UNIVERSITY OF CALIFORNIA, SAN DIEGO

Tunable Electro-Optic Devices for Fiber Optical RF Signal Processing

A dissertation submitted in partial satisfaction of the requirements for the degree

Doctor of Philosophy

in

Electrical Engineering (Photonics)

by

Jianxiao Chen

Committee in charge:

Paul K. L. Yu, Chair
William S. C. Chang, Co-Chair
Richard Herz
Lu Sham
Ivan Shubin
Charles Tu

2006

The dissertation of Jianxiao Chen is approved, and it is acceptable in quality and form for publication on microfilm:

_____

_____

_____

_____

_____
Co-Chair

_____
Chair

University of California, San Diego

2006

DEDICATION

This dissertation is dedicated to my wife and my parents.

TABLE OF CONTENTS

LIST OF FIGURES

LIST OF TABLES

ACKNOWLEDGEMENT

First of all, I am deeply indebted to my advisor, Dr. Paul Yu, and co-advisor, Dr. William Chang. They have provided constant support, guidance, and encouragement on my research and life for all these years in the Department of Electrical and Computer Engineering (ECE), University of California, San Diego (UCSD). Their wisdom and deep insights on Microwave Photonics keep on guiding me on the right track to finish this dissertation.

I am very grateful to Dr. Lu Sham, Dr. Charles Tu, Dr. Richard Herz, and Dr. Ivan Shubin for their valuable advices and kind support as the members of my doctoral committee.

I am very grateful to Dr. Tetsuya Kawanishi, Dr. Satoshi Shinada, and Dr. Masayuki Izutsu in National Institute of Information and Communications Technology, Japan, for the beneficial discussion and suggestion on the design of lithium niobate loop resonator device. I am also very grateful to Dr. Kaoru Higuma in New Technology Laboratories, Sumitomo Osaka Cement Co., Ltd., for his great effort on the fabrication of the lithium niobate loop resonator. I thank Dr. Justin Hodiak in SPAWAR, SSC San Diego, for her great support and beneficial discussion on the optical RF filter project.

My deep thankfulness goes to all my colleagues in ECE Dept., UCSD, Mr. Art Clawson, Dr. Guoliang Li, Dr. Dong-soo Shin, Dr. Yang Wu, Dr. Yuling Zhuang, Dr. Yimin Kang, Dr. Tsai-sheng Liao, Dr. Phil Mages, Dr. Felix Lu, Mr. Xiaobo Xie, Ms. Jessica Fisher, Mr. Fan Chang, Mr. Justin Bickford, Mr. Clint Novotny, Mr. Jeff Bloch,

Ms. Lauren Friedman, Mr. Sheldon Wu, Ms. Suju Kuo, and Ms. Meredith Hutchinson. We have spent lots of wonderful time together. For all these years, I have learned a lot from their outstanding performance on the scientific researches. My special thankfulness also goes to Prof. Wei-xi Chen and Prof. Li-sheng Yu who were visiting UCSD from Peking Univ., China. They trained me successfully with the modern lithography and device processing technique.

I thank my wife Qian Sui, my parents, and my brothers, for their endless support and understanding. They are my source of braveness. My life is complete because of them.

I also thank to the support from the staffs of ECE Dept. and International Center, UCSD, especially to Ms. Michelle Parks.

Finally, I would like to acknowledge the financial support from DARPA, AFRL, and NSF.

VITA

1992-1997	B. S., Electronics and Information System, Peking University, Beijing, P. R. China.
1997-2000	M. E., Communications and Information System, Peking University, Beijing, P. R. China.
2000-2006	Ph.D., Electrical Engineering (Photonics), University of California, San Diego.

PUBLICATIONS

1. **J. X. Chen**, T. Kawanishi, K. Higuma, S. Shinada, M. Izutsu, W. S. C. Chang, and P. K. L. Yu, "Tunability of Lithium niobate Loop Resonator", accepted by 2006 Asia-Pacific Microwave Photonics Conference (AP-MWP 2006), Kobe, Japan.

2. **J. X. Chen**, T. Kawanishi, K. Higuma, S. Shinada, J. Hodiak, W. S. C. Chang, M. Izutsu, and P. K. L. Yu, "Programmable Coupler Ladder based on Lithium niobate Y-junction Reflector", IEICE Trans. Electron., Vol. E88-C, No. 3, pp379-384, March. 2005.

3. P. K. L. Yu, I. Shubin, X. B. Xie, Y. Zhuang, **A. J. X. Chen**, W. S. C. Chang, "Transparent ROF link using EA modulators", International Topical Meeting on Microwave Photonis (MWP 2005), Seoul Korea, pp21-24, 2005.

4. **J. X. Chen**, Y. Wu, W. X. Chen, I. Shubin, A. Clawson, W. S. C. Chang, and P. K. L. Yu, "High-Power Intrastep Quantum Well Electroabsorption Modulator Using Single-Sided Large Optical Cavity", IEEE Photon. Technol. Letts., Vol. 16, pp440-442, Feb. 2004.

5. **J. X. Chen**, Y. Wu, W. X. Chen, I. Shubin, A. Clawson, W. S. C. Chang, and P. K. L. Yu, "High Power Junction Dynamics of the Intra-Step Quantum Well Electroabsorption Modulator", CLEO/IQEC 2004, San Fransisco, CThH5, May 2004.

6. **J. X. Chen**, T. Kawanishi, K. Higuma, S. Shinada, J. Hodiak, M. Izutsu, W. S. C. Chang, and P. K. L. Yu, "High Speed Tunable All-Pass Filter Based on Lithium niobate Waveguide Loop", 2004 IEEE International Topical Meeting on Microwave Photonics (MWP 2004) , pp221-224, Oct. 2004.

7. **J. X. Chen**, T. Kawanishi, K. Higuma, S. Shinada, J. Hodiak, M. Izutsu, W. S. C. Chang, and P. K. L. Yu, "Tunable Lithium niobate Waveguide Loop", IEEE Photon. Technol. Letts, Vol. 16, pp2090-2092, Sept. 2004.

8. **J. X. Chen**, Y. Wu, J. Hodiak, and P. K. L. Yu, "A Novel Digitally Tunable Microwave-Photonic Notch Filter Using Differential Group-Delay Module", IEEE Photon. Technol. Letts., Vol. 15, pp284-286, Feb. 2003.

9. **Alan J. X. Chen**, Yang Wu, Justin Hodiak, and Paul K. L. Yu, "Frequency Agile Digitally Tunable Microwave Photonic Filter", International Topical Meeting on Microwave Photonics (MWP 2003), pp89-92, Sept. 2003.

10. P. K. L. Yu, W. S. C. Chang, Y. Zhuang, **A. J. X. Chen**, Y. Wu, W. X. Chen, and I. Shubin, "Novel waveguide and materials structure for wideband electroabsorption modulator", International Topical Meeting on Microwave Photonics (MWP 2003), pp157-160, Sept. 2003.

11. **Alan J. X. Chen**, Yang Wu, Justin Hodiak, and Paul K. L. Yu, "Frequency Agile digitally tunable microwave photonic filter with high rejection level", GOMAC03 conference, Jul. 2003.

ABSTRACT OF THE DISSERTATION

Tunable Electro-Optic Devices for Fiber Optical RF Signal Processing

by

Jianxiao Chen

Doctor of Philosophy in Electrical Engineering (Photonics)

University of California, San Diego, 2006

Paul K. L. Yu, Chair

William S. C. Chang, Co-Chair

In order to provide the flexible coherent or incoherent RF signal processing in the optical domain, the tunable optical RF filters are very important elements to investigate.

For coherent optical RF signal processing, optical resonators are extensively used as filters or modulators. In the case of multiple resonators working together, accurate phase or frequency tunability is very essential to compensate the fabrication error, to align the carrier frequency to the passbands, and to fine-tune the RF response function shape. In this dissertation, we have proposed and demonstrated a loop resonator based on Titanium diffused lithium niobate waveguide which can be

accurately tuned over wide frequency range with fast tuning speed. A special waveguide structure called Y-junction reflector has been adopted to change the shape of the loop from a full circle to two slightly curved lines, so that the bending loss of the weakly-guided waveguide is avoided and the device is compact in size. The measurement has demonstrated a frequency tunability of 33.3 MHz/V for the testing device which has a 1.9 mm long phase tuning electrode. It is equivalent to 175 MHz/(V·cm) by normalizing the tunability to the electrode length. With reasonable assumptions, we predicted that the device can have a frequency tunability of 260 MHz/(V·cm) with an improved overlap between the optical and electrical fields. The design issues of the optical structure and electrode have been theoretically and experimentally investigated. The device also has a unique advantage of high speed tunability. It has been evaluated as a modulator. As a modulator a 3 dB link gain bandwidth of 5 GHz has been measured and a -42 dB normalized link gain is estimated.

For incoherent optical RF signal processing, we have introduced and demonstrated a novel notch filter based on a tunable differential group delay (DGD) module with 6-bit resolution. The notch filter can provide 60 dB rejection level and the notch frequency is digitally tuned according to the DGD delay time setting. The bandpass filter based on two DGD modules also has been investigated experimentally.

Chapter 1. Introduction

In this chapter, we first briefly review the recent development of Microwave Photonics and the coherent and incoherent radio frequency (RF) signal processing in the optical domain. Then the optical resonators for optical RF signal processing are discussed, as illustrated by an application example. In order to create an optical resonator with accurate and high speed tunability we propose a tunable lithium niobate (LN) loop resonator based on Titanium (Ti) diffused waveguide. In order to improve the coherent noise to the transversal filter we introduce a new tunable notch filter method based on differential group delay (DGD) modules. The outline of the thesis is given at the end of the chapter.

1.1 Microwave Photonics and Optical RF Signal Processing

With the soaring demands of the voice and digital data transmission generated mainly by the cellular phone and Internet services, last few decades are the heydays for the development of new communication techniques, especially for the optical fiber communications and radio frequency (RF) wireless communications. The optical communications solve the high capacity, long haul communication problems due to the inherent advantages of the high frequency optical carrier and the low propagation loss optical fiber. The wireless communications meet the requirements of the low cost, short distance communications due to the flexibility of the wireless access and its limitation in the bandwidth.

It is the growing trend that the wire and wireless communications are most likely complementary to each other. “Optical fiber doesn’t go everywhere, but where it does go, it provides a huge amount of available bandwidth (well over tens of terabits per second over a single fiber). Wireless, on the other hand, does go almost everywhere, but provides a highly bandwidth-constrained transmission channel, susceptible to a variety of impairments.” [1]

To utilize the advantages of both the wireless and optical communications, many types of the optical RF links or networks have been developed to transmit the RF signal over optical fibers. For example, many current researches have been found on the optical fiber feeder for the microcellular mobile communications system, or briefly *RF-over-Fiber*. [2-8] A block diagram of the RF-over-fiber system is depicted in Fig. 1-1. [2] Since the micro base stations (BS) are connected to the central BS through fiber, one major advantage of the RF-over-fiber system is to reduce the burden on the micro BS and move the expensive signal processing functions to the central BS which is fewer in number compared to the large number of the micro-BS, so that the total system cost will drop extensively. Other applications include the cable TV transmission, [9-10] communication of signals from a remote sensor or antenna [11], and some types of radar signal transmission [12-13]. All these techniques related to the RF or microwave signal transmission, modulation, signal processing in the optical domain are generally called Microwave Photonics (MWP). Over more than two decades, MWP has been marching very quickly to be an important interdisciplinary research area.

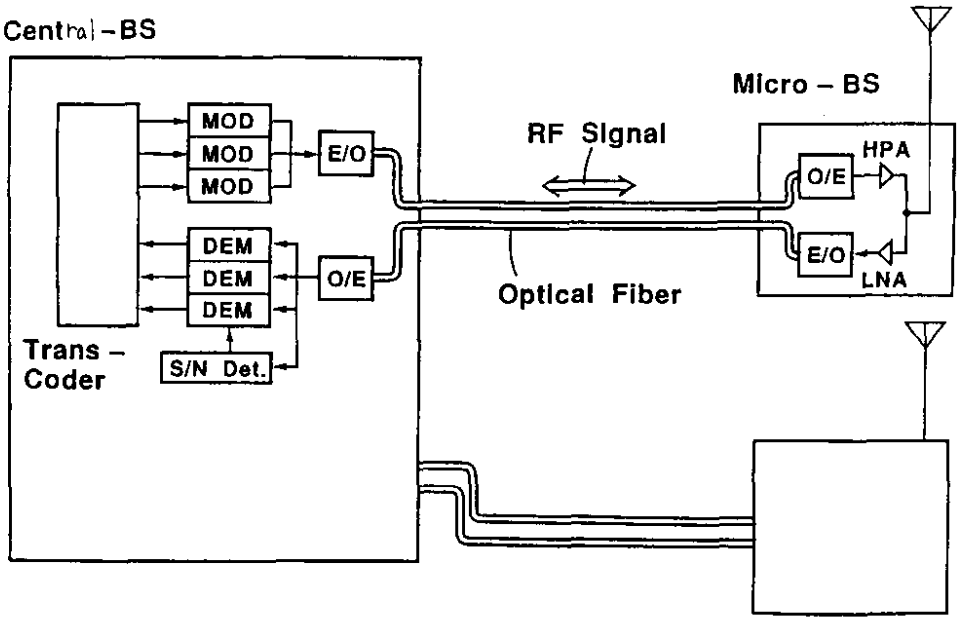

Fig. 1-1. Block diagram for the optical feeder system. MOD: modulation; DEM: demodulation; HPA: high power amplifier; LNA: low noise amplifier. After [2].

Since the RF signal is already carried in the optical domain, one question is raised naturally: can we do any signal processing in the optical domain to affect the output of the RF signal? The answer is yes.

A basic scheme of optical RF signal processing system is depicted in Fig. 1-2, where the modulator converts the RF signal from electrical domain into the optical domain, and then some signal processing devices are inserted to change the signal characteristics, finally the optoelectronic detector is used to recover the RF signal in the electrical form. As a comparison, the traditional RF signal processing in the electrical domain is also depicted. [14]

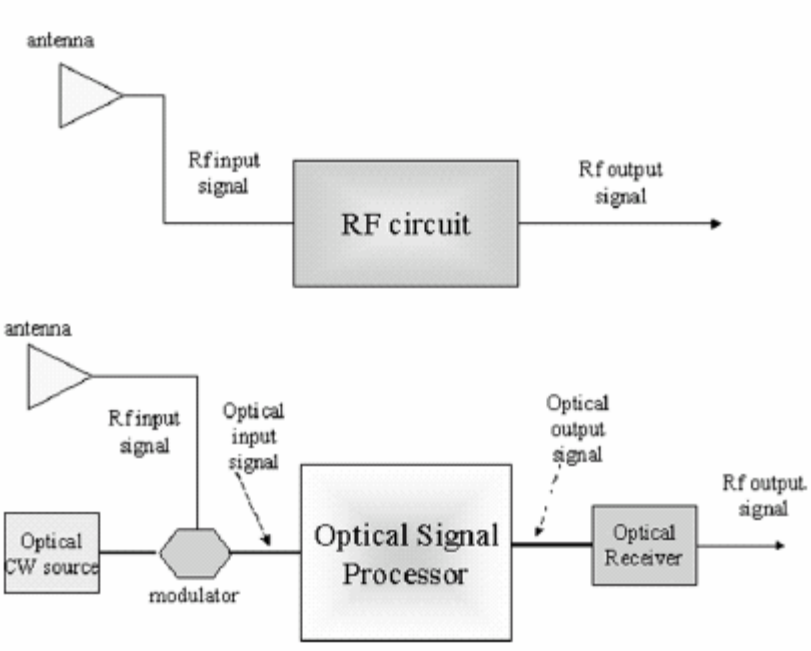

Fig. 1-2. Traditional RF signal processing in electrical domain (upper) and optical RF signal processing system diagram (lower). After [14].

It is generally accepted that the first milestone paper for optical RF signal processing was published in 1976 by Wilner and Van Den Heuvel, trying to utilize the fiber-optic delay lines for microwave signal processing. [15-16] The authors noted that some most important advantages of the fiber such as low loss and high modulation bandwidth make it suitable for broadband signal processing in addition to allow direct processing of high frequency signals that are already in the optical domain. After that, pioneering works based on optical fiber delay lines have been done at Stanford during 1980s. [17-20]

Nowadays, benefited from its unique functional advantages such as the inherent speed, parallel signal processing capability, low-loss (independent of RF frequency) delay lines, very high sampling frequency ability (over 100 GHz in comparison to around a GHz with electronic technology), [21] and EMI immunity, optical RF signal processing has become an important research area, including extensive research in many applications, e.g., signal filtering, [14] [22] multi-Gbit/s A/D converters, [23-25] frequency converters and mixers, [26-27] signal correlators,[28] arbitrary waveform generators, [29] optical RF channelizer, [30] optical RF spectrum analyzer, [31-32] microphotonic RF receiver, [33] single sideband signal forming, [34] millimeter-wave generation, [35] chaotic encryption, [36-37] and beam formers for phased arrays. [38-39]

Other research topics important to optical RF signal processing are improvements in fundamental link devices such as the laser source, modulator, and detector. Different applications will have different requirements for the devices. Ideal devices should provide the link with good performances such as high link gain, low noise figure, high linearity, large bandwidth, and high frequency operation. [40] Although performances of the laser [41], modulator [42], and detector [43] have already been improved significantly over last few decades, researches are still being carried on to obtain better link figure of merits such as transparent link gain or ultra-high spurious free dynamic range (SFDR).

Among all these interesting topics, our research in this thesis is focused mainly on the coherent and incoherent optical RF filters. A small portion of the discussion will be covered with modulation issues.

Filters, including the low-pass filter (LPF), high-pass filter (HPF), band-pass filter (BPF), and notch filter, are essential devices for RF signal processing. They are used to reduce the noise, to reshape the signal, or to select the signal channel. Various types of traditional electric filters have been developed over quite a long time, ever since the first filter design, so called "Wagner filter", was introduced by the German scientist K. W. Wagner in 1915. [44] For frequency below 1 GHz, the most commonly used filters are the bulk-wave, surface-acoustic wave (SAW) and helical resonators. From 1 GHz to 10 GHz, filters such as the coaxial, dielectric, waveguide, and stripline resonators are used. Coaxial resonators have many attractive features including an electromagnetic shielding structure, low-loss characteristics and small size, but their minute physical dimensions for applications above 10 GHz make it difficult to manufacture. Dielectric resonators also possess a number of advantages such as low-loss, acceptable temperature stability and small size. However, high cost and present-day processing technology restrictions limit dielectric resonator utilization to applications below 50 GHz. Waveguide filter can work beyond 50 GHz; but its greatest drawback is its large size, which is significantly larger than other filters available in the microwave region. The most common choice for RF and microwave circuits remains the stripline resonator, that has the practical features such as small size, ease of fabrication by conventional photolithography, and good affinity with

active circuit elements. However a major drawback for the resonator is a drastic increase in insertion loss compared to other type of filters, making it difficult to apply such stripline resonators to narrow band filters. [44]

Comparing with traditional electric filter, optical RF filter has its unique advantages. For example, optical delay lines have very low loss (independent of the RF signal frequency), very large time bandwidth products, immunity to EMI, and lightweight. They can provide very short delays which result in very high speed sampling frequencies. For very high speed RF telecommunications systems, where filters are difficult to implement due to the use of high frequency carrier, it is very important to develop a low cost technology for the implementation of very-high frequency filters in optical domain.

1.2 Optical Resonators for Optical RF Filter

1.2.1 Coherent and Incoherent Optical RF Filter

By examining the relationship between the coherent time τ of the optical transmitter and the basic delay T (time between adjacent temporal samples provided by the delay line or resonator), the processing system is divided into two main categories. When $\tau >> T$, the processor works under the coherent regime and its transfer function is generally governed by the electric field of the optical wave. When $\tau << T$, the processor works under the incoherent regime and the transfer function is affected by the optical power rather than the electric field. [16] In other words, the incoherent filter is generally related to the finite impulse response (FIR) and is realized with an

optical delay line, while the coherent filter is related to the infinite impulse response (IIR) and the response of the optical resonator.

Both the coherent and incoherent filters have their pros and cons. [16] [23] In the coherent scheme, the processor is more sensitive to the optical phase fluctuation, and consequently it is sensitive to the environmental disturbance to the optical carrier phase and polarization. It requires more care to maintain the system stability that makes its implementation more challenging under practical conditions. Thus, the coherent processor will function better when it is implemented using integrated optics. On the other hand, the coherent processor also has its unique advantages. For example, it is easy to realize negative weight with optical phase, leading to a better flexibility in the transfer function design. For the incoherent processor, it is governed only by the intensity. It is generally more robust to the environmental temperature or vibration. But it is very hard to realize any negative weight since the optical intensity is always positive. Only with a complex setup such as differential detector [45] or inversion in a semiconductor optical amplifier [46], optical negative weights can be realized in incoherent regime. [23]

Majority of the research efforts in the past focused on incoherent filters as they are relatively easier to achieve. A common limitation for these incoherent filters is caused by the optical coherence of the light source. When the light source is with a long coherent length, the residual amplitude interference increases the coherence noise. [47-49]. A detailed review to the incoherent filter and the proposal of using differential group delay module to improve a coherent noise is found in the beginning of Chapter

4.

On the other hand, few researches have been conducted on the coherent filter. The key limitation is that, in order to do coherent filtering, a low loss optical resonator with very good tunability is generally required. [50] In the next section, we will first introduce examples of the coherent optical RF filter based on optical resonators. Then we will point out the importance of the tunability for coherent optical RF filters, especially for filters based on the multiple loop scheme.

1.2.2 Optical Resonators and Optical RF Filters

It is well known that any signal processing scheme needs a structure to provide a reference signal which is used to interference with the incoming signal. This feature makes the resonator, which is inherently a dynamic memory device, very attractive for filtering, modulation, or other signal processing. There are several basic types of resonators, such as the Ferry-Perot cavity, the waveguide loop or ring resonator, the microdisk, and the microsphere. Let's examine the loop resonator as an example and briefly introduce several types of optical filter based on the loop resonator, including the all-pass filter (APF), the single loop band pass filter (BPF), and the multiple loop band pass filter.

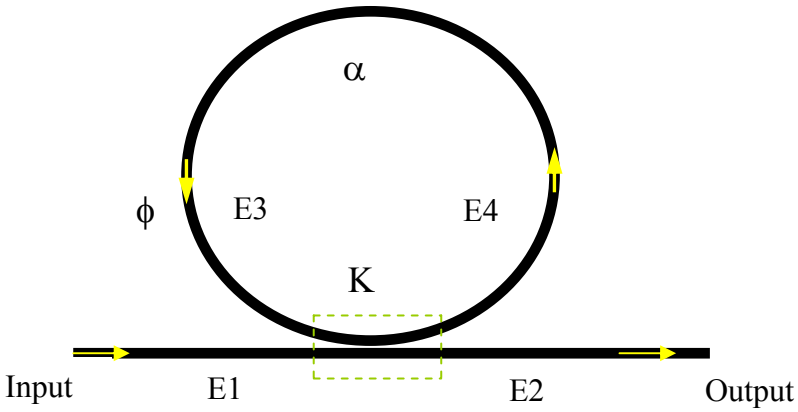

Fig. 1-3. All-pass filter consists of loop resonator coupled with a bus waveguide.

The structure of the APF in Fig.1-3 consists of a loop and a straightforward bus waveguide which is coupled with the loop at the coupler section. The injection light from the input port of the bus waveguide is partially coupled to the loop. When the roundtrip propagation phase of the light in the loop meets the resonant condition, the in-phase interference happens between the lights in the bus waveguide and the loop waveguide. A strong intensity of the light will be eventually built up inside the loop. If the loop is lossy, the injection light has to compensate the loss inside the loop. Consequently, the output light at the output port of the bus waveguide will be reduced. The APF is generally used as a notch filter to filter out the undesired wavelength.

The APF is the simplest filter structure. It is the building block for more complicated filters. Once we understand the characteristics of APF, it becomes relatively easy to extend the analysis to other filters. In this thesis, we focus on the design and demonstration of APF.

The most important parameters of the APF are the power coupling ratio K, roundtrip loss factor α (many times it is represented by $-10\mathrm{Log}_{10}(\alpha^2)$ in dB scale), and roundtrip phase ϕ which is given by

$$\phi = \frac{2\pi}{\lambda} nL \tag{1.1}$$

where L is the loop length, n is the effective optical refractive index, and λ is the wavelength. Obviously, the phase is a periodic function of the input optical wavelength. The frequency period, known as the free spectrum range (FSR), is given by

$$FSR = \frac{c}{nL} \tag{1.2}$$

The steady state transmission response of APF in Fig.1-3 has been described by a model using a coupler connected to a feedback delay line. [51-52] In [51], the coupler is assumed to be lossless. The loss caused by the coupler is implicitly included in the roundtrip propagation loss. While in [52], the coupler loss is explicitly included. For simplicity, we followed [51] in this thesis. We assume the two branches of the coupler are symmetric. In the bus waveguide, let E_1 be the optical amplitude injected to the coupler area. E_2 is the output. The optical amplitudes in the loop are E_3 and E_4 for the in-bound and out-bound respectively. Then the relationships among E_1, E_2, E_3 and E_4 are given by

$$\begin{bmatrix} E_2 \\ E_4 \end{bmatrix} = \begin{bmatrix} \rho & -j\kappa \\ -j\kappa^* & \rho^* \end{bmatrix} \begin{bmatrix} E_1 \\ E_3 \end{bmatrix} \tag{1.3}$$

$$E_3 = \alpha E_4 e^{-j\phi} \tag{1.4}$$

where κ is the coupling ratio of the electric fields and ρ is the transmission ratio. For lossless couplers, we have the relationship $|\rho|^2 + |\kappa|^2 = 1$ which represents energy conservation. So, $\kappa = \sqrt{\mathrm{K}}$, $\rho = \sqrt{1-\mathrm{K}}$, $k = k^*$, and $\rho = \rho^*$. More detailed analysis about the coupler can be found in Chapter 2.

Solving the equations, we obtain the amplitude transmission function as

$$\frac{E_2}{E_1} = \frac{\rho - \alpha e^{-j\phi}}{1 - \rho\alpha e^{-j\phi}}. \tag{1.5}$$

Many times we are interested in the fiber-to-fiber power transmission function which is given by

$$T = \Gamma\left|\frac{E_2}{E_1}\right|^2 \tag{1.6}$$

where Γ describes the extra loss introduced by the fiber to waveguide coupling and the propagation loss of the bus waveguide.

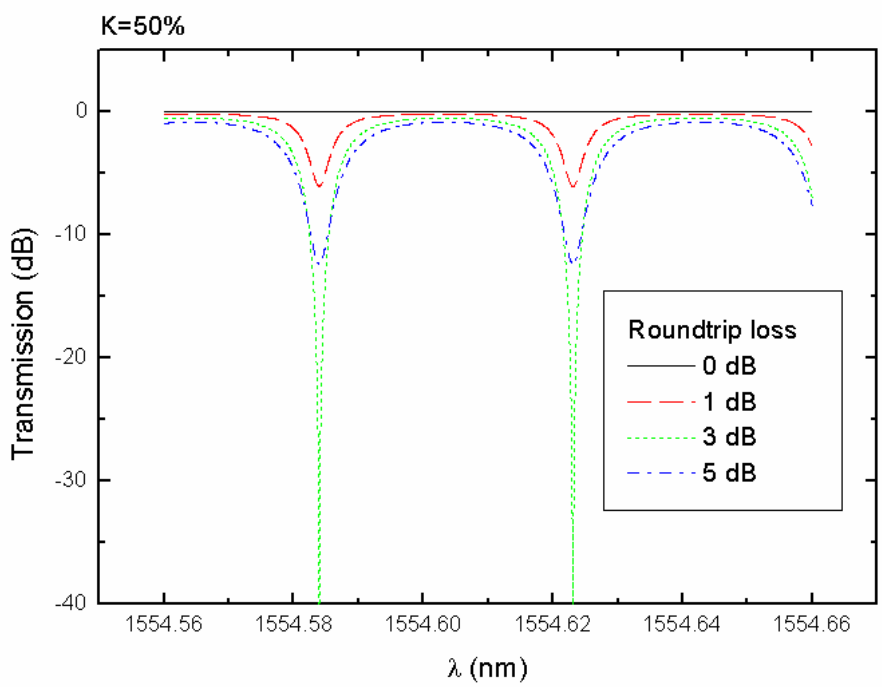

Fig. 1-4. The normalized transmission of the all-pass filter.

Assuming Γ =1, Fig. 1-4 shows the normalized power transmission function of the APF under different roundtrip power loss. The roundtrip optical path is arbitrarily set as 61740.3 μm. The power coupling ratio is 50%.

For α=1, the loop is lossless. We have $\left|\frac{E_2}{E_1}\right|^2 = \left|\frac{\rho - e^{-j\phi}}{1-\rho e^{-j\phi}}\right|^2 \equiv 1$. It means all the input power will be fanned out no matter whether it meets the resonant condition or not. The output response spectrum is a horizontal line. This means the output power is independent of the input wavelength. This also is the reason to name it the “All-pass”

filter. Although the output power is uniform across the spectrum, the phase is still different for different wavelengths.

If the loop has internal roundtrip loss, the output exhibits notches in the optical spectrum whenever the resonant roundtrip phase satisfies

$$\phi = 2m\pi, (m = 0,1,2,3...) \tag{1.7}$$

The out-of-band rejection level of a filter is defined by the ratio between the maximum and minimum output power. The minimum output power is determined by the coupling ratio and the roundtrip loss through

$$\left|\frac{E_2}{E_1}\right|^2 = \left|\frac{\rho - \alpha}{1 - \rho\alpha}\right|^2 \tag{1.8}$$

Obviously, when $\rho=\alpha$, the output is 0. This is the important condition to achieve a notch filter with high rejection level. In the example shown in Fig. 1-4, the maximum rejection level is realized at a roundtrip loss of 3 dB. For loss smaller or larger than 3 dB, the maximum output power would be larger or smaller. But the rejection levels are always smaller.

The analysis above is based on the steady state response. It is also important to understand the loop transient behavior in the time domain. The transient analysis can be done with R-soft Fullwave program. As an example, an intuitive view of a lossless APF under resonant condition is shown in Fig.1-5 (a), (b), (c), and (d). To each figure, the top is the electric field distribution and the bottom is the output power monitored at the output port of the bus waveguide. For the power monitor plot, the vertical axis is the power level and the horizontal axis is the time scale.

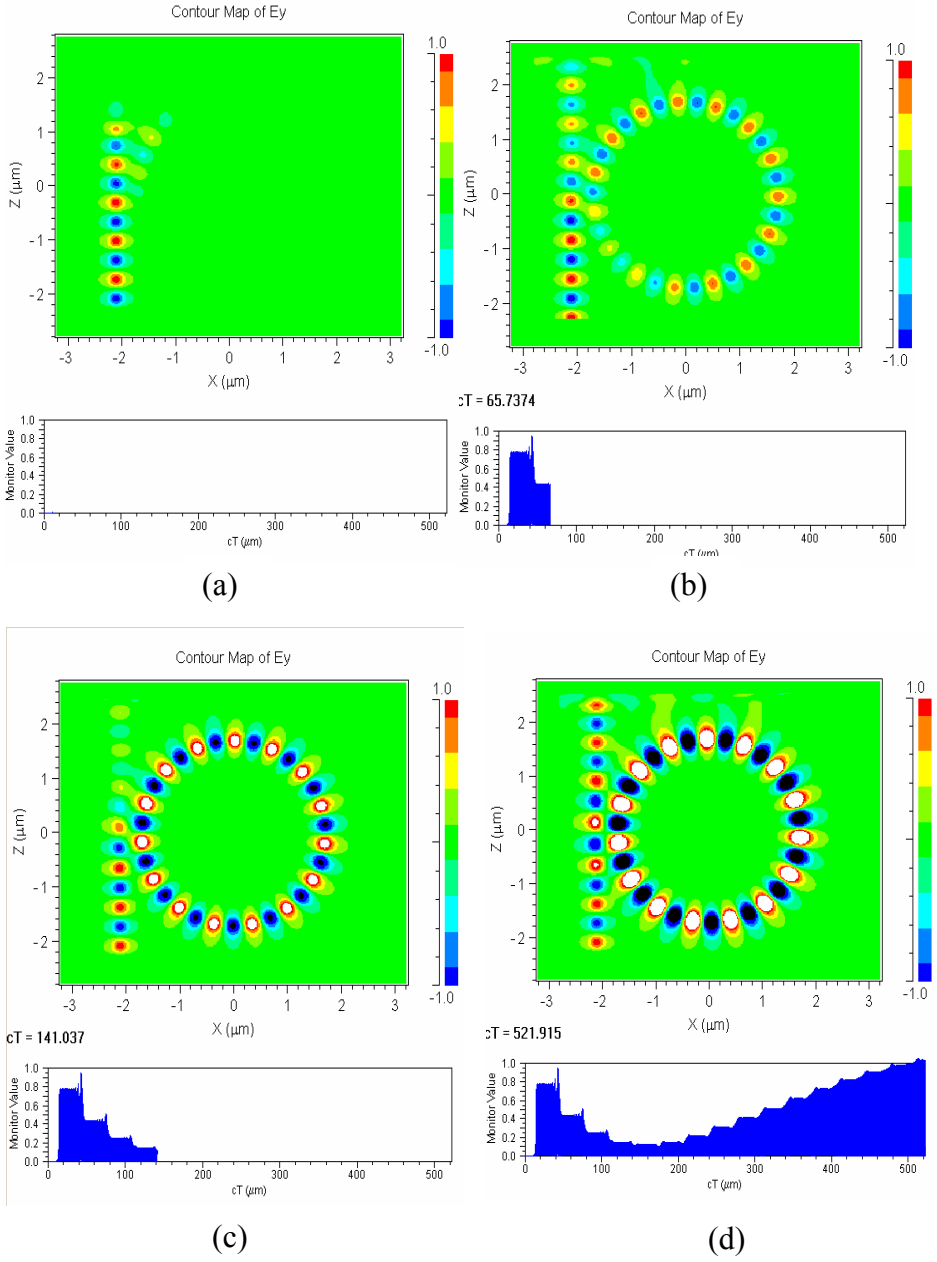

Fig. 1-5. The transient response of the lossless APF in time domain. (a) the light in the bus waveguide starts to couple to the loop; (b) the in-phase interference happens between the lights in the bus waveguide and loop waveguide; (c) more and more light is coupled and stored inside the loop; (d) The steady state is built up.

The evolution of the transient output power from (a) to (d) in the time domain is to show how the steady state is built. In Fig. 1-5 (a) the input light has not reach the output port yet, so that the output power is zero. In Fig. 1-5 (b) and (c), the decrease of the output power indicates the light is coupled into the loop due to the in-phase resonance. When the light inside the loop is strong enough, it starts to couple back to the bus waveguide. The monitored output power goes back. Eventually, the output power goes back to one when the loop reaches the steady state, as shown in Fig. 1-5 (d).

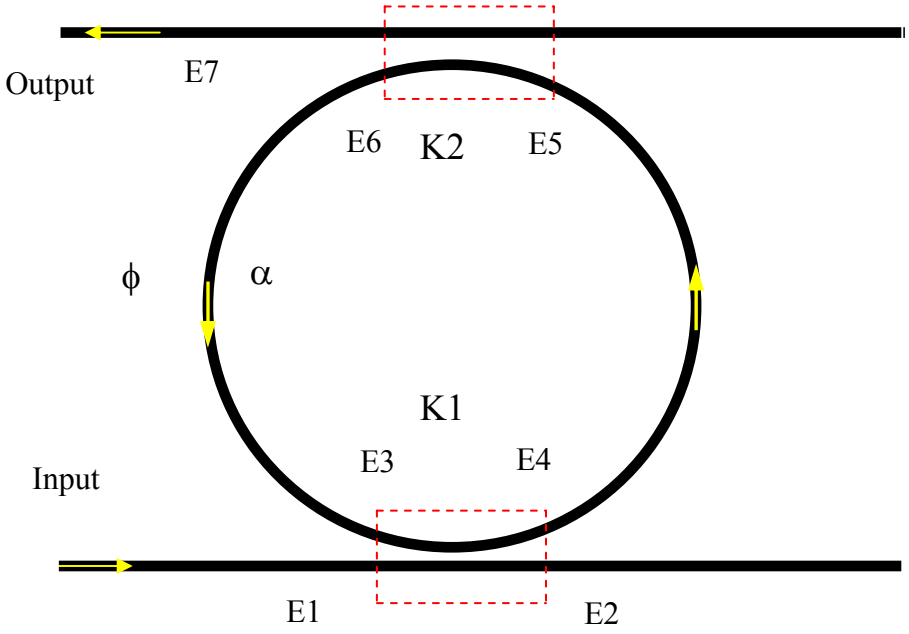

Fig. 1-6. The bandpass filter consists of one loop and two bus waveguides.

For the single loop BPF bandpass filter shown in Fig.1-6, we can derive the transmission function in a similar manner. Now we have two couplers to take care of. The relationships of the electric field is described by two matrices

$$\begin{bmatrix} E_2 \\ E_4 \end{bmatrix} = \begin{bmatrix} \rho_1 & -j\kappa_1 \\ -j\kappa_1^* & \rho_1 \end{bmatrix} \begin{bmatrix} E_1 \\ E_3 \end{bmatrix} \tag{1.9}$$

$$\begin{bmatrix} E_6 \\ E_7 \end{bmatrix} = \begin{bmatrix} \rho_2 & -j\kappa_2 \\ -j\kappa_2^* & \rho_2 \end{bmatrix} \begin{bmatrix} E_5 \\ 0 \end{bmatrix} \tag{1.10}$$

$$E_5 = \sqrt{\alpha} E_4 e^{-j\phi/2} \tag{1.11}$$

$$E_3 = \sqrt{\alpha} E_6 e^{-j\phi/2} \tag{1.12}$$

The ratio between the output and the input field is given by

$$\frac{E_7}{E_1} = \frac{\kappa_1 \kappa_2 \sqrt{\alpha} e^{-j\phi/2}}{1 - \rho_1 \rho_2 \alpha e^{-j\phi}} \tag{1.13}$$

We can see that the maximum output, $\left|\frac{E_7}{E_1}\right|^2_{\max} = \left|\frac{\kappa_1 \kappa_2 \sqrt{\alpha}}{1 - \rho_1 \rho_2 \alpha}\right|^2$, happens when the roundtrip phase is $\phi = 2m\pi, (m = 0,1,2,3...)$. Since the phase is wavelength dependent, a periodic passband structure is expected in the optical frequency domain. That's why this structure is called "Bandpass" filter. The bandpass filter with loop roundtrip optical path of 61740.3 μm and symmetric power coupling ratios of 25% is simulated under different loop roundtrip loss conditions, as shown in Fig. 1-7. It can be seen that the larger the loop loss, the smaller the output power and the wider the passband width.

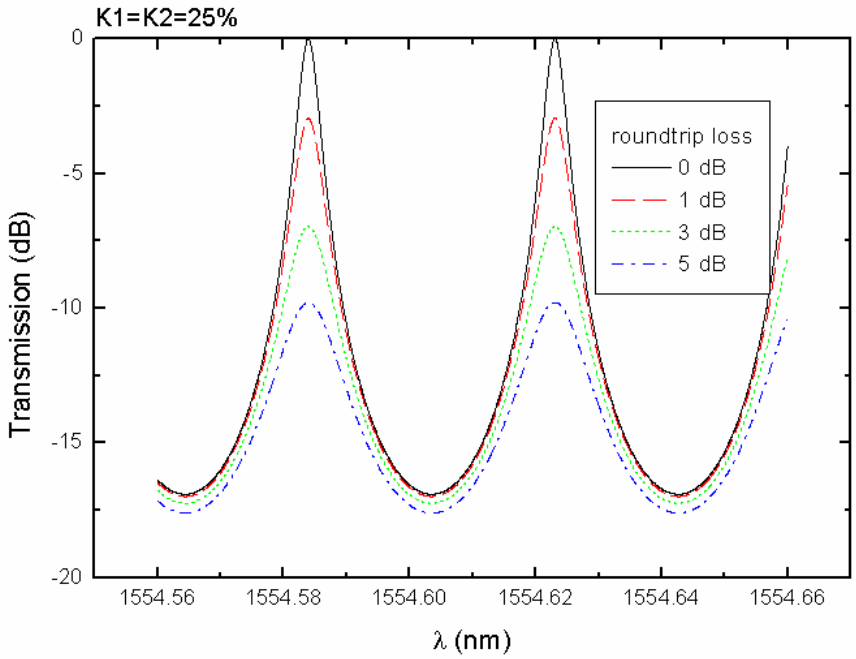

Fig. 1-7. The transmission of the single loop bandpass filter.

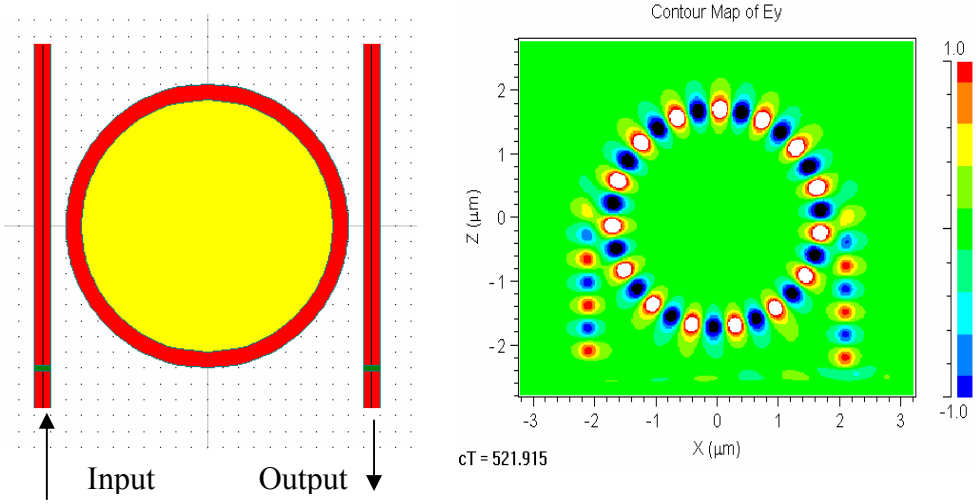

Fig. 1-8. Intuitive view of band pass filter (left) and its electric field distribution at resonance (right).

Similar to the APF, the transient response of the BPF can be analyzed by R-soft Fullwave simulation. An intuitive view of the lossless BPF under resonant condition is given in Fig.1-8. For simplicity, only the electric field for the final steady state is shown.

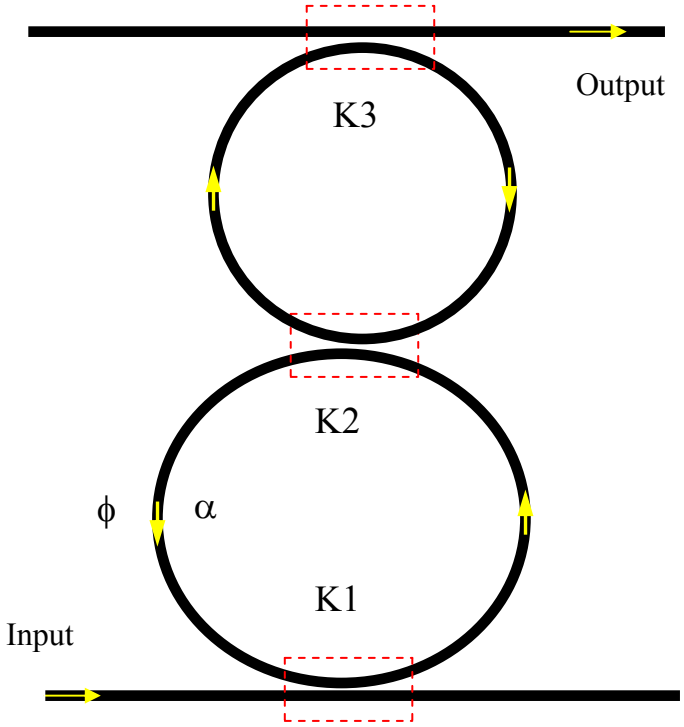

Fig. 1-9. Diagram of double loop bandpass filter.

For the multiple loop band pass filter (BPF), for instance, the double loop shown in Fig.1-9, the transmission function is more complex since each loop has its own resonant condition. A thorough discussion about the transmission is found in [53-54]. The multiple loop BPF has two advantages. The first is that it can extend the FSR. The

total FSR is the integer number times of the each loop. Take the double loop as example, we have

$$FSR = nFSR_1 = mFSR_2 \quad (1.14)$$

where n and m are integer number. Frequency which can not resonate with either loop simultaneously will be blocked from the output. For example, assuming FSR_1=12.5 GHz for loop 1, and FSR_2=14.39 GHz, the total FSR is extended to about 100 GHz, shown in Fig.1-10. [54]

This FSR alignment raises a serious requirement to the loop roundtrip phase tunability. In [54], the authors use thermal heaters to fine-tune the phase of SiO_2-GeO_2 waveguides to accomplish this.

The second advantage of the multiple loop is its ability to suppress the out-of-band output which helps to improve the out-of-band rejection level or the skirt-selection of the BPF, defined as the ratio of the 3 dB bandwidth and 30 dB bandwidth. A 50 dB out-of-band rejection has been reported. [55] Again, to do so, an accurate tunability is required to align all the passbands together.

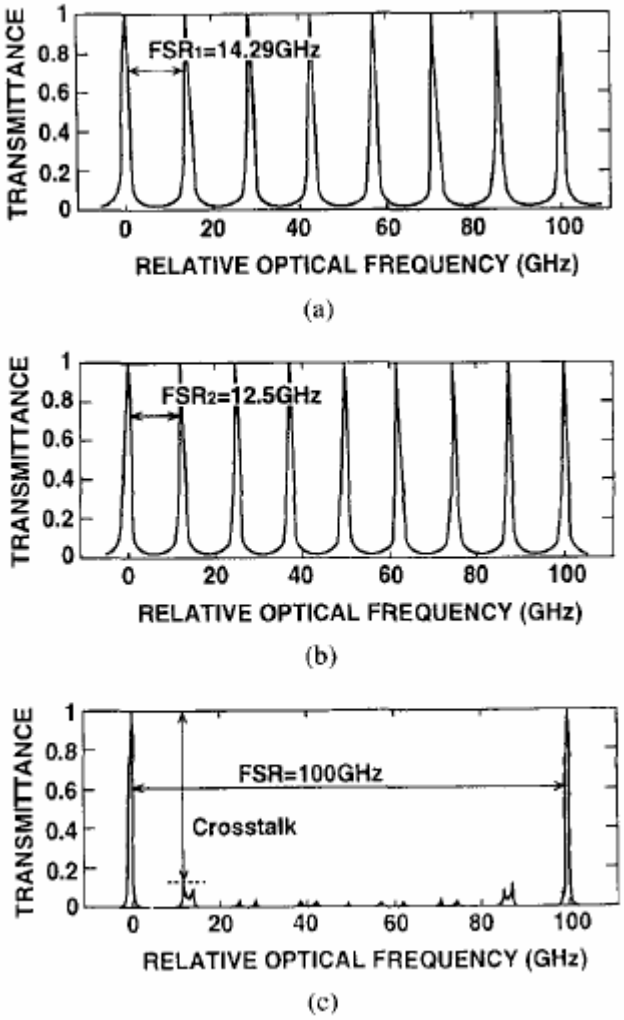

Fig. 1-10. The expansion of the FSR of the double loop band pass filter. (a) FSR1=14.39 GHz for loop 1; (b) FSR2=12.5 GHz for loop 2; (c) FSR=100 GHz for double loop. After [54].

1.2.3 Tunability of Optical RF Filter

We have introduced several types of optical filters based on loop resonators. One important issue to be discussed is that how the optical filters can perform the RF filtering function. In this section, we will give a detailed application example, from which it can be seen that tunability plays a key role in realizing a good optical RF filter.

An example of the coherent optical RF filter based on the triple loop resonator is shown in Fig. 1-11. [50] Each loop has a perimeter of 2.7 cm, corresponding to a free spectrum range (FSR) of 7.5 GHz. The resonator will periodically generate passbands in the optical spectrum, i.e., the output is high at the resonated wavelengths. The output is low at the out of phase wavelengths.

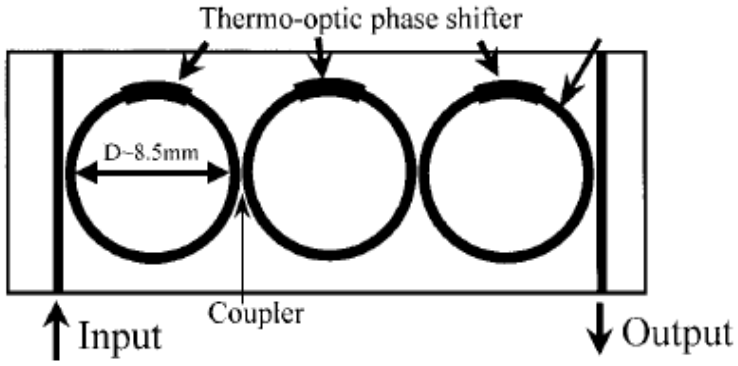

Fig. 1-11. Triple loop band pass filter with thermo-optic phase shifter. After [50].

Now suppose the input optical signal is amplitude modulated by an RF signal. It will consist of a carrier tone and two side band tones, as shown in the insets in Fig.1-12. Once all the three tones are aligned at the optical filter's passbands in the optical spectrum as shown in the central inset figure, the output of the detector in the receiving end can recover the RF signal with the maximum power. If the carrier is aligned to a passband while the sidebands are located at the stopbands as shown in the left and right insets, the detector output of the RF signal is small. In this way, the BPF response function in the RF domain is formed. The total BPF response, i.e., the RF transmission, is depicted by the solid curve in Fig. 1-12. [50]

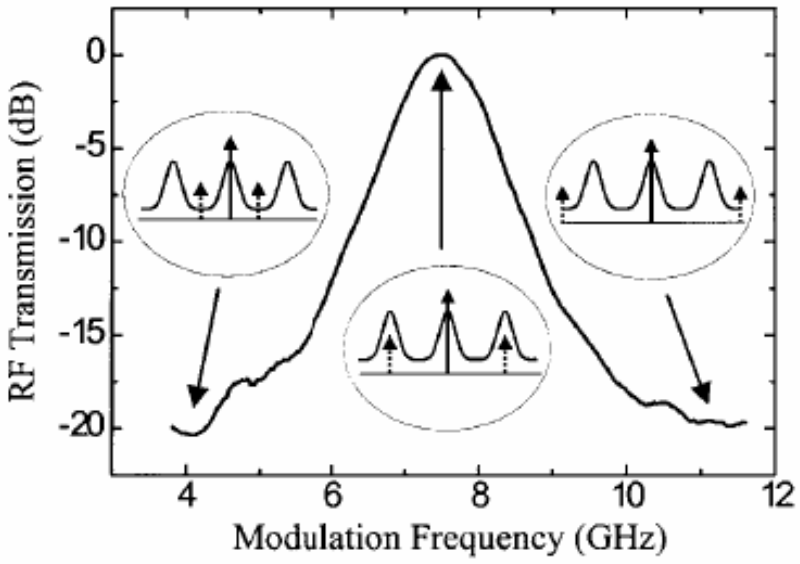

Fig. 1-12. Working principle of the RF BPF based on the triple loop resonator. The inserts show the optical tones aligning to the pass bands of the optical filters. After [50].

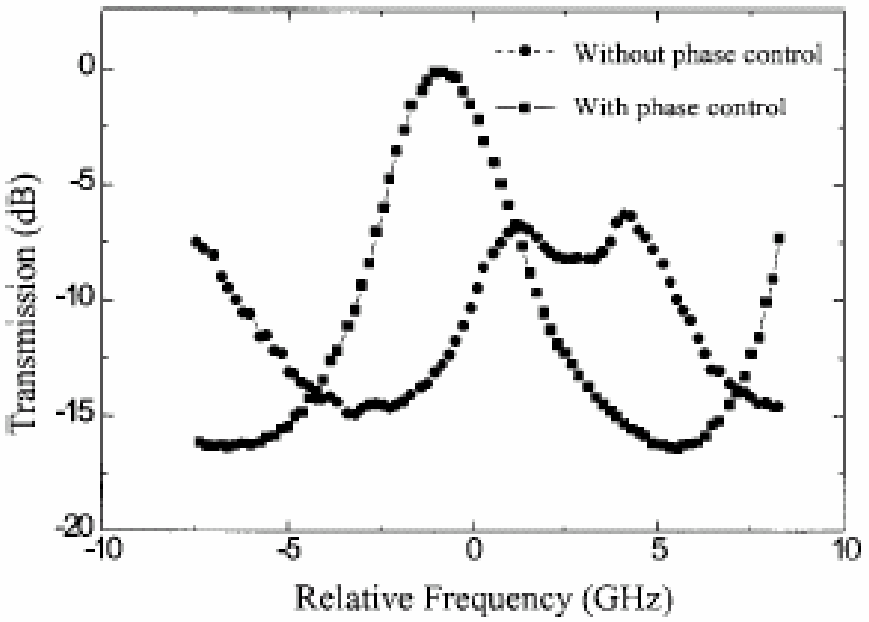

Fig. 1-13. The optical response functions with/without accurate control to the loop roundtrip phases. After [50].

To obtain a good performance, the roundtrip phases of all the rings have to be carefully controlled. For example, the input optical wavelength has to resonate with all three rings, so that it is coupled effectively to the output. Otherwise, the response function will change in shape. Fig.1-13 compares the optical response of the filter with and without the phase control. It is seen that without accurately controlled loop phase, the response function has worse bandwidth and larger insertion loss. [50]

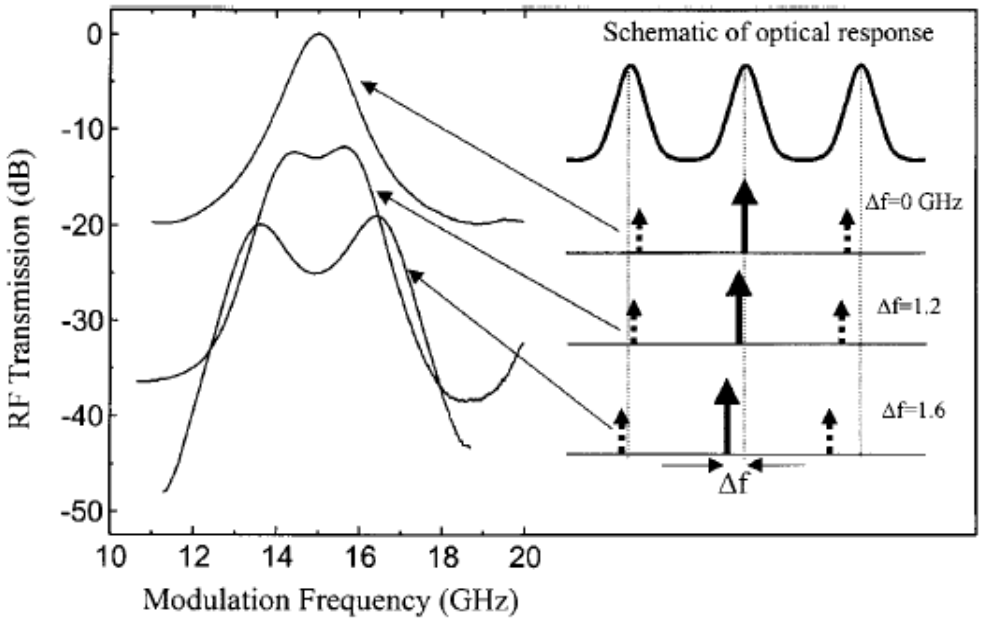

Fig. 1-14. The RF response functions for the different offsets of the optical carrier to the pass band. After [50].

Another important application of the accurate phase control is to align the passband to the carrier wavelength. In Fig. 1-14, we can see that if the optical carrier is offset from the center of the passband, the RF transfer functions will change in shape. This causes fluctuation of the output RF signal and should be avoided. [50]

In practice the fabrication process always introduces errors in the loop phase due to the limited resolution of the lithography and variation of the mask pattern. A way to compensate these variations is to apply thermo-optic phase shifters to the rings. Once the loop is heated up, the offset of the loop phase will be compensated. However, thermal tuning is not a desirable solution. First, it is inherently slow in tuning speed because heat conduction is slow. Second, the thermal electrode generally consumes

large power. Typically, 150 to 400 mW powers are used in this scheme. Third, ambient temperature variation will affect the control. [50]

It is very important for us to find a more efficient and convenient way to achieve accurate phase tuning for the resonator.

1.3 Proposed Tunable Lithium Niobate Loop Resonator

Our investigation in this thesis was motivated by the need to obtain an optical RF bandpass or notch filter in the optical RF link for radar systems on a ship, to get rid of out-of-band noise. The link diagram is shown in Fig.1-15. The radar will function at the RF frequency of 20 to 60 GHz [56]. The optical RF filter is a competitive solution to the electrical filters in this case. As the antennas may work in the array format, the system requires a filter to have very flexible tunability of the center freqeuncy. For example, the filter should accurately tune over frequencies in a wide range >10 GHz. Meanwhile the pass band of the filter could be as narrow as 100 MHz, implying that the filter should have very low loss. The out-of-band rejection level should be as large as 40 dB, which generally requires a multiple loop structure. In order to align the pass bands of different loops, an accurate tunability in order of several MHz is required. Finally, the device should be compatible with fiber system. All these requirements led us to search for a low loss and highly tunable optical resonator.

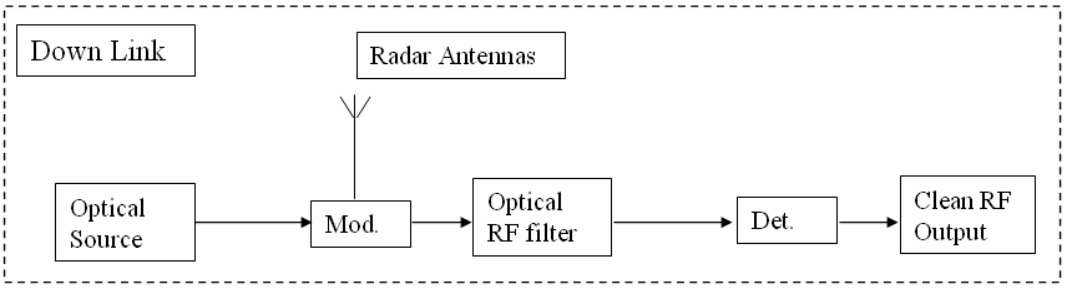

Fig. 1-15. Optical RF filter in the optical RF downlink of the antenna system.

Passive or active loops have been demonstrated in material structures such as glass waveguide, PMMA waveguide, GeO_2-doped silica waveguide, [57] and optical fibers. [58] However, the resonance frequency in these ring structures generally can not be tuned conveniently. Although the resonant frequency of some of them is tuned thermally, the tuning speed and accuracy are not sufficient for the application. An interesting candidate with good tunability is the lithium niobate microdisk. [59] Unfortunately, it has to couple the light in and out with a prism which is not compatible with fiber system and may not work stably.

We propose a new solution to realize a low loss, accurately tunable resonator. This is based on a loop resonator formed by the Titanium diffused lithium niobate (Ti:LN) waveguide. The advantages of the device include 1) large EO effect enabling high speed and accurate tunability; 2) low loss; 3) matured fabrication technology in comparison with lithium niobate microdisk; 4) easy to extend the technique to complex structure such as multiple loop filter.

There was one important issue that prevented previous efforts from realizing a low loss loop based on Ti:LN waveguide. Ti:LN waveguide is a weakly guided

waveguide because the index difference between the waveguide core and the surrounding material is very small. It is not possible to form a full low loss circular loop due to severe bending loss. The bending loss is governed by the bending radius and the waveguide structure. The bending loss for semi-circle bending of a TM mode has been estimated experimentally and theoretically at 1.3 μm wavelength. [60] The bending loss increases sharply when the bending radius is less than 8 mm. For the wavelength at 1.55 μm, a simple estimation has been done for the TM mode by FIMMWave simulation. The waveguide is exponentially bended as shown in Fig.1-16. The detailed structure of the waveguide can be found in chapter 2. Assuming the waveguide has a horizontal offset, Lx, of 100 μm and a vertical offset, Ly, that varies from 0 to 15 μm, the bending loss, represented by the output optical power normalized to the input power, is given as a function of Ly in Fig. 1-17. The calculated result shows the output decreases quickly with increased vertical offset. For our device, the bending loss is as large as 10 dB for a circular loop with the radius of 4 mm, which is not acceptable for a low loss loop.

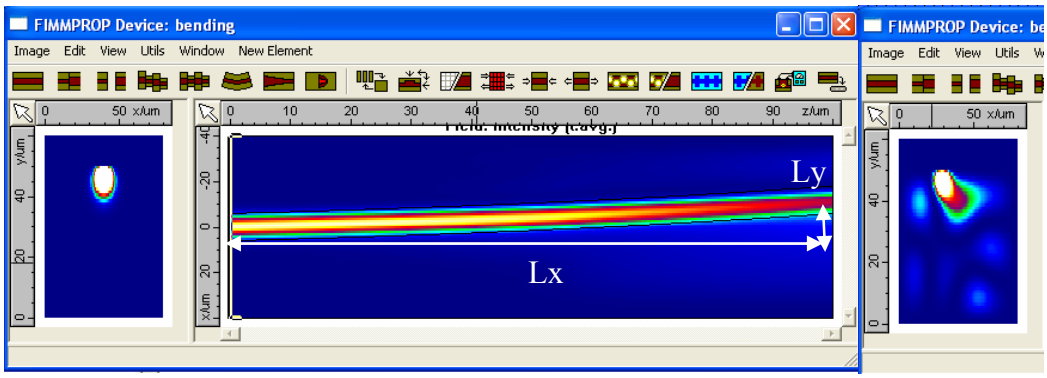

Fig. 1-16. The simulation of the bending loss of the Ti:LN waveguide. Left inset is the input mode. Right inset is the output mode shape. The leakage can be seen in the output mode.

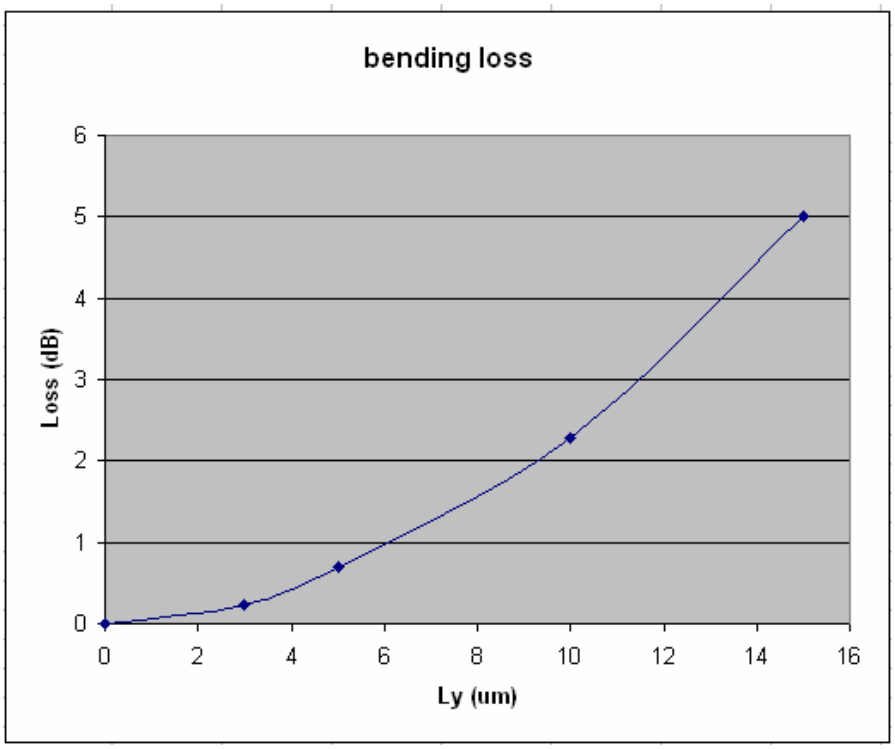

Fig. 1- 17. Bending loss estimation to the Ti:LN waveguide.

To overcome excessive bending loss, a new device other than full circle loop has been invented. The device is actually analyzed and fabricated as an all-pass filter (notch filter) in order to study it characteristics as a loop resonator. The detailed structure is shown in Fig.1-18. It is composed of one straight-through bus waveguide coupled to a loop structure, which is made of two Y-junction reflectors connected by two waveguide branches. The Y-junction reflector, with metal-coated total reflective mirror at the facet, can reflect light from one arm totally to the other arm. With the help of Y-junction reflector, the attenuation in loop is reduced to avoid the bending loss. Such a device is also more compact compared to a circular loop. Input light is injected to the bus waveguide and then coupled onto the loop. Two electrodes are added to fine-tune the loop roundtrip phase and the power coupling ratio of the coupler. The details of the device will be discussed in Chapter 2 and 3.

A unique advantage of this device is that it is capable of high speed tuning with speed up to several GHz. Although it was not the original intent of the project, this ability might be very useful for the other applications, such as a high speed modulator which can simultaneously resonate at optical and RF signal. [59] In this thesis, we also investigate the implementation of high frequency electrode to the loop and evaluate the high speed modulation.

Since the facility in UCSD does not support lithium niobate waveguide fabrication, we cooperated with New Technology Laboratories, Sumitomo Osaka Cement Co., Ltd and National Institute of Information and Communications Technology in Japan to fabricate the device and to conduct some of the basic testing.

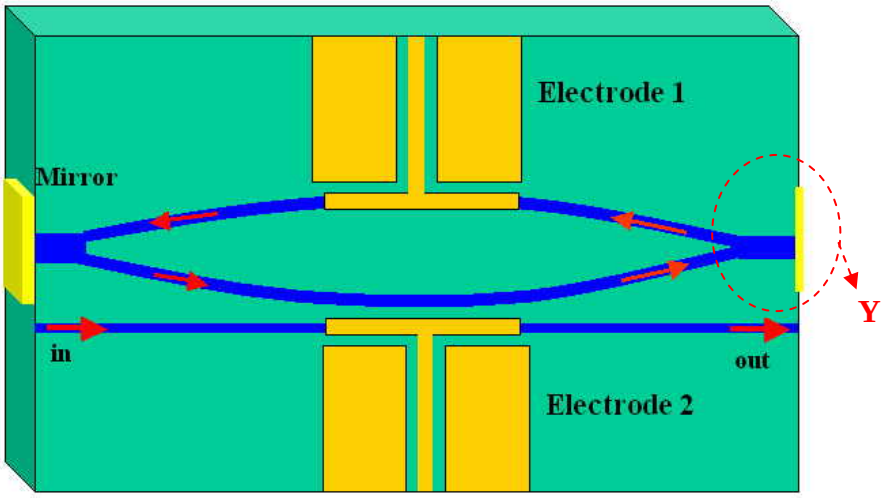

Fig. 1-18. Schematic diagram of the APF based on the tunable lithium niobate loop resonator. Y represents the Y-junction reflector.

1.4 Thesis Outline

In chapter 2, the design issues of the tunable lithium niobate loop will be discussed in detail, including the material property, optical structure design, and the electrode design. In chapter 3, the measurement results of devices from two different iterations will be presented together with the device analysis. The possible extension of the technique to a novel 1xN splitter is also discussed. In chapter 4, a novel optical RF notch filter for the incoherent filtering based on DGD units is proposed and demonstrated. The summary and future works are given in chapter 5.

Reference

[1] Rajiv Ramaswami, "Optical Fiber Communication: From Transmission to Networking", IEEE Commun. Mag., 50th Anniversary Commemorative Issue, pp 138-147, May 2002.

[2] Makoto Shibutani, Toshihito Kanai, Watani Domom, Katsumi Emura, and Junji Namiki, "Optical Fiber Feeder for Microcellular Mobile Communication Systems (H-015)", IEEE J. Selected Areas In Comm., Vol. 11, No. 7, Sept. 1993.

[3] John O'Reilly and Phil Lane, "Remote Delivery of Video Service Using mm-Waves and Optics", J. Lightwave Tech., Vol. 12**,** No. 2, pp 369-375, Feb. 1994.

[4] L. Noel, D. Wake, D. G. Moodie, D. D. Marcenac, L. D. Westbrook, and D. Nesset, "Novel Techniques for High-Capacity 60-GHz Fiber-Radio Transmission Systems", IEEE Trans. Microwave Theory Tech., Vol. 45, No. 8, pp 1416-1423, Aug. 1997.

[5] Jiunn-Shyen Wu, Jingshown Wu, and Hen-Wai Tsao, "A Radio-over-Fiber Network for Microcellular System Application", IEEE Trans. Vehicular Tech., Vol. 47, No.1, pp 84-94, Feb. 1998.

[6] Robert A. Griffin, H. M. Salgado, P. M. Lane, and J. J. O'Reilly, "System Capacity for Millimeter-Wave Radio-Over-Fiber Distribution Employing an Optically Supported PLL", J. Lightwave Tech., Vol. 17, No. 12, pp 2480-2487, Dec. 1999.

[7] Christina Lim, Ampalavanapillai Nirmalathas, Dalma Novak, Rod Waterhouse, and Gideon Yoffe, "Millimeter-Wave Broad-Band Fiber-Wireless System Incorporating Baseband Data Transmission over Fiber and Remote LO Delivery", J. Lightwave Tech., Vol. 18, No. 10, pp 1355-1363, Oct. 2000.

[8] Hong Bong Kim, Marc Emmelmann, Berthold Rathke, and Adam Wolisz, "A Radio over Fiber Network Architecture for Road Vehicle Communication Systems", In Proc. of IEEE Vehicular Technology Conference, VTC 2005 Spring., 2005.

[9] G. E. Betts, L. M. Johnson, and C. H. Cox, III, "Optimization of Externally Modulated Analog Optical Links", Proc. SPIE Vol. 1562, pp281-302, 1991.

[10] J. A. Chiddix, H. Laor, D. M. Pangrac, L. D. Williamson, and R. W.Wolfe, "AM Video on Fiber in CATV Systems: Need and Implementation", IEEE J. Select. Areas Commun., Vol. 8, pp1229-1239, 1990.

[11] R. H. Buckley, E. R. Lyons, and g. Goga, "A Rugged Twenty Kilometer Fiber Optic Link for 2 to 18 Gigahertz Communications", Proc. SPIE, Vol. 1371, pp. 212-222, 1990.

[12] H. F. Taylor, “Application of Fiber Optic Delay Lines and Semiconductor Optoelectronics to Microwave Signal Processing”, Proc. SPIE, Vol. 1371, pp 150-160, 1990.

[13] W. Ng, G. Tangonan, A. Walston, I. Newberg, J. J. Lee, and N. Bernstein, “True-time-delay Steering of Dual Band Phased Array Antenna Using Laser-Switched Optical Beam Forming Networks”, Proc. SPIE, Vol. 1371, pp 205-211, 1990.

[14] J. Capmany, B. Ortega, D. Pastor, and S. Sales, “Discrete-time optical processing of microwave signals”, J. Lightwave Technol., Vol. 23, No. 2, pp. 702-723, 2005.

[15] Kalman Wilner, and Anthony P. Van Den Heuvel, “Fiber-Optic Delay Lines for Microwave Signal Processing”, Proc. IEEE, Vol. 64, No. 5, pp805-807, May 1976.

[16] J. Capmany, D. Pastor, B. Ortega, and S. Sales, “Optical Processing of Microwave Signals”, in Dig. Int. Topical Meeting MWP’00, pp. 241–244, 2000.

[17] K. Jackson, S. Newton, B. Moslehi, M. Tur, C. Cutler, J. Goodman and H. J. Shaw, “Optical fiber delay-line signal processing”, IEEE Trans. Microwave Theory Tech, Vol. 33, pp. 193-204, 1985

[18] M. Tur, J. W. Goodman, B. Moslehi, J. E. Bowers, and H. J. Shaw, “Fiber-optic signal processor with applications to matrix-vector multiplication and lattice filtering,” Optics Letters, vol. 7, no. 9, pp 463-465, 1982.

[19] S. A. Newton, R. S. Howland, K. P. Jackson, and H. J. Shaw, “High-speed pulse train generation using single-mode fiber recirculating delay lines,” Electronics Letters, vol. 19, pp.756-758, 1983.

[20] B. Moslehi, J. Goodman, M. Tur and H. J. Shaw, Fiber-optic lattice signal processing, Proc. IEEE, Vol. 72, pp. 909-930, 1984

[21] R. Minasian, “Photonic signal processing of high-speed signals using fibre gratings”, Optical Fiber Technology, pp. 91-108, 2000.

[22] R. A. Minasian, K. E. Alameh, and E. H. W. Chan, “Photonics-based interference mitigation filters”, IEEE Trans. Microwave Theory Tech., pp. 1894-1899, 2001.

[23] F. Coppinger, A. Bushan, and B. Jalali, “Photonic time stretch and its application to analog-to-digital conversion”, IEEE Trans. Microwave Theory Tech., pp. 1309-14, 1999

[24] P. Juodawlkis, J. Twitchell, G. Betts, J. Hargreaves, R. Younger, J. Wasserman, F. O'Donnell, K. Ray, and R.C. Williamson, "Optically sampled analog-to-digital converters, IEEE Trans. Microwave Theory Tech., pp. 1840-1853, 2001.

[25] Y. Han and B. Jalali, "Photonic time-stretched analog-to-digital converter: fundamental concepts and practical considerations", J. Lightwave Technol., vol. 21, no. 12, pp. 3085-3103, 2003.

[26] H. Roussell and R. Helkey, "Optical frequency conversion using a linearized LiNbO3 modulator", IEEE Microwave Guided Wave Lett, pp. 408-410, 1998.

[27] B. Desormiere, C. Maerfeld, and J. Desbois, "An Integrated Optic Frequency Translator for Microwave Lightwave Systems", J. Lightwave Technol., vol. 8, No. 4, pp 506-513, April 1990.

[28] D. Hunter and R. Minasian, "Programmable high-speed optical code recognition using fibre Bragg grating arrays", Electron. Lett., pp. 412-414, 1999.

[29] J. Chou, Y. Han, and B. Jalali, "Adaptive RF-photonic arbitrary waveform generator", IEEE Photon. Technol. Lett., Vol. 15, No. 4, pp. 581-583, 2003.

[30] W. Wang, R. L. Davis, T. J. Jung, R. Lodenkamper, L. J. Lembo, J. C. Brock, and M. C. Wu, "Characterization of a Coherent Optical RF Channelizer Based on a Diffraction Grating", IEEE Trans. Microwave Theory and Tech., Vol. 49, No. 10, pp1996-2001, Oct. 2001.

[31] R. E. Saperstein, D. Panasenko, and Y. Fainman, "Demonstration of a Microwave Spectrum Analyzer Using Time-domain Processing in Optical Fibers", Opt. Lett., Vol. 29, No.5, pp501-503, Mar. 2004.

[32] V. Lavielle, I. Logere, J. –L. Le Gouet, S. Tonda, and D. Dolfi, "Wideband versatile radio-frequency spectrum analyzer", Opt. Lett., Vol. 28, No. 6, pp 384-386, Mar. 2003.

[33] D. A. Cohen, A. F. J. Levi, "Microphotonic components for a mm-wave Receiver", Solid-state Electron. Vol. 45, pp 495-505, 2001.

[34] E. Vourch, D. Le berre, and D. Herve, "Lightwave Single Sideband Wavelength Self-Tunable Filter Using and InP:Fe Crystal for Fiber-Wireless Systems", IEEE Photon. Technol. Lett., Vol. 14, No. 2, pp194-196, Feb. 2002.

[35] T. Kawanishi, S. Oikawa, and M. Izutsu, "Reciprocating Optical Modulation for Millimeter-wave Generation by Using a Dual-section Fiber Bragg Grating", J. Lightwave Tech., Vol. 20, No. 8, pp 1408-1414, Aug. 2002.

[36] C. R. Mirasso, “Chaotic Optical Communications”, IEEE LEOS Newsletter, pp12-14, Feb. 2005.

[37] E. Genin, L. Larger, J.-P. Goedgebuer, M. W. Lee, R. Ferriere, and X. Bavard, “Chaotic Oscillations of the Optical Phase for Multigigahertz-Bandwidth Secure Communications”, IEEE J. Quan. Electron., Vol. 40, No. 3, pp294-298, Mar. 2004.

[38] H. Zmuda, R. Soref, P. Payson, S. Johns, and E.N. Toughlian, "Photonic beamformer for phased array antennas using fibre grating prism", IEEE Photon. Technol. Lett., pp. 241-243, 1997.

[39] W. Zhou, and S. Weiss, “A low-cost optical controlled phased-array antenna with optical true-time-delay generation”, Proc. SPIE, Vol. 4998, pp133-138, Jul. 2003.

[40] N. Dagli, “Wide-Bandwidth Lasers and Modulators for RF Photonics”, IEEE Trans. Microwave Theory and Tech., Vol. 47, No. 7, pp1151-1171, Jul. 1999.

[41] D. Tauber, and J. E. Bowers, “Dynamics of Wide Bandwidth Semiconductor Lasers”, Int. J. High Speed Electron. Syst., Vol. 8, No. 3, pp. 377-416, 1997.

[42] G. L. Li, and P. K. L. Yu, “Optical Intensity Modulators for Digital and Analog Applications”, J. Lightwave Technol., Vol. 21, No. 9, pp2010-2030, Sept. 2003.

[43] K. Kato, “Ultrawide-Band/High Frequency Photodetectors”, IEEE Trans. Microwave Theory Tech., Vol. 47, No. 7, pp 1265-1281, Jul. 1999.

[44] M. Makimoto, and S. Yamashita, “Microwave Resonators and Filters for Wireless Communication: Theory, Design and Application”, Springer series in advanced microelectronics, ISBN 3540675353, 2000.

[45] S. Sales, J. Capmany, J. Marti, and D. Pastor, “ Experimental Demonstration of Fibre-Optic Delay Line Filters with Negative Coefficients”, Eletron. Lett., Vol. 31, pp 1095-1096, 1995.

[46] F. Coopinger, S. Yegnanarayanan, P. D. trinh, and B. Jalali, “ All-optical Incoherent Negative Taps for Photonic Signal Processing”, Eletron. Lett., Vol. 33, pp 973-975, 1997.

[47] Robert A. Minasian, Kamal E. Alameh, and Erwin H. W. Chan, “Photonics-based interference mitigation filters”, IEEE Trans. Microwave Theory and Tech., vol. 49, No.10, pp1894, Oct. 2001.

[48] D. Hunter and R. Minasian, "Reflectively tapped fiber optic transversal filter using in-fiber Bragg gratings", Electron. Lett., Vol. 31, pp. 1010-1012, 1995

[49] Jose Capmany, Daniel Pastor, and Beatriz Ortega, "New and flexible fiber-optic delay-line filters using chirped Bragg gratings and Laser arrays", IEEE Trans. On Microwave theory and tech., vol. 47, No. 7, pp1321, Jul. 1999

[50] F. Coppinger, C. K. Madsen, and B. Jalali, "Photonic Microwave Filtering Using Coherently Coupled Integrated Ring Resonators", Microwave and Optical Technol. Lett., Vol. 21, No.2, pp90-93, April 1999.

[51] A. Yariv, "Universal relations for coupling of optical power between microresonators and dielectric waveguides", Electron. Lett. Vol. 36, pp. 321-322, Feb. 2000.

[52] H. Li, K. Ogusu, "Analysis of optical instability in a double-coupler nonlinear fiber ring resonator", Optics Communications, Vol. 157, pp. 27-32, Dec. 1998.

[53] K. Oda, N. Takato, and H. Toba, "A wide-FSR Waveguide Double-Ring Resonator for Optical FDM Transmission Systems", J. Lightwave Technol., Vol. 9, No. 6, pp728-736, 1991.

[54] S. Suzuki, K. Oda, and Y. Hibino, "Integrated-Optic Double-Ring Resonators with a Wide Free Spectral Range of 100GHz", J. Lightwave Technol., Vol. 13, No.8, pp1766-1771, 1995.

[55] B. Little, "A VLSI Photonics Platform", Optical Fiber Communication Conference 2003, Invited Talk, pp 1-3, 2003.

[56] W. D. Jemison, P. R. Herczfeld, W. Rosen, A. Vieira, A. Rosen, A. Paolella, A. Joshi, "Hybrid Fiberoptic-millimeter-wave links", IEEE Microwave Magazine, Vol. 1, pp 44-51, Jun. 2000.

[57] T. Kominato, Y. Ohmori, N. Takato, H. Okazaki, and M. Yasu, "Ring resonators composed of GeO_2-doped Silica waveguides", J. Lightwave Technol., Vol. 10, pp. 1781-1788, Dec. 1992.

[58] B. Moslehi, and J. W. Goodman, "Novel amplified fiber-optic recirculating delay line processor", J. Lightwave Technol., Vol. 10, pp 1142-1147, Aug. 1992.

[59] D. A. Cohen, M. Hossein-Zadeh, A. F. J. Levi, "High-Q microphotonic electro-optic modulator", Solid-State Electron., Vol. 45, pp1577-1589, 2001.

[60] P. Ganguly, J. C. Biswas, and S. K. Lahiri, “Modelling of Titanium Indiffused Lithium niobate Channnel Waveguide Bends: a Matrix Approach”, Optic. Comm., Vol. 155, pp125-134, 1998.

Chapter 2. Lithium Niobate Loop Resonator Design

In this chapter, the lithium niobate material properties, Titanium diffused waveguide characteristics, the coupling section design, the electrode design, and the Y-junction reflector (Y-reflector) design will be discussed in detail. The frequency tunability of the tunable lithium niobate loop is theoretically predicted.

2.1 Material Properties of Lithium Niobate

Ever since 1964, the piezoelectric, electro-optic properties of single crystal lithium niobate (LN) have been extensively investigated. Lithium niobate has been used in many applications such as acoustic transducers, electro-optic modulators, waveguide, nonlinear optical devices, holographic storage devices, and so on. [1] Detailed information about properties of lithium niobate is found in handbooks. [2] In this chapter, we will only discuss briefly some important aspects of the properties to understand the electro-optic properties of Titanium (Ti) diffused lithium niobate waveguide.

High purity lithium niobate crystal is generally grown by Czochralski technique. [3-4] It looks like a transparent crystal with hardness similar to that of soft glass, as shown in Fig. 2-1. Its lattice structure is depicted in Fig. 2-2. Its unit cell is characterized by six plane layers of oxygen spaced 0.232 nm apart along the z-axis.

The oxygen ions in each layer are arranged in a triangle with every other layer rotated by 180° so that the six oxygen atoms in adjacent layers form an octahedron. The center of the octahedron is occupied either by Li or Nb ion or just vacancy, in the order of Nb, V, Li, Nb, V, Li…, where V is vacancy. This structure makes the crystal possess large local polarization for its permittivity. Consequently, lithium niobate is an anisotropic crystal.

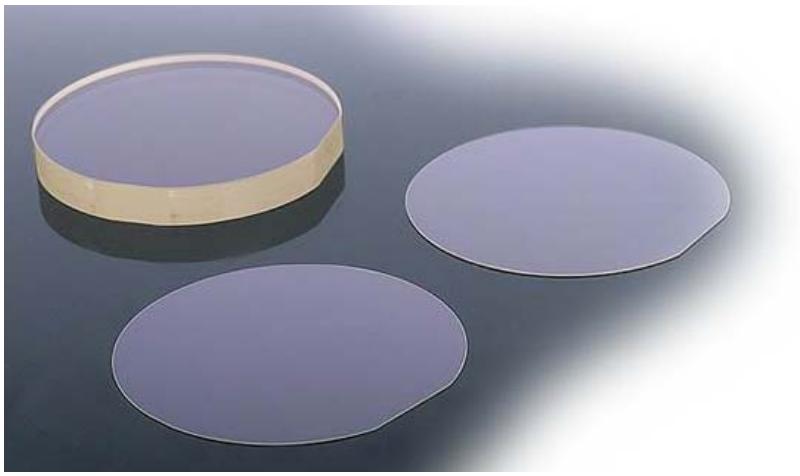

Fig. 2-1. Appearance of lithium niobate crystal wafer.

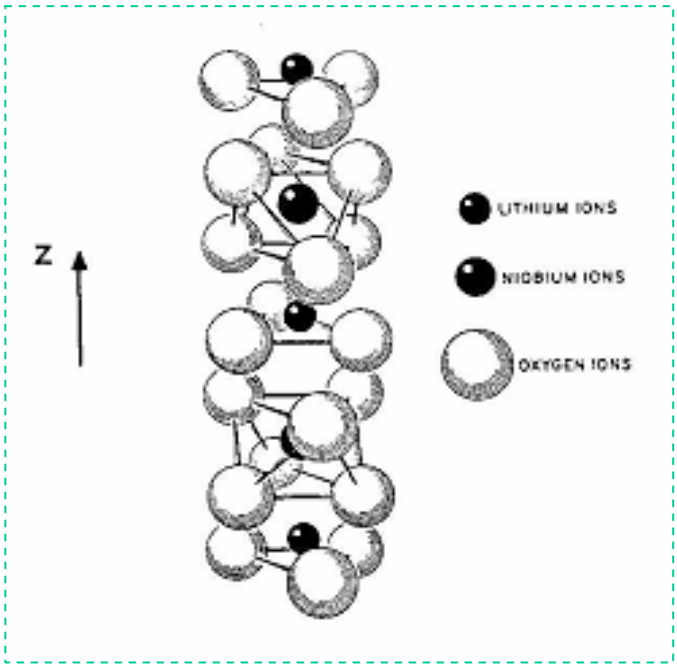

Fig. 2-2. Lattice structure of lithium niobate crystal.

The electric displacement vector $\vec{D}$ and the electric field $\vec{E}$ inside a lithium niobate crystal is related by

$$\vec{D} = \varepsilon_r \varepsilon_0 \vec{E} \qquad (2.1)$$

where ε_0 is the permittivity of vacuum. The dielectric constant tensor ε_r, referred to its principal axes, has three independent components:

$$\varepsilon_r = \begin{bmatrix} \varepsilon_x & 0 & 0 \\ 0 & \varepsilon_y & 0 \\ 0 & 0 & \varepsilon_z \end{bmatrix} \qquad (2.2)$$

As lithium niobate is a crystal with point group 3m symmetry, $\varepsilon_x = \varepsilon_y$, it is a uniaxial crystal. For light polarizes along one of the principal axes, it sees the refractive index given by $n_i = \sqrt{\varepsilon_i}$, for i=x,y,z. For arbitrarily polarized light, the index is described through the index ellipsoid. [5] For a uniaxial crystal like LN, the index ellipsoid is given by

$$\frac{x^2}{n_o^2} + \frac{y^2}{n_o^2} + \frac{z^2}{n_e^2} = 1 \qquad (2.3)$$

where $n_o = n_x = n_y$ is called ordinary index and $n_e = n_z$ is the extraordinary index. For the wavelength ranges from 1.3 μm to 1.6 μm, $n_o = 2.22$ and $n_e = 2.14$ are generally good approximations at room temperature.

Because of its piezo-electric properties, the index ellipsoid of lithium niobate varies with the applied electric field. The new index ellipsoid is given by

$$\left(\frac{1}{n_o^2} - r_{22}E_y + r_{13}E_z\right)x^2 + \left(\frac{1}{n_o^2} + r_{22}E_y + r_{13}E_z\right)y^2 + \left(\frac{1}{n_e^2} + r_{33}E_z\right)z^2 + 2r_{51}E_x xz - 2r_{22}E_x xy = 1 \qquad (2.4)$$

where E_i (i=x, y, z) is the applied electric field along the axes. r_{ij} are the terms of the electro-optic tensor. Typical values of r_{ij} are $r_{13} = 9.63\,pm/V$, $r_{22} = 6.81\,pm/V$, $r_{33} = 30.9\,pm/V$, and $r_{51} = 32\,pm/V$.

For devices in this dissertation, the substrate is cut perpendicular to the z-axis, i.e., the light travels in the xy plane and electric field is applied along z-axis, so that the electro-optic coefficient r_{33} and r_{13} is utilized for the TM and TE mode respectively. In this case, Ex and Ey are zero and the index ellipsoid is simplified as

$$\left(\frac{1}{n_o^2}+r_{13}E_z\right)x^2+\left(\frac{1}{n_o^2}+r_{13}E_z\right)y^2+\left(\frac{1}{n_e^2}+r_{33}E_z\right)z^2=1 \qquad (2.5)$$

Also,

$$\left(\frac{1}{n_e^2}+r_{33}E_z\right)^{-1/2}\approx n_e-\frac{1}{2}n_e^3r_{33}E_z \qquad (2.6)$$

$$\left(\frac{1}{n_o^2}+r_{13}E_z\right)^{-1/2}\approx n_o-\frac{1}{2}n_o^3r_{13}E_z \qquad (2.7)$$

The variation of the extraordinary and ordinary index is given by

$$\Delta n_e=-\frac{1}{2}n_e^3r_{33}E_z \qquad (2.8)$$

$$\Delta n_o=-\frac{1}{2}n_o^3r_{13}E_z \qquad (2.9)$$

The typical index variations as a function of E_z are plotted in Fig. 2-3.

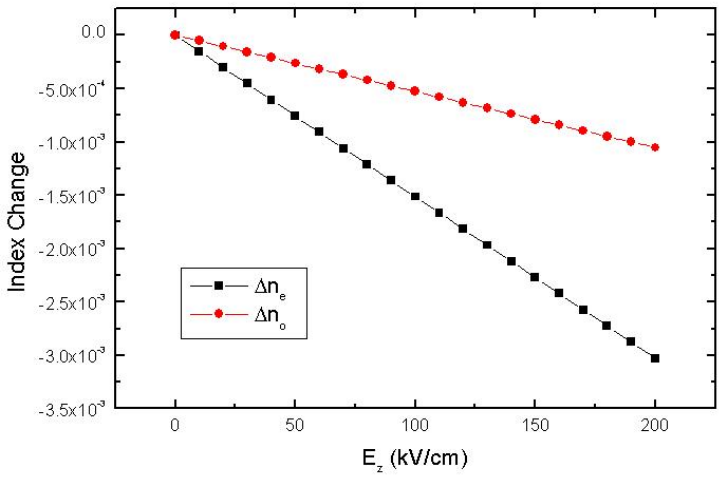

Fig. 2-3. Electro-optic effect of z-cut lithium niobate crystal.

The other important characteristic of the electrooptic effect of lithium niobate is that its dielectric constant is dependent on the frequency, i.e., it's a dispersive material because of its piezoelectric effect (f<1 MHz), acoustic resonance (1 MHz<f<50 MHz), ionic contribution (50 MHz<f<4 THz), and optical phonon resonance (4 THz<f<60 THz). [6] Fortunately, for the commonly used microwave frequency in the range of 0.1 GHz to 40 GHz and the infrared optical wavelength from 1.30 μm to 1.6 μm, the dielectric constants are relatively independent of the frequency. Dielectric constants at some typical RF's frequencies are listed in Table 2-1.

Table 2-1. Typical values of the relative dielectric constant for different frequencies. [After [2], p129]

Frequency	ε_x	ε_z
Low (100 kHz)	84.6	29.1
High (10 MHz)	44.3	27.6
0.1 GHz	44.1	23
1.0 GHz	43.9	23.7
9.0 GHz	42.5	26

2.2 The Titanium Diffused Lithium niobate Waveguide

There are two major methods to fabricate low loss optical waveguide on the lithium niobate substrate, proton exchange [7] and Titanium in-diffusion (Ti-diffused). The advantages of the proton exchange method are quick, simple, and low temperature. The expected waveguide area is exposed to the acids (Benzoic acid, for example) under the temperature of 160 °C to 249 °C. Ion exchange will happen between Li^+ and H^+. As the consequence, the high index area will form after several hours. Unfortunately, this method still has many disadvantages, including the instability of the index and reduced electro-optic activity.. Ti in-diffusion method requires much higher temperature (900 °C ~ 1100 °C). However, after cooling down, its index distribution is more stable than proton exchange. In this dissertation, we choose the Ti in-diffusion method to fabricate the waveguide.

The first Ti-diffused waveguide was reported in 1974. [8] Typically, a thin film (10-100 nm) of titanium is sputtered or evaporated on the surface of the lithium niobate substrate with a defined waveguide pattern. The diffusion is carried out in reactive or inert ambient at temperatures ranging from 900 °C to 1100 °C. Diffusion time t ranges from 0.5 to 30 hours. The diffusion profile is described by Fick's second law

$$\frac{\partial c}{\partial t} = D\nabla^2 c \qquad (2.10)$$

where c is the material concentration and D is the diffusion coefficient.

For an infinite large thin film, the source is written as

$c(y) = \delta(y)$ for t=0. (2.11)

The 1D solution of Fick's law is $c(y,t) = \frac{2}{\sqrt{\pi} d} e^{-y^2/d^2}$, where the diffusion length $d = 2\sqrt{Dt}$.

For a thin strip of material of thickness h, width w, and atomic density C_1, the 2D solution of Fick's law is [1]

$$c(y,x) = \frac{C_1}{\sqrt{\pi}} \frac{h}{d_y} e^{-y^2/d_z^2} \left[erf\left(\frac{w/2 + x}{d_x} \right) + erf\left(\frac{w/2 - x}{d_x} \right) \right] \qquad (2.12)$$

where erf is error function.

The characteristics of the Ti diffused lithium niobate waveguide can be simulated by FIMMWave. Fig. 2-4 depicts the cross-section of the waveguide used in FIMMWave. The substrate is z-cut lithium niobate wafer. The extraordinary light axis (n_e) is along y direction. The ordinary axis (n_o) is along x or z direction. The light propagation direction is in z direction. For the practical Ti diffused device, the dimensions of diffusion area are determined by equation (2.12). But FIMMWave program approximately uses a square shape box to truncate the diffusion area. The refractive index profile inside the box is determined by the Ti diffusion. The refractive index profile outside of the box is treated as linear decay between the indices of the box boundary and the substrate. As long as the box is big enough, the error caused by the truncation can be neglected. In our simulation, the Ti metal width is about 7 μm. A box with a 12 μm width and a 10 μm depth is good enough to approximate the Ti diffused waveguide.

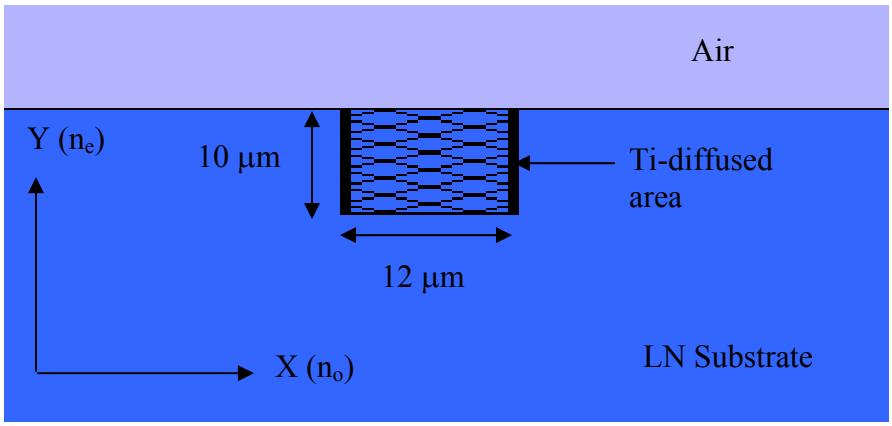

Fig. 2-4. The cross-section of the Ti diffused waveguide in the FIMMWave simulation program. The shade area is the square shape Ti diffused waveguide profile.

We first simulated the index profiles of the waveguide. As a good approximation to the fabrication conditions, the diffusion lengths of d_x=4.450 μm and d_y=4.0923 μm are input to FIMMWave. The optical wavelength is 1.55 μm. The ordinary index of the substrate n_o is 2.2125 and extraordinary index n_e is 2.1383. The maximum change of the n_o is 0.004548. The maximum change of the n_e is 0.009547. The maximum change of n_e is about twice of n_o, which implies that the TM mode is more strongly guided than the TE mode. The 3D profile of n_o and its 2D cut-view at the surface (y=50 μm) are shown in Fig. 2-5 (a) and (b), respectively. The plots for n_e are shown in Fig. 2-6 (a) and (b), respectively. From the 2D plot, we can see that the index profile outside the box is approximated as linear decay.

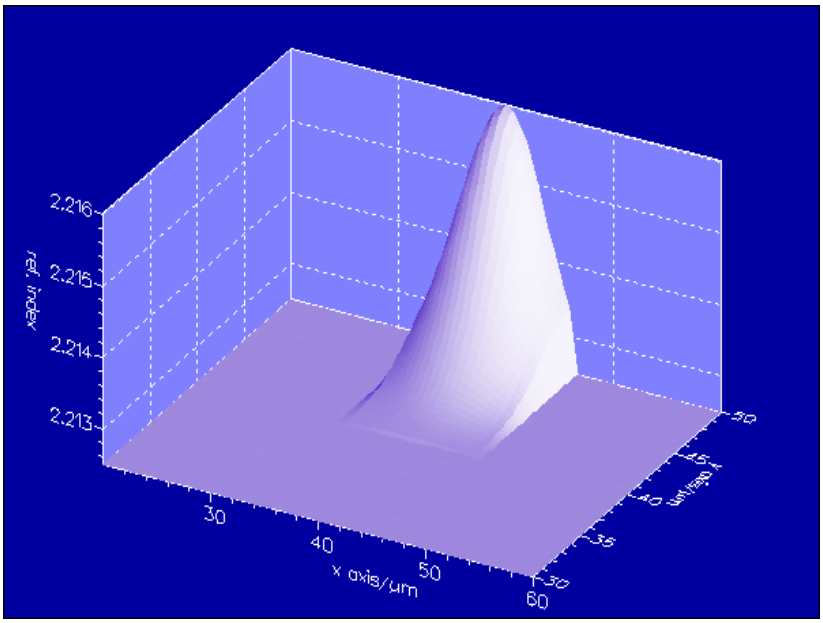

(a)

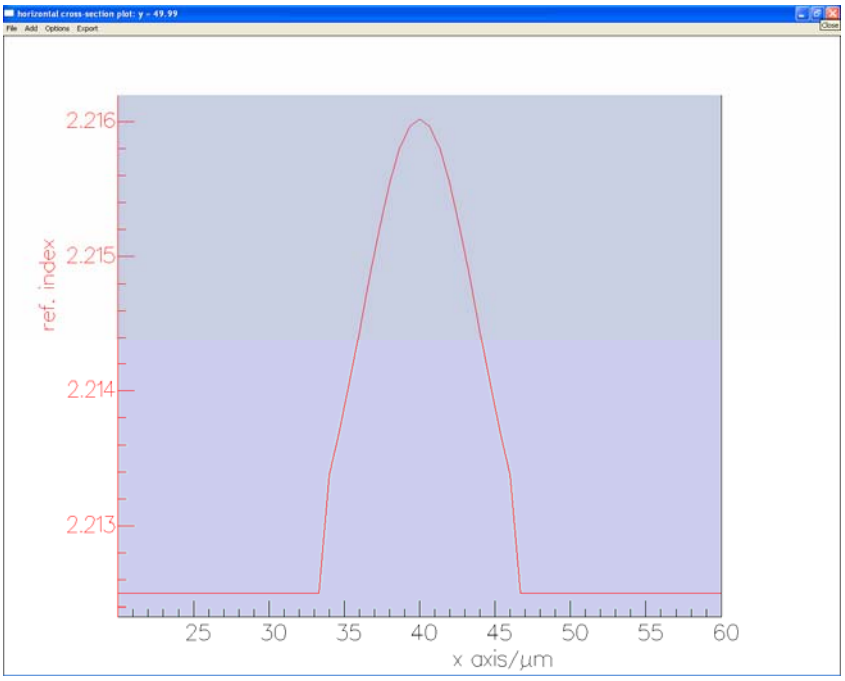

(b)

Fig. 2-5. Ordinary index profile of Ti:LN waveguide. (a) 3D, and (b) 2D cut-view at the surface (y=50 μm).

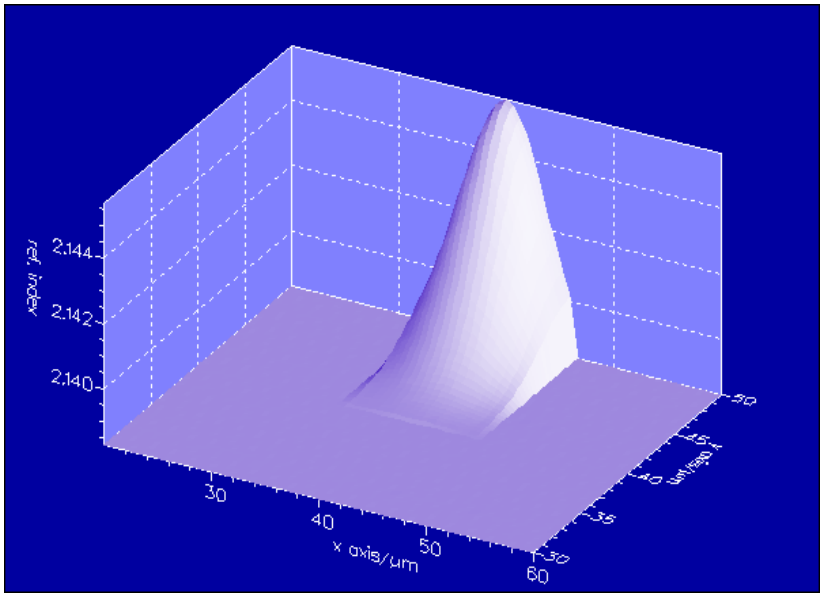

(a)

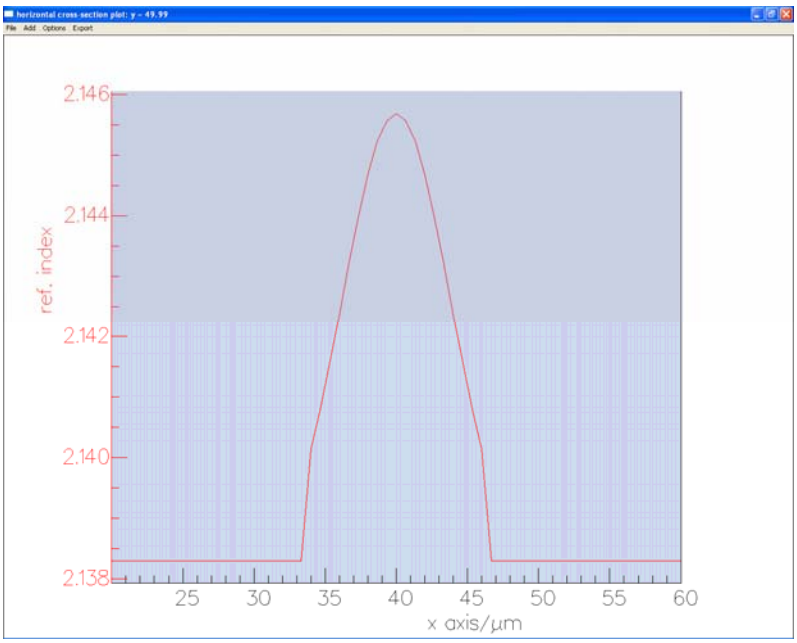

(b)

Fig. 2-6. Extraordinary index profile of Ti:LN waveguide. (a) 3D, and (b) 2D cut-view at the surface (y=50 μm).

The Ti:LN waveguide can support both TE and TM modes, which means the waveguide is sensitive to the light polarization and needs in-line polarization control in the measurement setup. To understand this, FIMMwave simulations have been done for the example waveguide mentioned above for both TE and TM fundamental mode. The intensity distribution of TE and TM modes are plotted in Fig. 2-7 (a) and (b), respectively. The most important component of the TE mode, Ex, is plotted in Fig. 2-8 with detailed cut-views for both the horizontal and vertical directions. For the TM mode, Hx is shown in Fig. 2-9.

From the mode profiles, it is easy to see that the TE mode is relatively much "bigger" than the TM mode. The reason is that the index change in ordinary index is much smaller than extraordinary, which means the waveguide is more weakly guided for the TE mode than the TM mode. Consequently, the TE mode spreads more widely than the TM mode. The mode size can be described by the full width of half maximum (FWHM). Table 2-2 lists the FWHM for the intensity, Ex of the TE mode and intensity, Hx of the TM mode. For our devices, in order to utilize the big electro-optic coefficient r_{33}, the TM mode is preferred to use for the design of the coupler and the Y-junction reflector.

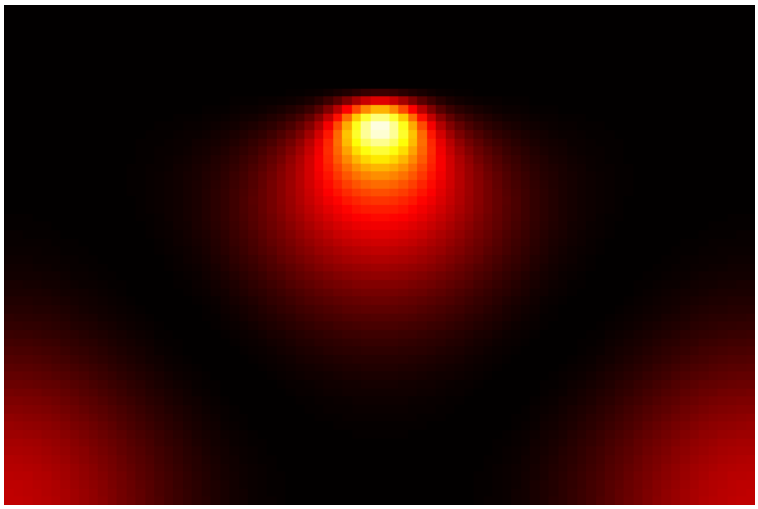

(a)

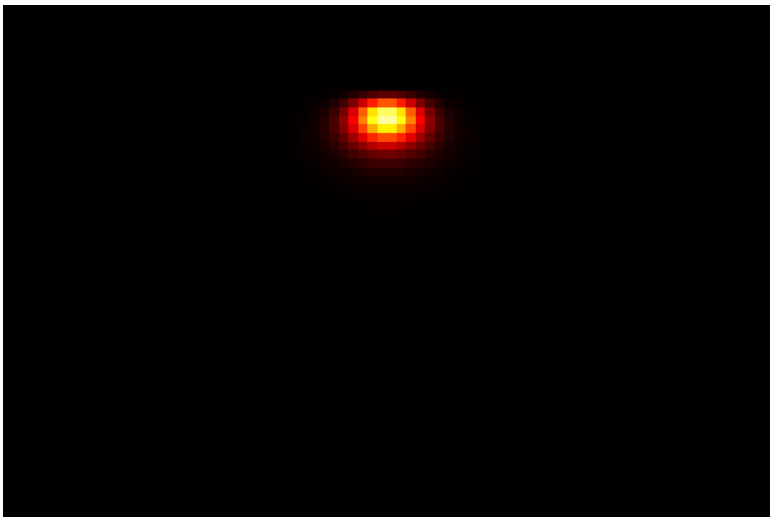

(b)

Fig. 2-7. Intensity profiles of (a) TE, and (b) TM mode. The horizontal and vertical are not to scale.

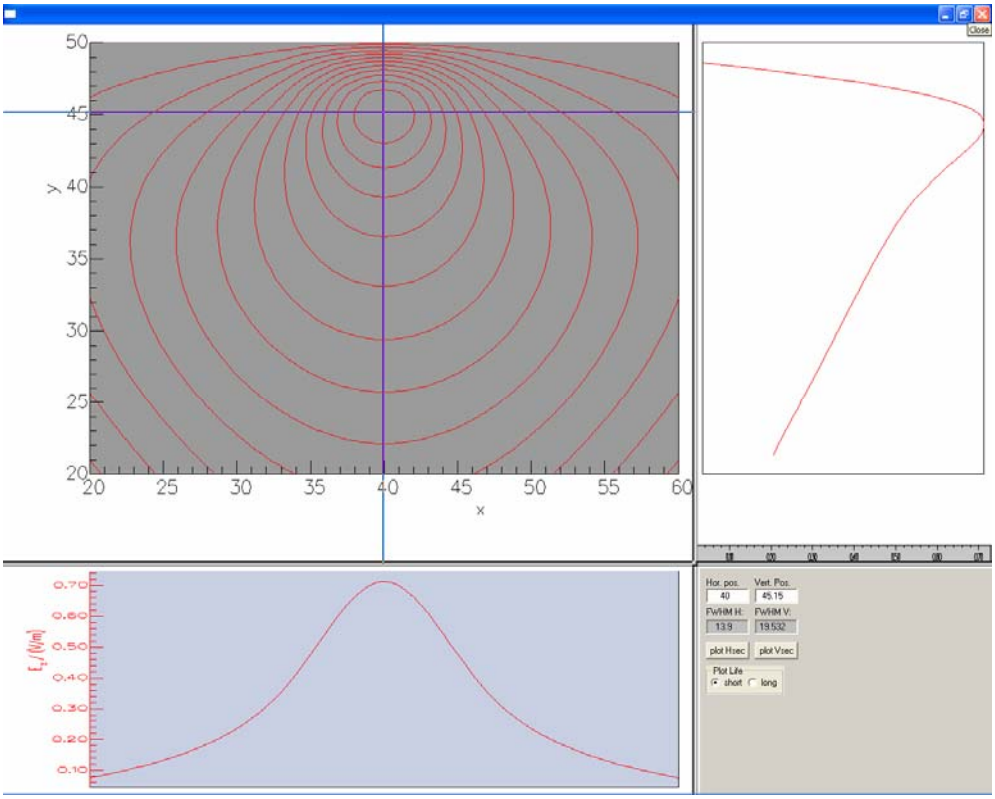

Fig. 2-8. Ex contour profile of TE mode. The crosses indicate the cross-sections in which the electric field variation is plotted. Horizontal cross-sectional profile is shown in the bottom and vertical cross-section profile is shown on right side.

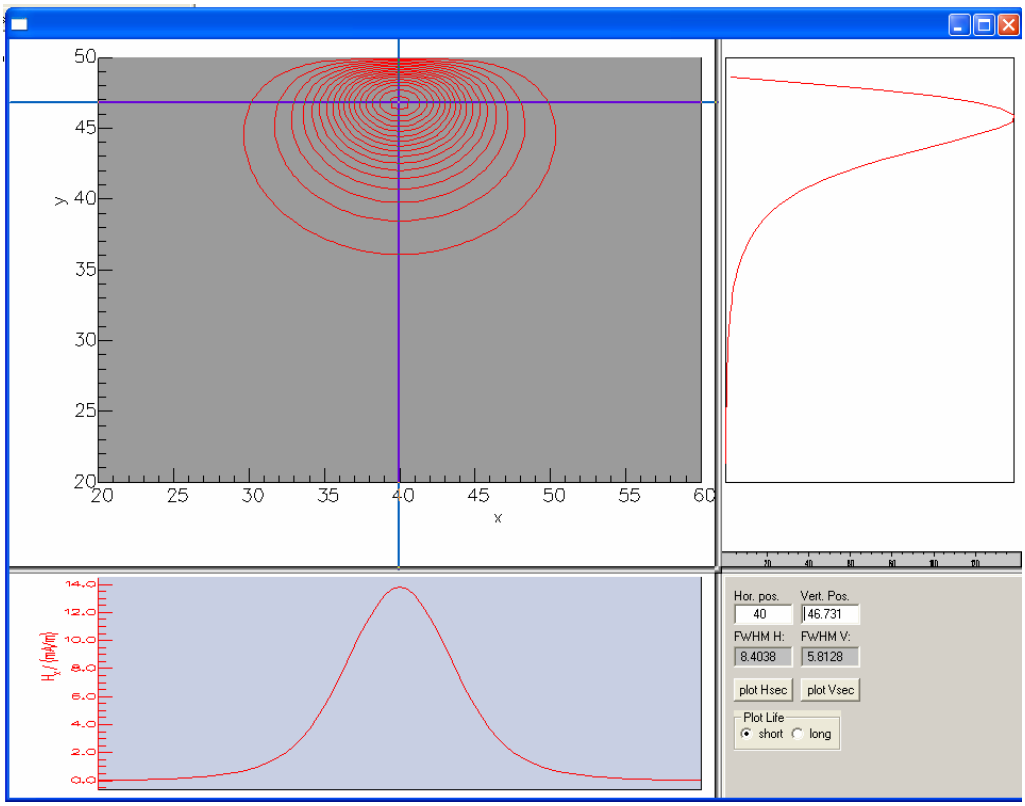

Fig. 2-9. Hx contour profile of TM mode. The crosses indicate the cross-sections in which the magnetic field variation is plotted. Horizontal cross-sectional profile is shown in the bottom and vertical cross-section profile is shown on right side.

Table 2-2. FWHM values in x and y direction for the TE and TM mode.

	FWHM x (μm)	FWHM y (μm)
TE intensity	8.809	10.22
TE Ex	13.9	19.532
TM intensity	5.8915	4.0654
TM Hx	8.4038	5.8128

2.3 Coupling Section Design

Directional coupler has been used extensively in passive optical component, for optical power splitting and coupling. The model of the coupler is well-established. [9] As shown in Fig. 2-10, the complex amplitudes of the input and output light are related by the following equations

$$\begin{bmatrix} E_2 \\ E_4 \end{bmatrix} = \begin{bmatrix} A & -jB \\ -jB^* & A^* \end{bmatrix} \begin{bmatrix} E_1 \\ E_3 \end{bmatrix} \tag{2.13}$$

The matrix elements are given by

$$A = \cos(L\sqrt{\kappa^2 + \delta^2}) + j\delta \sin(L\sqrt{\kappa^2 + \delta^2}) / \sqrt{\kappa^2 + \delta^2} \tag{2.14}$$

$$B = \kappa \sin(L\sqrt{\kappa^2 + \delta^2}) / \sqrt{\kappa^2 + \delta^2} \tag{2.15}$$

where κ is the coupling coefficient, L is the coupling length, and δ is the difference of the propagation constants of two branches. $\delta = (\beta_1 - \beta_2)/2 = \frac{\pi}{\lambda}(n_1 - n_2) = \frac{\pi}{\lambda}\Delta n$, where n is the refractive index and λ is the wavelength. Equation (2.15) implies that the power coupling ratio, defined by $|B|^2$, of the coupler can be fine-tuned if we can change the refractive index in one branch.

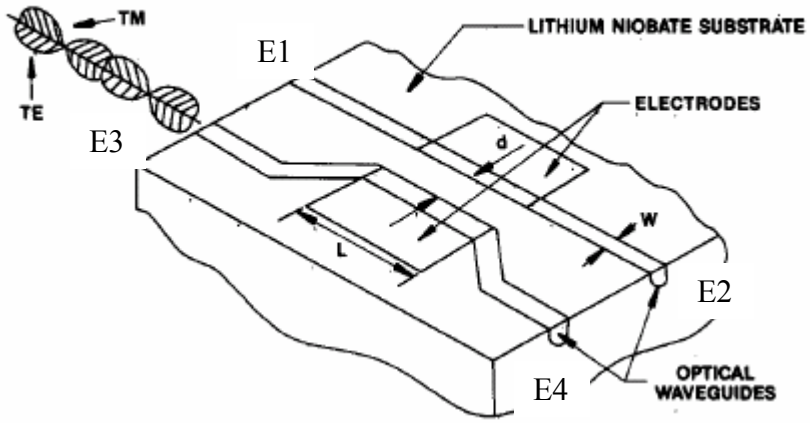

Fig. 2-10. Schematic view of the directional coupler based on Ti:LN waveguide. After [9] The coupler section with length L is connected to the input and output waveguides by waveguide bends.

When δ=0, and $\cos(L\kappa) = 0$, light will be completely coupled from one branch to the other branch.

The coupling coefficient κ is related to the separation distance between two waveguides d as

$$\kappa = \kappa_0 e^{-d\gamma_0} \qquad (2.16)$$

where κ_0 and γ_0 are parameters generally determined by experimental measurement.

In order to minimize the bending loss, the coupling section in our device is not made of two parallel waveguides with separation distance d, connected to input and output waveguides by sharp waveguide bends. In practice, one waveguide is bended

down slowly and gets closer and closer to the other parallel straight waveguide on the input side. Part of such pattern can be seen in the photo of the waveguides used in the first generation device in Fig. 2-11. In this case, d is the minimum distance between the bending waveguide and the straight-through bus waveguide. The coupling interaction takes place gradually along the direction of propagation where κ is a function of the distance.

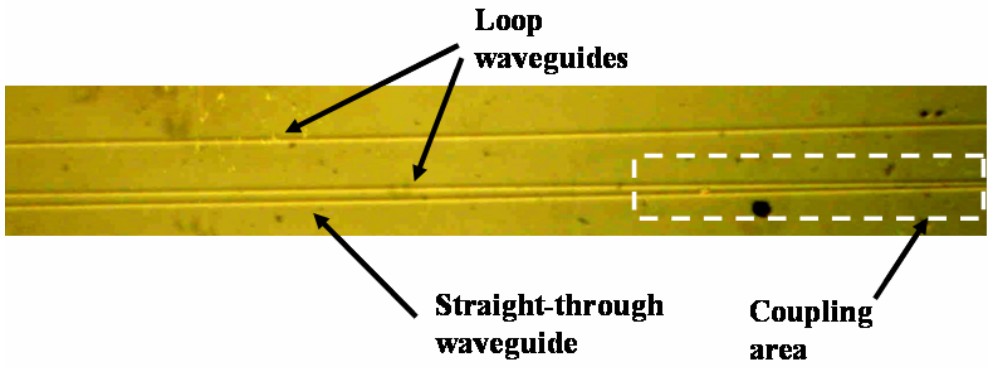

Fig. 2-11. Top view of the Ti:LN waveguides. The minimum gap distance at the coupling area is about 4 μm.

It is hard to get an analytical expression for the coupling coefficient as a function of distance or the power coupling ratio in this case. We first fabricated the test device by error-and-try experiments in Sumitomo Company. Then the devices are simulated by FIMMWave at UCSD.

The FIMMWave model of the coupler is shown in Fig. 2-12. The cross-section area of the waveguide is still 12 μm x 10 μm. The Ti strip width is set at 7 μm. Although two waveguides appear to be touching at the middle in Fig. 2-12, the gap

between two Ti strips is actually 4 μm. The total horizontal length is 3600 μm. The gap between the Ti strips at the output port is 10.5 μm. The input light is injected from the left end of the straight-through bus waveguide. The output is monitored at the right end of the bending waveguide. The bending shape is set as an exponential decay function.

The simulation results for the TM modes with d=4, 5, 6 μm are shown in Fig. 2-13 (a), (b), and (c), respectively. More simulation data can be found in Fig. 2-14. The power coupling ratio varies from 93.5% to 52.3% with the gap increasing from 4 to 6 μm.

We have measured the first generation demo devices with d=4.0, 4.1, and 4.2 μm, respectively. The power coupling ratios are 91.5%, 93.4%, and 92.5%, respectively, very close to the simulation results. We also have measured a second generation demo device with the gap of about 6 μm. The measured power coupling ratio is about 80%, which is larger than the simulated result 52%. The discrepancy may be caused by the SiO_2 layer on the surface and the gold electrode on the bus waveguide for the real device but lack in the simulation structure.

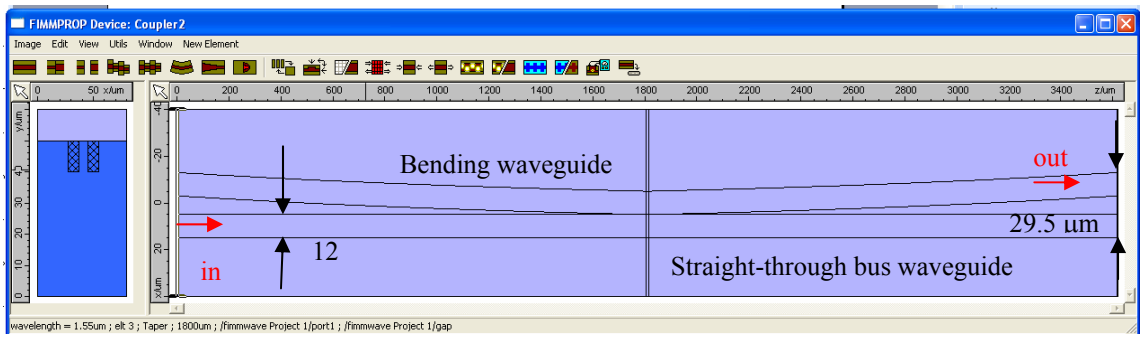

Fig. 2-12. Coupler model in FIMMWave simulation. The inset to the left is the waveguide cross-section at the input or output port.

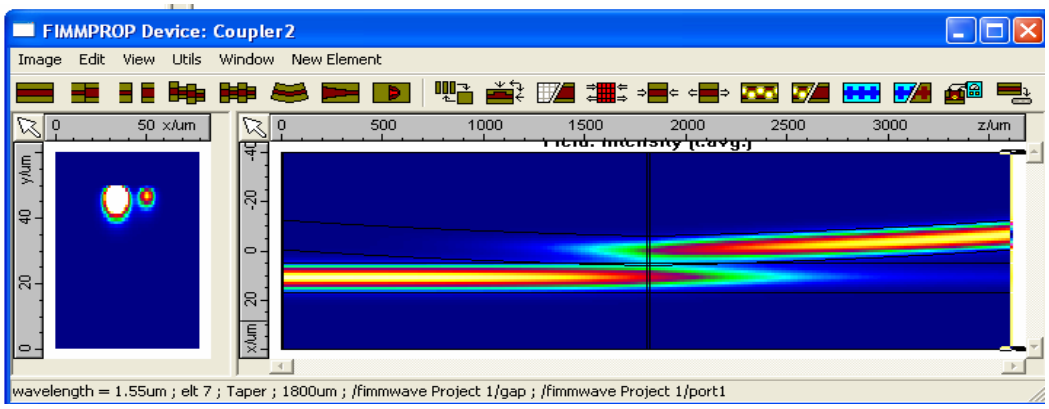

(a)

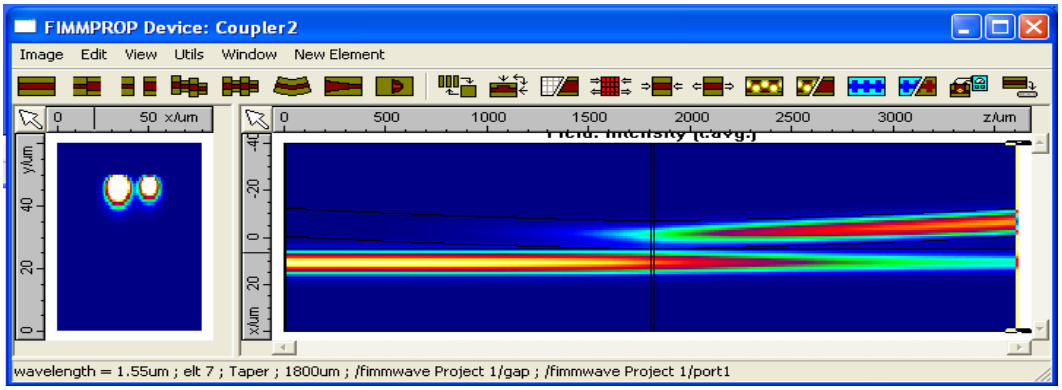

(b)

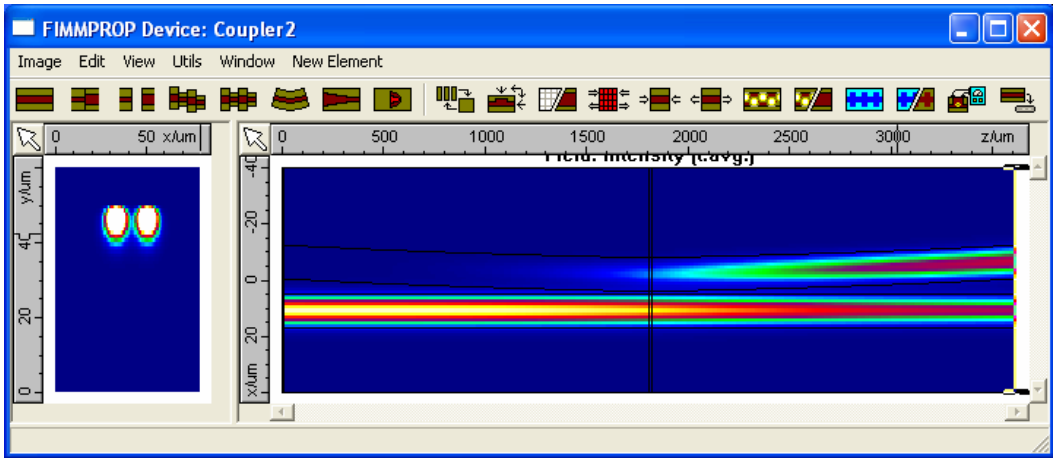

(c)

Fig. 2-13. Coupler transmission simulation for TM mode with (a) d=4 μm, (b) d=5 μm, and (c) d=6 μm. The inset to the left is the output modes for the bending (left) and bus waveguide (right), respectively.

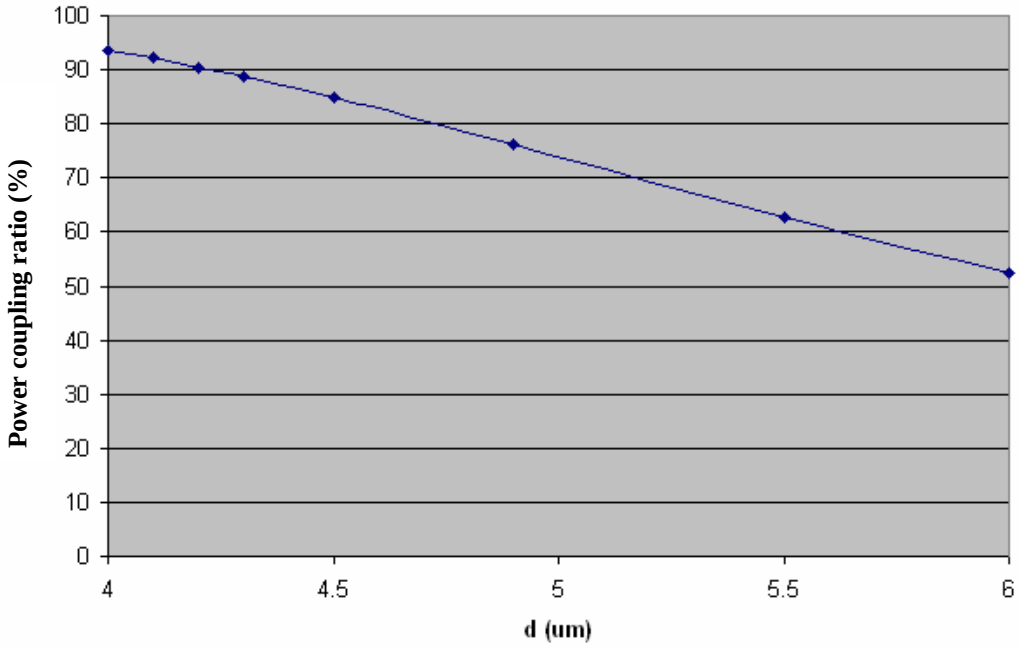

Fig. 2-14. Power coupling ratio varies with coupler gap d.

2.4 The Y-junction Reflector

Y shaped waveguide junctions have been extensively used as power splitting/coupling components and polarization mode splitter. The coupled mode analysis of the Y-junctions has been discussed thoroughly in the literatures. [10-16] By incorporating a metal mirror at the output facet, a Y-junction reflector (Y-reflector) can be formed. Our goal is to guide the light as much as possible from one branch to the other branch. Y-reflector has been used in applications such as Acousto-optic filter. [17] To our knowledge, this is the first time that the Y-reflectors have been used to obtain a loop resonator.

A traditional Y-junction, shown in Fig. 2-15, consists of 3 sections, a branching section, a tapered section, and a straight guide section. [16] According to the super mode theory, the Y-junction is actually a four-port device, including two incident ports, one output port, and one radiation port, as shown in Fig. 2-16. [16] Assuming the light injects from port I, it excites one even super mode and one odd super mode. If the straight guide section is a single mode waveguide, the even mode will be converted to the fundamental mode while the odd mode will radiate away. This may cause large insertion loss in power. In order to reduce the loss, the tapered section and straight waveguide are generally wide enough in our device to tolerate both even and odd mode, as shown in Fig. 2-17. The sharp bending between the tapered section and straight guide section is also avoided.

The most important characteristic of the Y-reflector is its insertion loss, defined by the ratio between the output power at the lower branch in Fig. 2-17 and the input power at the upper branch. The lowest propagation loss is reported at about 0.15 dB when the Y-junction is used as a TE and TM mode splitter. [17] The insertion loss includes the contributions from the radiation loss and the splitting ratio of the reflection light between two branches. It is mainly determined by the structure parameters such as the branch angle θ, the converging gap g, the minimum taper width w, and the taper length L.

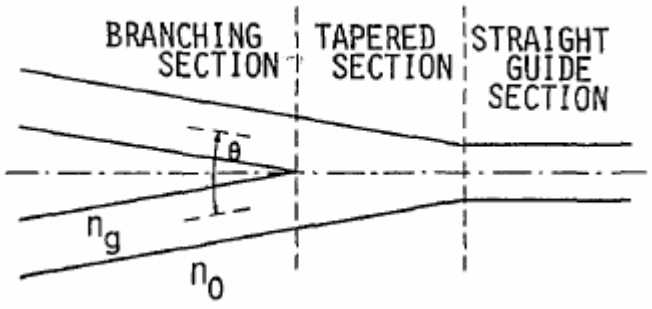

Fig. 2-15. The basic structure of Y-junction waveguide. After [16].

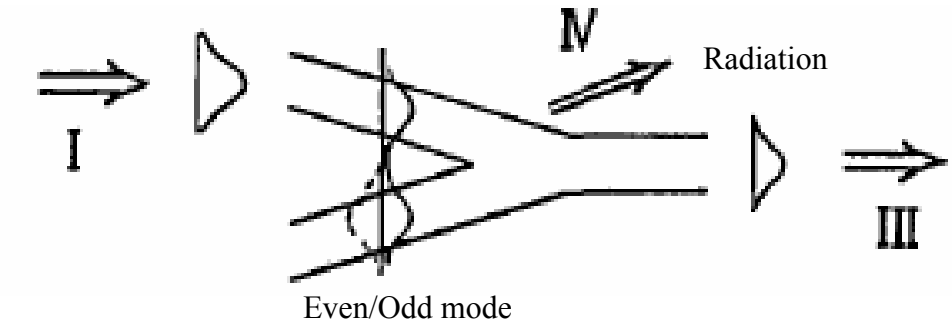

Fig. 2-16. Couple mode model of the Y-junction. After [16].

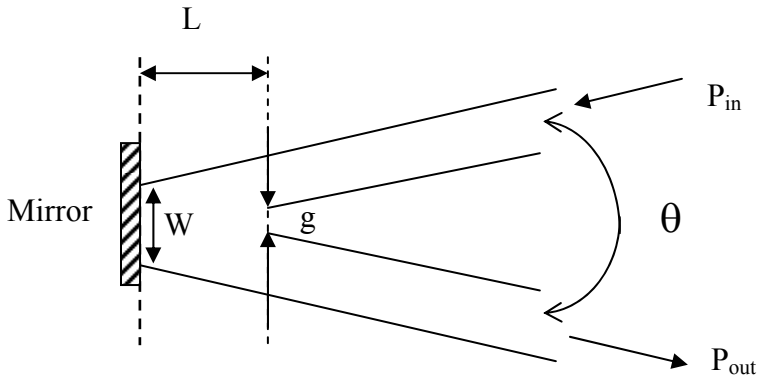

Fig. 2-17. Schematic view of the Y junction reflector.

Assuming the mirror has 100% reflectivity, the operation of the Y-reflector is understood by drawing a symmetric "image" Y-junction connected to the original one back-to-back, so that the reflection analysis is converted to the transmission analysis, as shown in Fig. 2-18. The propagation constant for even mode, β_e, is slightly different from the odd mode, β_o. In the beginning, two modes are in-phase as they are excited from one injection waveguide mode. After propagating through certain distance, two super modes are out of phase and the output light is guided to the opposite branch. If L is not long enough, the output is split into two branches with certain ratio. The example Y-reflectors with L=50 μm, 100 μm, 210 μm, respectively, have been simulated by FIMMWave. The structure is with g=2.0 μm, W=10.0 μm, and θ=4.8°. The results are shown in Fig. 2-19. The output power is shifted significantly from the upper branch to the lower branch when L is changed from 50 μm to 210 μm. More results can be found in Fig. 2-20. The insertion loss reduces from 7.4 dB to 1.05 dB when L is changed from 50 μm to 210 μm, and bounds back again if the length increases further.

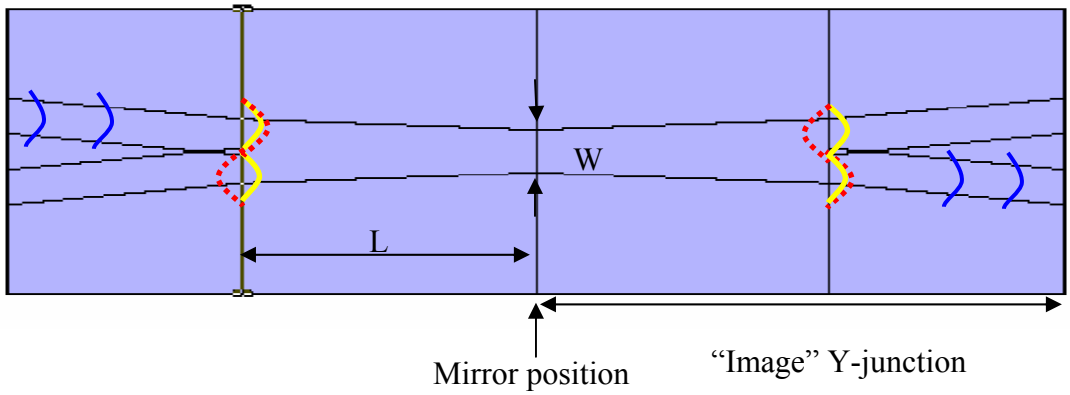

Fig. 2-18. Super modes propagate though Y-junction and its image.

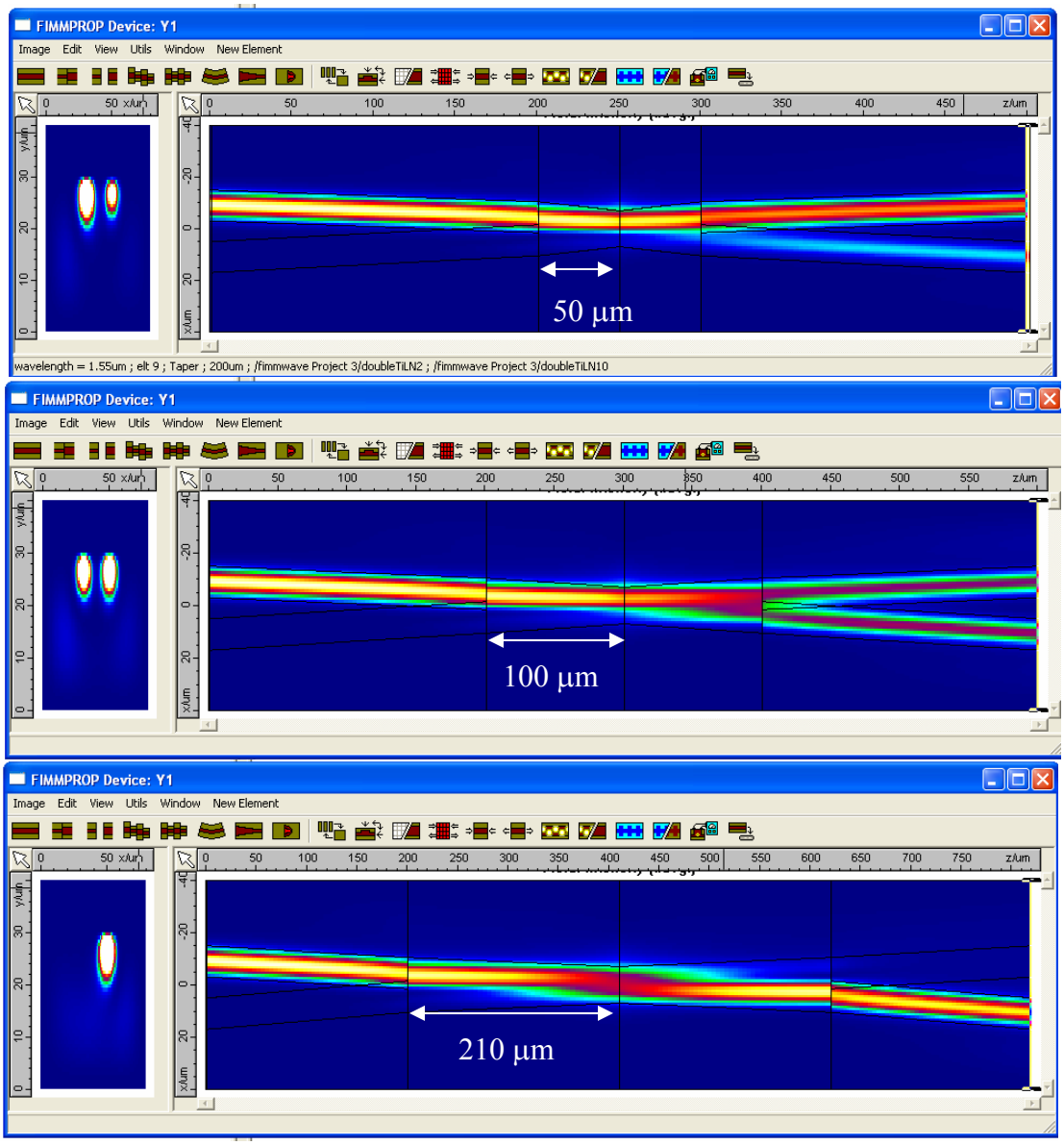

Fig. 2-19. Y-reflector transmission simulation with L=50, 100, 210 µm. The inset to the left is the TM modes at the output branches. Left mode is for the upper branch output and right mode is for the bottom branch output.

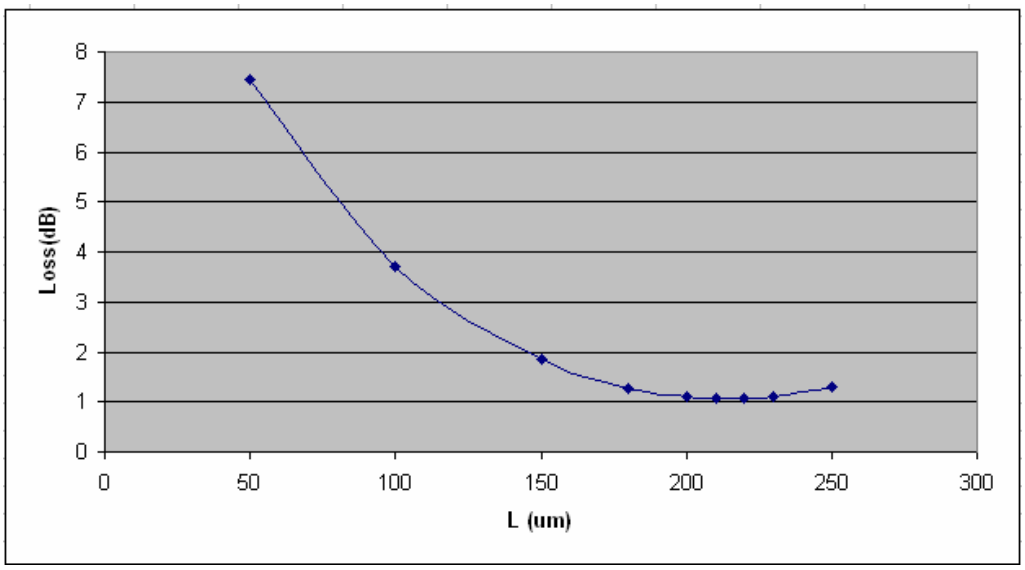

Fig. 2-20. Y-reflector insertion loss varies with taper length.

To minimize the insertion loss of the Y-reflector, test structures with different branch angle θ and converging gap g are made experimentally in Sumitomo company. An example of Y-reflector photo taken from the second generation device is shown in Fig. 2-21. The best insertion loss of 3.5 dB is obtained with θ=5°, g=1.5 μm, L=100 μm, and W=10 μm. However, this value is measured from the stand-alone single Y-reflector and estimated by subtracting the facet reflection loss from the total insertion loss. The value might be over-estimated since we found later on that the roundtrip loss of a loop, which includes two Y-reflectors and two branch waveguides, is only 4.4 dB. The loss of one Y-reflector can not be more than 2 dB.

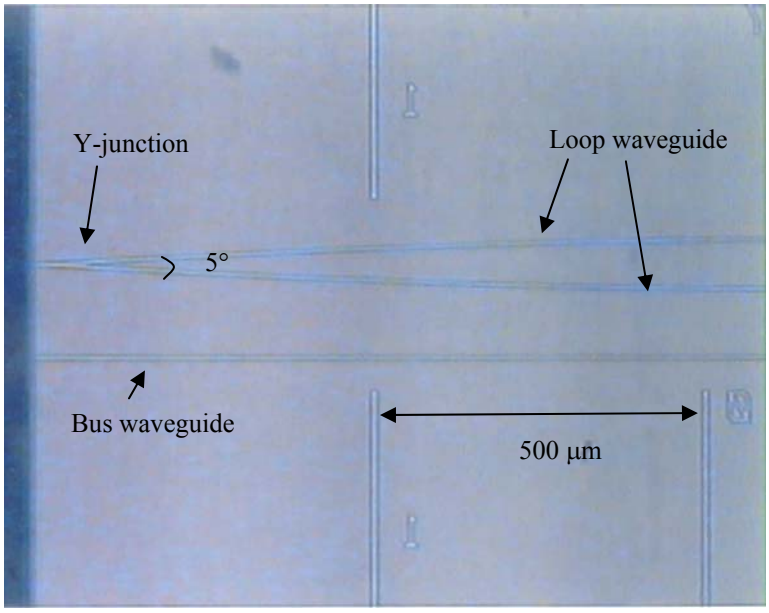

Fig. 2-21. The Y-reflector in the second generation device. Two loop waveguides are merged to the Y-junction with the angle of 5°. The vertical lines are the distance markers.

With the same structure (L=210 μm, g=2.0 μm, W=10.0 μm, and θ=4.8°), we also investigated its sensitivity to the wavelength. Fortunately, the variation of the insertion loss is very small even over 50 nm change of wavelength, as shown in Fig. 2-22. For wavelength at 1520 nm, the insertion loss is 1.14 dB. And it is 1.01 dB at 1570 nm. The variation is less than 0.2 dB. This insensitivity comes from the fact that the insertion loss is only affected by the propagation constant difference between the even mode and odd mode.

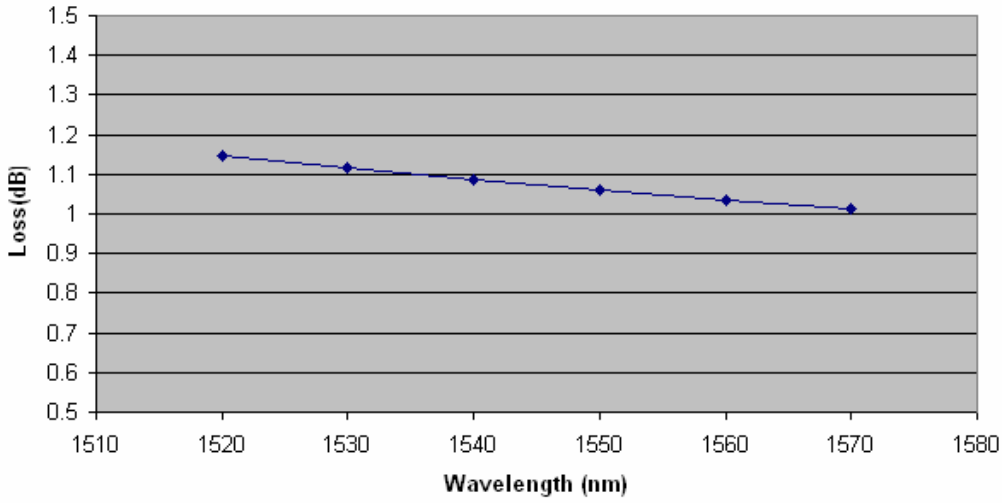

Fig. 2-22. The dispersion characteristics of the Y-reflector.

2.5 The Electrode Design

2.5.1 The Electrode Pattern for The Demo Device

As shown in Fig. 1-18, we need to deploy two RF electrodes to the loop resonator. Electrode 1 is used to fine-tune the loop roundtrip phase (it would be called "phase tuning electrode" hereafter). Electrode 2 is used to fine-tune the δ in the coupling matrix element B (it would be called "coupling tuning electrode" hereafter). The goal is to demonstrate accurate and high speed tunability of the device. The electrode must function effectively for both DC and RF frequency up to several GHz, say, 5 GHz. As a demonstration device, we only adopted very simple lumped electrode. The two electrodes are with same pattern. But in the future, we may want to adopt traveling wave electrode to achieve higher tuning speed or resonant type electrode to obtain higher tuning efficiency. It is necessary to investigate in detail to

the transmission line characteristics of the RF coplanar waveguide (CPW) structure on the lithium niobate substrate.

A detailed view of the electrode is shown in Fig. 2-23. The horizontal hot electrode is overlapped on the top of the Ti-diffused optical waveguide because the substrate is z-cut lithium niobate wafer. A single-sided ground electrode is placed parallel to the hot electrode with a gap of d. The hot electrode is connected to the ground-signal-ground (GSG) type coplanar waveguide signal feeder. The feeder has three sections, including the parallel CPW S_1, S_3, and a tapered section S_2 which is used to eventually convert the large dimensions of S_3 to small dimensions of S_1. The widths of the central strips are 2A for S_3 and 2a for S_1 section respectively. The gap between the central strip and ground plane varies from B-A to b-a. For our demo device, the electrode length is 1.9 mm and the total length of the feeder is 1.341 mm.

The design issues for the hot electrode and the feeder are different as they serve different purposes. For the hot electrode, it has to generate as large as possible electric field in the z direction, so that efficient Electro-optic effect and consequently large tunability of refractive index can be achieved. For the feeder, it has to guide the microwave signal from the source efficiently to the hot electrode so that it requires that the signal reflected from the feeder is as small as possible, i.e., almost all the signal power can be guided to the hot electrode.

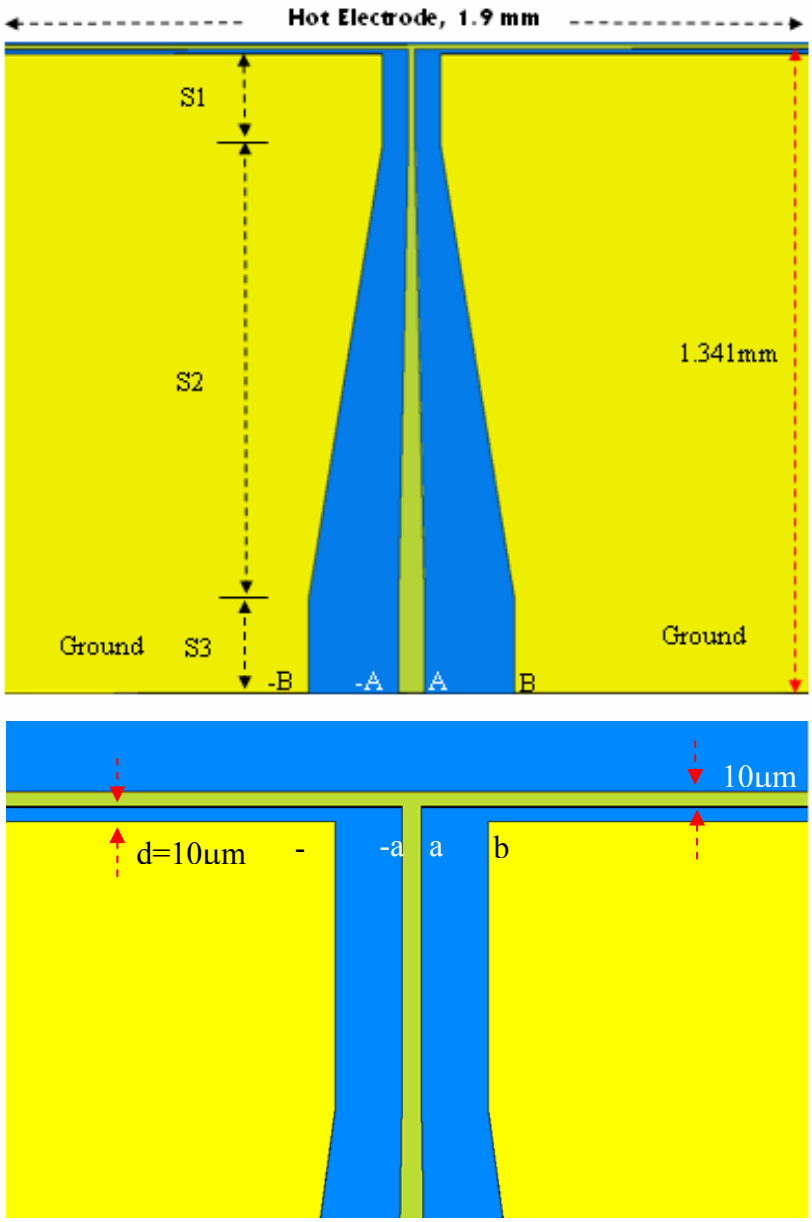

Fig. 2-23. The pattern of the electrode (upper) and the magnified S_1 section (bottom).

The effective electric field E_z underneath the hot electrode is generally defined as

$$E_z = \frac{\gamma V}{d} \tag{2.17}$$

where V is the applied voltage; d is the gap distance between the hot electrode and the ground; γ is the overlap integral between the electrical field and the optical field and is defined by [21-22]

$$\gamma = \frac{d}{V} \frac{\iint E_{opt}^2(x,z) E_z(x,z) dx dz}{\iint E_{opt}^2(x,z) dx dz} \tag{2.18}$$

where $E_{opt}(x, z)$ is the optical field distribution in the xz plane assuming the light propagating along y direction. $E_z(x, z)$ is the electric field distribution. The overlap integral highly depends on the structure parameters of the electrode, such as the gap d, buffer layer thickness, and the hot electrode width and its relative position to the optical waveguide. Although it can be estimated approximately by the conformal mapping method, it is very hard to get a simple analytical expression. [22] The value of γ is generally in the range from 0.3 to 0.55 for z-cut lithium niobate. [21] For the demo device, we have not done the optimization for the hot electrode to obtain a large overlap integral yet. The structure parameters are selected based on the reported results in the literatures. For example, d of 10 μm is commonly used to keep a good overlap integral. [21-23]. γ=0.37 has been extracted from the measured data for our demo device discussed in chapter 3.

2.5.2 CPW Feeder Design

The CPW design of the feeder is a little complicated since the lithium niobate substrate is an anisotropic crystal with different dielectric constant at microwave frequencies for the different axes. In order to reduce the RF reflection, we have to design a CPW feeder with characteristic impedance matched to the RF probe. The computer aided design (CAD) tool, 3D Electro-magnetic field simulation software HFSS (High Frequency Structure Simulation) from Ansoft company is adopted to numerically obtain the microwave parameters such as S-parameter and characteristic impedance.

The shape of the feeder is divided into three sections. Section S_3 is a short parallel CPW used as the touch pad of the RF probe. Section S_1 is also a short parallel CPW with smaller dimension, connected to the middle of the hot electrode. Section S_2 is a tapered part, converging the big dimension of section S_3 to the smaller section S_1.

To understand the discussion of the design, we have to briefly review the basic properties of CPW and try to find the proper dimensions for the CPW with 50 Ω characteristic impedance.

The CPW structure was first proposed by C. P. Wen in 1969 and was extensively studied and applied in microwave and RF devices and circuits. [18-20] A simplified 3D view of the CPW structure is given in Fig. 2-24. Basically, it consists of a center strip line sandwiched between two coplanar ground planes. Both the strip line and the ground planes are metal thin films deposited on the surface of the dielectric substrate. A quasi-TEM mode can propagate along the waveguide without low frequency cut-off.

The RF characteristics of a CPW is determined mainly by the substrate dielectric constant and the geometric parameters a, b.

For simplicity, we first assume the substrate is a single layer with infinite thickness. The relative dielectric constant is ε_r and the range in x direction is from –f to f. The CPW can be analyzed by the conformal mapping transformation. [18-20] The infinite substrate with the relative dielectric constant ε_r in the Z-plane is converted to a square shape cavity filled with the relative dielectric constant ε_r in complex Z_1-plane by

$$\frac{dz_1}{dz} = \frac{A}{\sqrt{(z^2 - a^2)(z^2 - b^2)}} \qquad (2.19)$$

where A is a constant, and the complex $z_1=a_1+j\,b_1$.

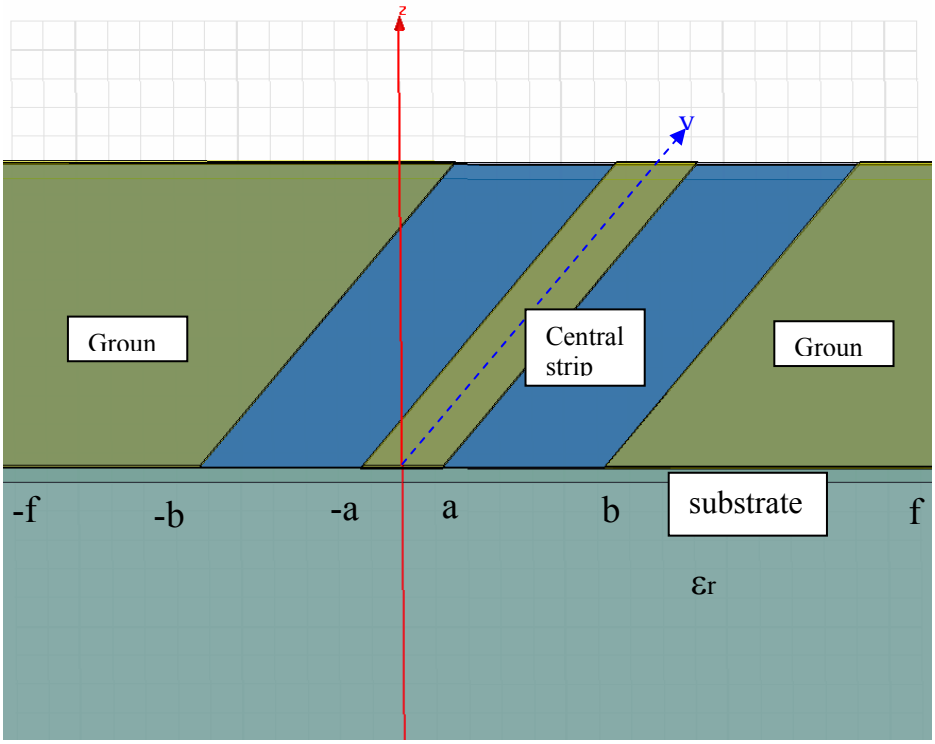

Fig. 2-24. The basic CPW structure on a single layer substrate.

The conformal mapping can be done by performing the integration [18-20]

$$a_1 + jb_1 = \int_0^b \frac{Adz}{\sqrt{(z^2 - a^2)(z^2 - b^2)}} \tag{2.20}$$

where the meanings of a_1 and b_1 are the real and imaginary coordinators in Z_1 plane, as shown in Fig. 2-25. As a result, $\frac{a_1}{b_1} = \frac{K(k)}{K\left(\sqrt{1-k^2}\right)}$, where $k = a/b$ and $K(k)$ is the complete elliptical integral of the first kind, defined as

$$K(k) = \frac{\pi}{2}\sum_{n=0}^{\infty}\left[\frac{(2n-1)!!}{(2n)!!}\right]^2 k^{2n} \tag{2.21}$$

The !! operator means double factorial, i.e., n!!=nx(n-2)x(n-4)x….

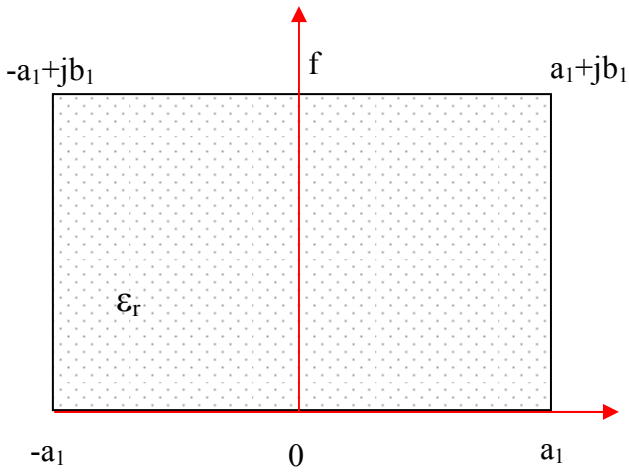

Fig. 2-25. CPW after the conformal transformation.

After the conform mapping, the electric field in the semi-infinite substrate is converted to the uniform electric field between the top and bottom planes of the square

shape cavity shown in Fig. 2-25. So the capacity can be evaluated by the model of the parallel plate capacitance.

The similar conformal mapping method can be applied to the electric field in the semi-infinite air space above the CPW. As these two capacitances are in parallel with each other, the total capacity per unit length is given by [18]

$$C = (\varepsilon_r + 1)\varepsilon_0 \frac{2a_1}{b_1} \tag{2.22}$$

In a zero-order static approximation which simply treats the CPW as a transmission line totally immersed in a dielectric with effective dielectric constant $(\varepsilon_r + 1)/2$, the phase velocity is given by

$$v_{ph} = c / \sqrt{(\varepsilon_r + 1)/2} \tag{2.23}$$

And the characteristic impedance is written as

$$Z_0 = \frac{1}{Cv_{ph}} \tag{2.24}$$

The most important conclusion here is that once the dielectric constant is determined the characteristic impedance is the function of the ratio k=a/b only, which means that we can obtain the same Z_0 by selecting different set of (a, b) which has the same ratio k=a/b.

For a multilayered substrate, the conformal mapping transformation would have a more complex form due to the inclusion of the layer thicknesses. [19-20] In our simulation, the substrate is multilayered since a thin SiO_2 (about 0.55 μm) film is inserted between the metal and the lithium niobate substrate.

Instead of doing the complicated conformal mapping transformation, we have simulated the CPW on lithium niobate substrate with the Ansoft HFSS software. The complete structure used for the simulation is shown in Fig. 2-26. The structure is contained in an air box which serves as the simulation boundary. The boundary condition of the air box surface is radiation condition, meaning all Electro-magnetic waves (EMW) will radiate away from this boundary.

From the bottom to the top, the first layer is the lithium niobate substrate with a thickness of 510 μm. The substrate width is 2 mm and the waveguide length is also 2 mm. For the region under the electrode, the change of the dielectric constant due to Ti-diffusion is very small. A small change of dielectric constant will not affect the RF characteristics, so that it can be neglected in the simulation. The relative dielectric constant matrix is given by

$$\varepsilon_r = \begin{bmatrix} 43 & 0 & 0 \\ 0 & 43 & 0 \\ 0 & 0 & 28 \end{bmatrix} \qquad (2.25)$$

The dielectric loss tangents are approximately set as 0.4 for all three directions. The relative permeability is assumed to equal to 1 and the conductivity is set at 0.

The second layer is a 0.55 μm thick SiO_2 layer on the top of LN substrate and below the metal electrode. It is used to reduce the metal absorption of the light in the waveguide. The relative dielectric constant is 4.0 with a loss tangent of 0. The third layer is the 1 μm thick gold electrode pattern for the CPW structure.

To start the HFSS simulation, the wave port has to be defined for the input and output port of the CPW respectively. HFSS will initialize the wave port with a quasi-

TEM mode in the xz plane, which is the exciting mode for the CPW. However, HFSS can not initialize the input wave port if the substrate is a lossy anisotropic material. So we have to create a very thin (~10 μm) artificial isotropic lithium niobate port material with an average dielectric constant of $\frac{2\varepsilon_x\varepsilon_z}{\varepsilon_x+\varepsilon_z}=33.9$. The CPW will extend to the top of isotropic material. An extra air box is overlapped on the top of the isotropic lithium niobate. The width and height of the ports should be defined large enough. The rule of thumb is that the field of the wave port mode at the edge of the wave port should be much smaller than the center part so that the excitation mode has negligible distortion due to the finite port dimensions.

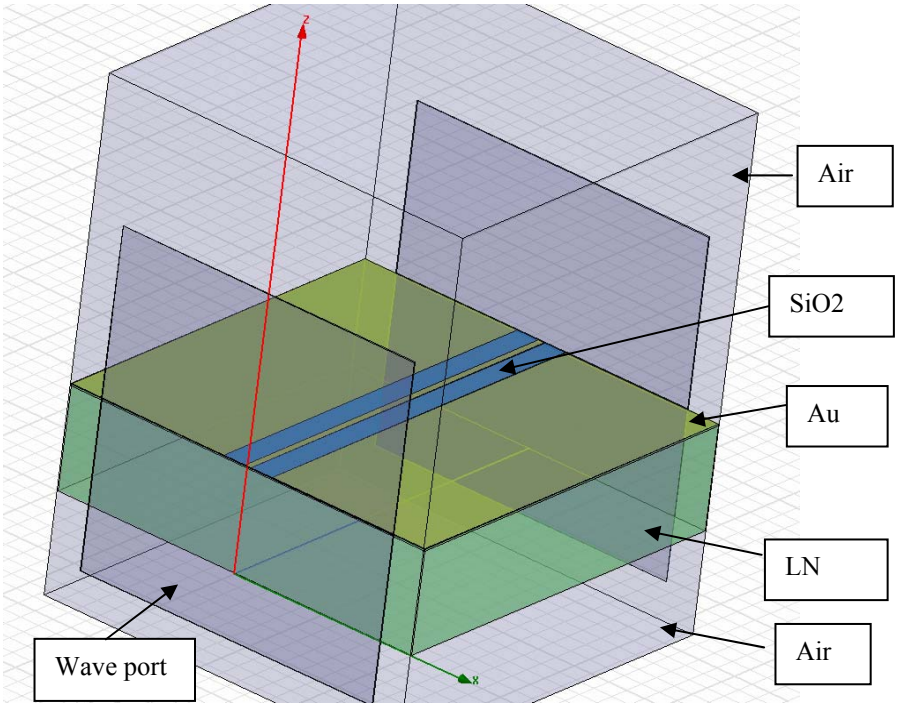

Fig. 2-26. Ansoft HFSS simulation model for CPW on the LN substrate. A thin SiO_2 buffer layer is inserted between the LN layer and the metal layer. The entire structure is contained inside an air box which serves as the simulation boundary. The wave port is defined in the input and output of the CPW respectively.

In order to find a proper geometric structure which has Z_0 of 50 Ω, we can use the parametric sweeping tools of the HFSS. We set the RF frequency as 5 GHz. Sweeping the width of the center strip w(=2a) and the gap g(=b-a), the variation of Z_0 with the different geometric dimensions is shown in Fig. 2-27. From this figure we find out that when g=120 μm and w=35 μm, the magnitude of Z_0 is equal to 50 Ω. The k ratio of this case is $k = a/b = (w/2)/(g + w/2) = 0.1273$. The other interesting point to make is that Z_0 is not sensitive to the variation of w and g. When w is swept from 35 μm to 50 μm and g is swept from 90 μm to 130 μm, Z_0 varies only in the range of 42 Ω to 50 Ω.

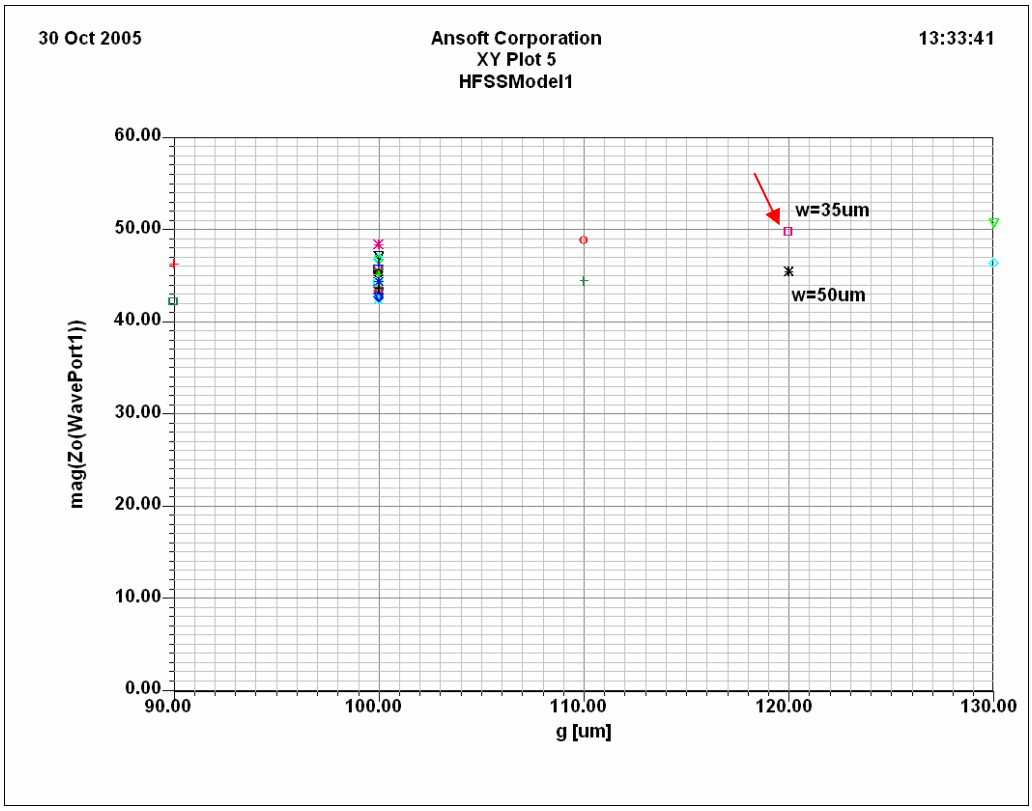

Fig. 2-27. Parametric sweeping to obtain Z_0=50 Ω.

Once we obtain the k=0.1273 for 50 Ω characteristic impedance, the other important RF characteristic of the CPW to be determine is its dispersion, i.e., how Z_0 and S-parameter will vary with frequency. This is done with the frequency sweeping tools of HFSS. We set w=35 μm and g=120 μm and sweep the frequency from 1 GHz to 10 GHz with the step of 1 GHz. The accuracy tolerance of the S-parameter is set as 1%. The results of Z_0 are shown in Fig. 2-28 and S-parameters are in Fig. 2-29.

From Fig. 2-28, we can see that the magnitude of Z_0 varies from 50.40 Ω at 1 GHz to 49.55 Ω at 10 GHz. Z_0=50 Ω is actually located at 2.55 GHz and Z_0=49.80 Ω is found for 5 GHz. At this point, the small difference is ignored because the error is smaller than 1% (the simulation accuracy). Since the substrate has dielectric loss, the Z_0 is a complex-valued number and has a small phase angle varying from 0.1 degree to 0.75 degree.

From Fig. 2-29, we can see that the magnitude of the S_{11} varies from -33.5 dB to -19.5 dB and S_{21} varies from -0.25 dB to -2.6 dB, which implies a small RF power loss (0.25 dB/2 mm=0.125 dB/mm) at low frequency and relatively large (2.6 dB/2 mm=1.3 dB/mm) for high frequency. This loss is low enough for our design to the demo device.

With keeping k=0.1273, we scale down the CPW to w=10 μm and g=34.3 μm and re-run the simulation, trying to see if Z_0 and S-parameters remain unchanged for the same k. It turns out the Z_0 has about 2 Ω increment at 1 GHz and 0.6 Ω increment at 10 GHz, which means the change is smaller than 4% (=2 Ω/50 Ω). And the S-

parameters have less than 1 dB increment. Approximately, we can still use the simple design rule: Z_0 is the function of k only.

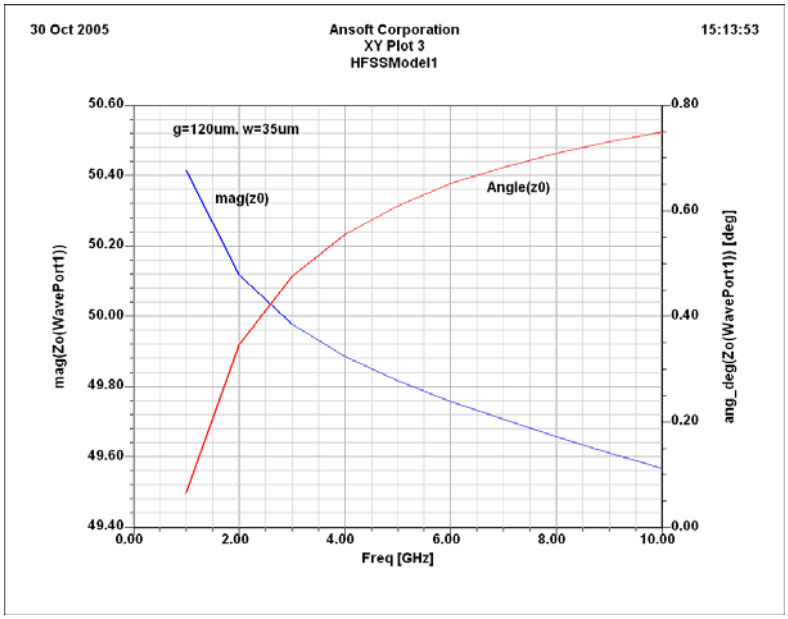

Fig. 2-28. Characteristic impedance variation in frequency domain. The CPW is with with w=35 μm and g=120 μm.

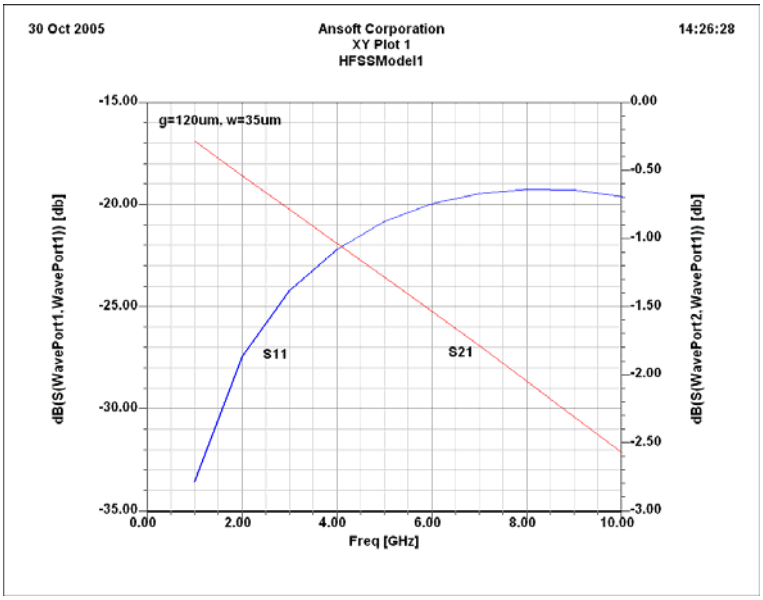

Fig. 2-29. Simulated S_{11} of CPW with w=35 μm and g=120 μm.

Since the characteristic impedance is the function of k only, we propose that the tapered section of the feeder can be designed in this way: use the data set (A, B) for the input port dimension, and the data set (a, b) for the output port which is away from input with distance L in y-direction, then connect A and a, B and b with linear lines, if k=A/B=a/b, any point a(y) and b(y) in between will still have k=a(y)/b(y). The geometric relationship is plotted in Fig. 2-30. The equation for a(y) is written as

$$a(y) = \frac{a-A}{L}y + A = \frac{kb-kB}{L}y + kB = k\left[\frac{b-B}{L}y + B\right] = kb(y) \qquad (2.26)$$

The thinking here is that if we keep $k = \frac{a(y)}{b(y)}$, Z_0 of 50 Ω should be maintained along the tapered section.

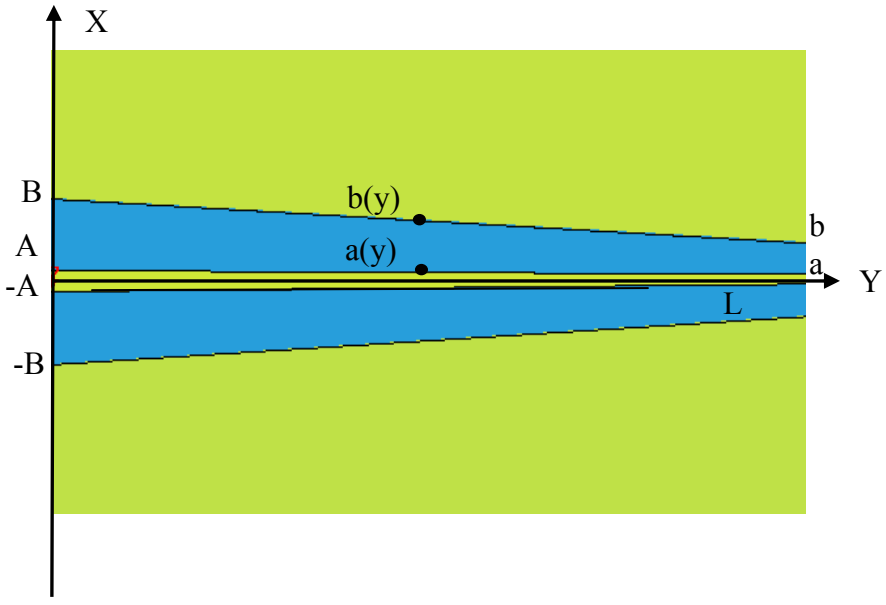

Fig. 2- 30. Tapered section of the feeder.

To verify the design logic of the tapered section, we simulated the structure shown in Fig. 2-30, which has the parameters of k=0.1273, A=17.5 μm, B=137.5 μm, a=5 μm, b=39.3 μm, L=2 mm. The Z_0 results are around 50 Ω as shown in Fig. 2-31.

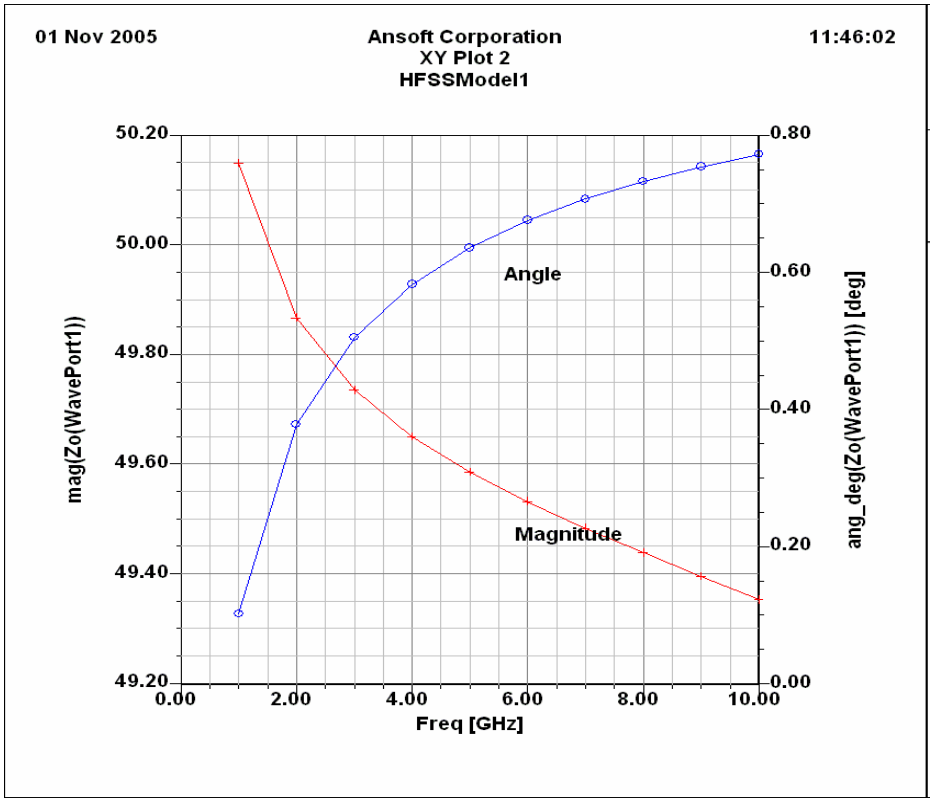

Fig. 2-31. The characteristic impedance of the tapered section.

Finally, we put S_1, S_2, and S_3 sections together to form the entire feeder. The lengths are 200 μm, 940 μm, and 200 μm for these three sections, respectively. The simulation results show that the characteristic impedance is around 50 Ω, which is matched to the RF probe.

2.5.3 S_{11} Measurement to The Electrodes of The Demo Device

Although we have developed a method to design the electrode feeder with characteristic impedance of 50 Ω, the fabricated electrode pattern on the demo device is slightly offset from the designed pattern. The fabrication of an optimized design is complicated further by the tight schedule of the fabrication process in Sumitomo company. Major differences between the designed and the fabricated pattern are from the geometric parameters of the CPW. A=25 μm, B=125 μm, a=5 μm, and b=15 μm are used for the quick design of the demo device, so that ratio k is A/B=0.2 and a/b=0.33 for the S_3 and S_1 section respectively. For k=0.2, Z_0 of CPW is about 43 Ω. For k=0.33, the Z_0 of CPW is about 39 Ω.

A photo of the loop resonator device with the electrodes is shown in Fig.2-32 and the enlarged views of the middle part and end part of the electrode are shown in Fig. 2-33 and Fig. 2-34, respectively. Fortunately, the offset did not affect much the performance of the electrode. The simulated magnitude of the Z_0 is shown in Fig. 2-35. It is around 44 Ω. Most of the power still can be transmitted to the electrode.

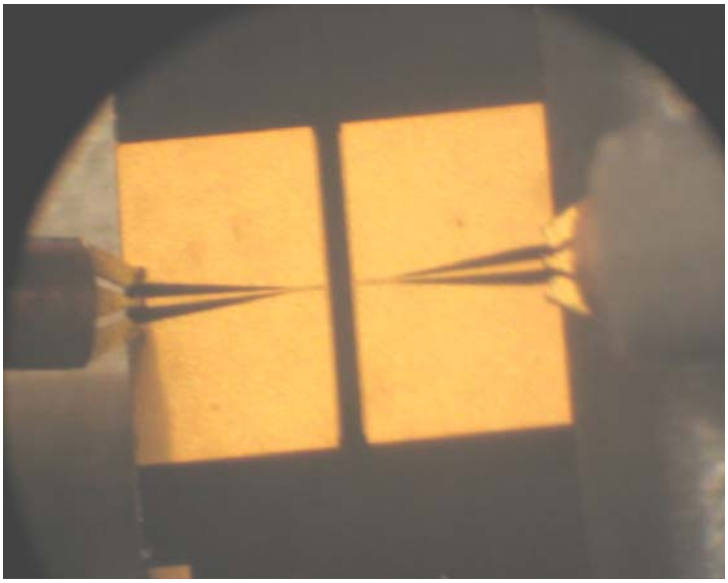

Fig. 2-32. Appearance of the testing electrodes with RF probe touched on the feeder.

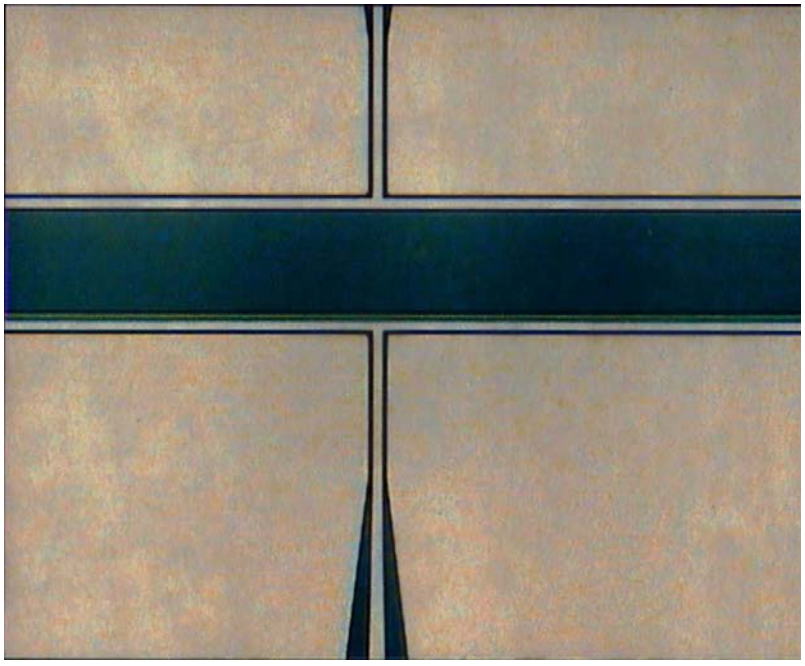

Fig. 2-33. Central part of phase tuning electrode (upper) and coupling tuning electrode (bottom).

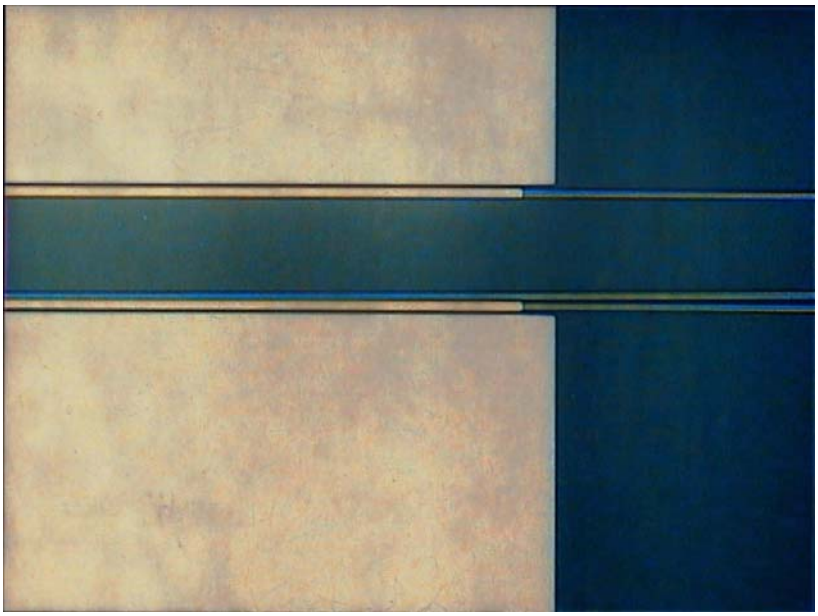

Fig. 2- 34. End part of phase tuning electrode (upper) and coupling tuning electrode (bottom).

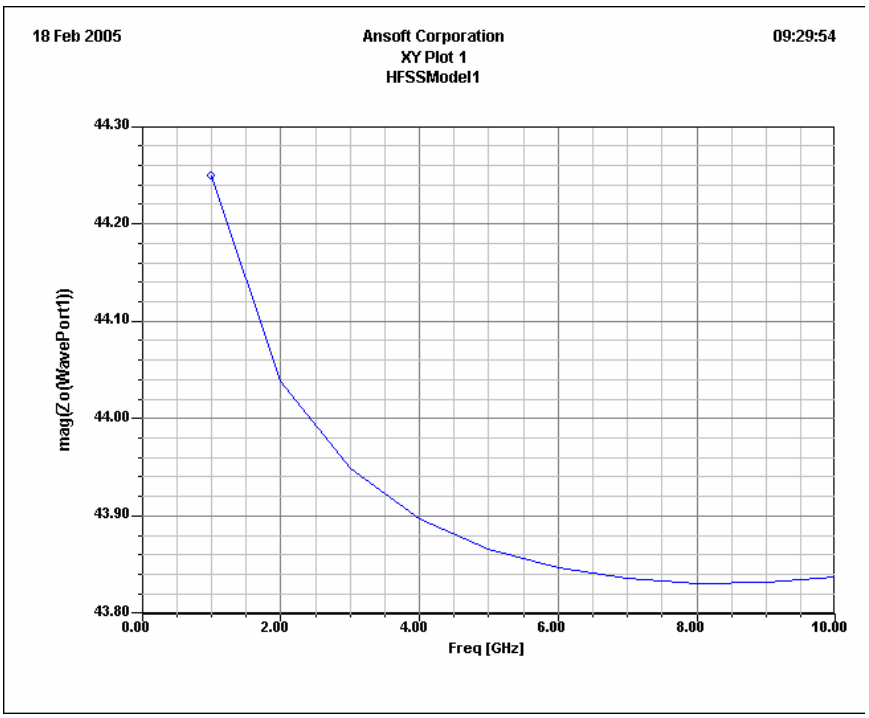

Fig. 2-35. Simulated input characteristic impedance for the testing electrode.

To verify the design, we measured S_{11} parameter of the fabricated electrode on the demo device with RF network analyzer HP 8703 and RF probe with a tip distance of 200 μm. As shown in Fig. 2-36, the measured results are compared with the simulated results. The measured S_{11} as the function of frequency has more complex structure than the simulated S_{11}. For frequency f<7 GHz, the differences of S_{11} are within 1.5 dB. Two dips are found around 1 GHz and 3.5 GHz. For frequency f close to 10 GHz, the simulated and measured S_{11} differ by 5 dB. Except for the fabrication error, a possible explanation of the difference is that the quality of the fabricated metal electrode is not as good as what we assumed in the simulation, so that the radiation loss or transmission loss is larger at high frequency.

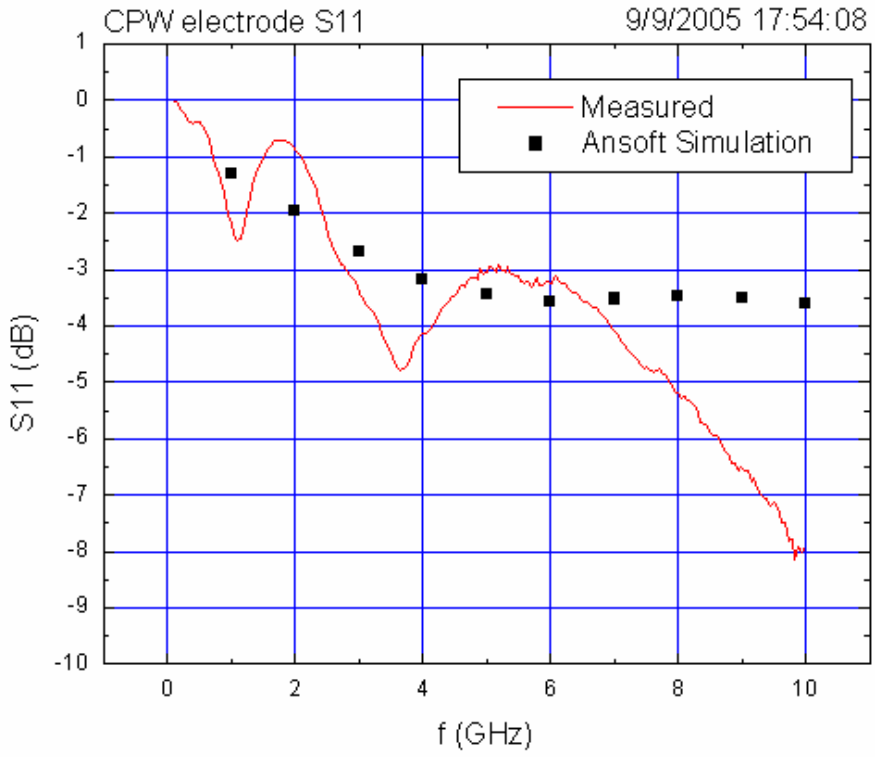

Fig. 2-36. Comparison of the measured and simulated S_{11} data.

2.6 The Tunability of The Lithium Niobate Loop

After the analysis of the electrode design, we analyzed tunability of the lithium niobate loop (LN-loop) based all pass filter. A good tunability is able to obtain with the device working with the TM mode.

The roundtrip phase variation with the applied voltage is given by

$$\begin{aligned}\phi &= \frac{2\pi}{\lambda}\left[n_e L + \Delta n_e l_e\right] \\ &= \frac{2\pi}{\lambda}\left[n_e L - \frac{1}{2} n_e^3 r_{33} E_z l_e\right] \\ &= \frac{2\pi}{\lambda}\left[n_e L - \frac{1}{2} n_e^3 r_{33} l_e \frac{\gamma V}{d}\right]\end{aligned} \qquad (2.27)$$

where L is the roundtrip length of the loop. l_e is the length of the electrode; And the electric field $E_z = \frac{\gamma V}{d}$ is used.

To estimate the frequency tunability, we assume f_0 is the resonant frequency at V=0, i. e.,

$$\phi_0 = f_0 \frac{2\pi}{c} n_e L = M_0 2\pi \qquad (2.28)$$

where c is the light speed in the vacuum and M_0 is an integer number.

When the bias voltage V is applied to the electrode, the resonant frequency is shifted to $f_0+\Delta f$. We have

$$\phi_1 = \left(f_0 + \Delta f\right)\frac{2\pi}{c}\left[n_e L + \Delta n_e l_e\right] = M_1 2\pi \qquad (2.29)$$

For the frequency tuning range smaller than the free spectrum range, we have $\phi_0=\phi_1$ and $M_0=M_1$. The frequency shifting can be given by

$$\Delta f = -f_0 \frac{\Delta n_e l_e}{n_e L + \Delta n_e l_e} \approx -f_0 \frac{\Delta n_e l_e}{n_e L} = f_0 \frac{1}{2} n_e^3 r_{33} \frac{\gamma V}{d} \frac{l_e}{n_e L} \qquad (2.30)$$

where the assumption $\Delta n_e l_e << n_e L$ is applied for equation (2.30). From equation (2.30), we can see that the frequency tuning is approximately affected linearly by the electrode length l_e and the applied voltage. It is convenient to use the normalized frequency tunability $\Delta f /(V l_e)$ as the figure of merit to describe the loop tunability, which is the frequency tuning range of 1 V bias for the electrode of unit length, say, 1 cm. We will use the unit of MHz/(V·cm) for the figure of merit.

The other two important parameters for the tunability are the gap d and the effective coefficient γ. In Fig. 2-37, the simulated tunability as the function of γ has been plotted for d=5 and 10 μm, respectively. n_eL= 67410.3 μm is used for the plots.

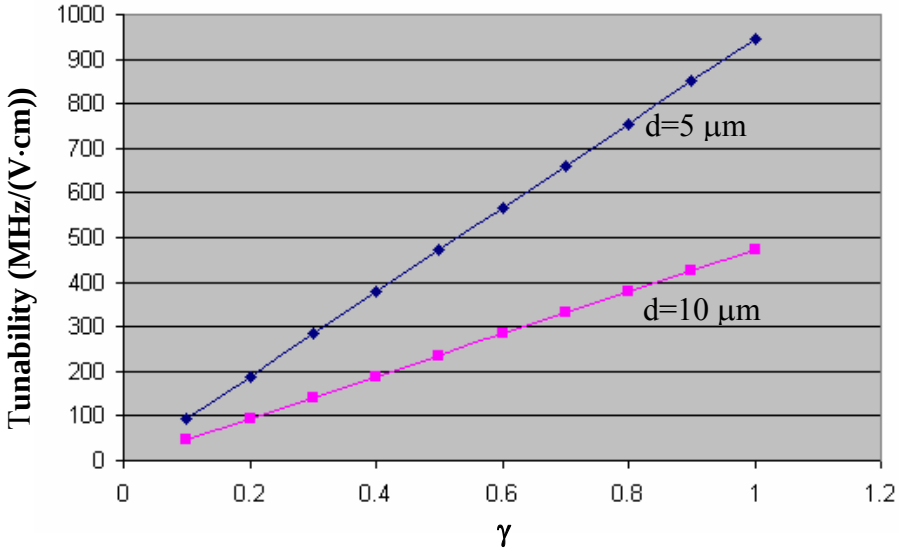

Fig. 2-37. Estimation to the normalized frequency tunability of the APF.

We have measured the tunability of 175 MHz/(V·cm) for our demo device with γ of 0.37. Assuming the electrode length can be extended to 1.5 cm, it needs 38 V bias

to tune the resonant frequency over 10 GHz. If we can improve γ to 0.55, [21] the tunability is expected to be 260 MHz/(V·cm). For the electrode length of 1.5 cm, it needs 25 V bias to achieve 10 GHz frequency tuning range.

2.7 Summary

In this chapter, the TE and TM mode pattern in the Ti:LN waveguide have been simulated. According to the simulation, the TE mode size is larger than the TM mode due to the smaller change of the ordinary index caused by the Ti diffusion. For the coupling section, the power coupling ratio has been simulated for the TM mode. For the coupling gap around 4 μm, the coupling ratio is about 93.5%, close to the measured result. The simulation shows the Y-junction has a low loss of 1.05 dB. The loss is insensitive to the input wavelength. The design method for the CPW feeder electrode to reduce the RF loss has been discussed. A normalized tunability of 175 MHz/(V·cm) is realized for the demo device, which has the effective length of the electrode of 1.9 mm and electrode gap of 10 μm. 260 MHz/(V·cm) frequency tunability has been projected under reasonable assumptions.

Reference

[1] Eddie. L. Wooten, "Modelling of Optical Guided Wave Devices in Lithium niobate Using Test Structures for Process Characterization", PhD dissertation, Dept. of Electrical and Computer Engineering, University of California, San Diego, 1991.

[2] K. K. Wong, "Properties of Lithium Niobate", INSPEC, The Institution of Electrical Engineers, ISBN 0 85296 799 3, UK, 2002.

[3] A. A. Ballman, " Growth of piezoelectric and ferroelectric materials by the Czochralski technique", Journal of the American Ceramic Society, Vol. 48, p. 112, 1965.

[4] K. Nassau, H. J. Levinstein, and G. M. Loiacono, "Ferroelectric lithium niobate. 1. Growth, domain structure, dislocations and etching", Journal of Physical Chemistry of Solids, Vol. 27, pp 983-988, 1966.

[5] A. Yariv, "Optical Electronics", New York: CBS College Publishing, 3rd ed., 1985.

[6] J. T. Milek and M. Neuberger, "Linear Electrooptic Modulator Materials", Vol.8 of Handbook of Electronic Materials, pp92-124, IFI/Plenum, 1972.

[7] J. L. Jackel, C. E. Rice, J. J. Veselka, "Proton exchange for high-index waveguides in LiNbO3", Appl. Phys. Lett., Vol. 41, No. 7, pp607-608, 1982.

[8] R. V. Schmidt, and I. P. Kaminow, "Metal-diffused optical waveguides in LiNbO3", Appl. Phys. Lett., Vol.25, pp.458-460, 1974.

[9] H. S. Hinton, " Photonic Switching Using Directional Couplers", IEEE Communications Magazine, Vol. 25, No. 5, pp16-26, 1987.

[10] H. Yajima, "Dielectric thin-film optical branching waveguide", Appl. Phys. Lett. Vol. 12, pp647-649, 1973.

[11] W. K. Burns, and A. F. Milton, "Mode conversion in planar-dielectric separating waveguides", IEEE J. Quantum Electron., Vol. 11, pp32-39, 1975.

[12] T. R. Ranganath, and S. Wang, "Ti-diffused LiNbO3 branching waveguide modulators: performance and design," IEEE J. Quantum Electron., Vol. 13, pp 290-295, 1977.

[13] H. Yajima, "Coupled mode analysis of dielectric planar branching waveguides", IEEE J. Quantum Electron., Vol. 14, pp 749-755, 1978.

[14] H. Sasaki, and I. Anderson, "Theoretical and experimental studies on active Y junction in optical waveguides," IEEE J. Quantum Electron., vol. 14, pp 883-892, 1978.

[15] W. K. Burns, and A. F. Milton, "An active analysis solution for mode coupling in optical waveguide branches," IEEE J. Quantum Electron., Vol. 16, pp 446-454, 1980.

[16] M. Izutsu, Y. Nakai, and T. Sueta, "Operation mechanism of the single-mode optical-waveguide Y junction", Optics Lett., Vol. 7, pp 136-138, 1982.

[17] T. Nakazawa, S. Taniguchi, and M. Seino, "Ti:LiNbO3 Acousto-optic Tunable Filter (AOTF)", Fujitsu Sci. Tech. J., 35, 1, pp. 107-112, Jul., 1999.

[18] C. P. Wen, "Coplanar Waveguide: A Surface Strip Transmission Line Suitable for Nonreciprocal Gyromagnetic Device Applications", IEEE Trans. Microwave Theory and Tech., vol. MTT-17, No. 12, pp1087-1090, 1969.

[19] S. Gevorgian, L. J. Peter Linner, and E. L. Kollberg, "CAD Models for Shielded Multilayered CPW", IEEE IEEE Trans. Microwave Theory and Tech., Vol. 43, No. 4, pp 772-778, 1995.

[20] E. Carlsson, and S. Gevorgian, "Conformal Mapping of the Field and Charge Distributions in Multilayered Substrate CPW's", IEEE Trans. Microwave Theory and Tech., Vol. 47, No.8, pp1544-1552, 1999.

[21] X. Zhang, and T. Miyoshi, "Optimum Design of Coplanar Waveguide for $LiNbO_3$ Optical Modulator", IEEE Trans. Microwave Theory and Tech., Vol. 43, No. 3, pp 523-528,1995.

[22] C. M. Kim, and R. V. Ramaswamy, "Overlap Integral Factors in Integrated Optic Modulators and Switches", J. Lightwave Technol., Vol. 7, pp1063-1070, Jul. 1989.

[23] E. L. Wooten, K. M. Kissa, A. Yi-yan, E. J. Murphy, D. A. Lafaw, P. F. Hallemeier, D. Maack, D. v. Attanasio, D. J. Fritz, G. J. McBrien, and D. E. bossi, "A Review of Lithium Niobate Modulators for Fiber-Optic Communications Systems", IEEE j. Sel. Top. Quantum Electon., Vol. 6, No. 1, pp69-82, Jan. 2000.

Chapter 3. Measurement and Analysis of Lithium Niobate Loop Devices

In this chapter, the optical transmission responses of two generations of tunable lithium niobate loop (LN-loop) devices are presented. The DC and AC tunability are demonstrated with the second generation device. Possible extensions of the technique to other devices are also briefly discussed.

3.1 Two Generations of The Demo Devices for LN Loop Resonator

As mentioned in the previous chapter, we have completed two generations of the testing devices in collaboration with Sumitomo Osaka Cement Company. The first generation (1G) devices, which have only optical waveguide structures but without the tuning electrodes, are used to study the optical transmission characteristics of the loop resonator. The second generation devices (2G) are mainly used to study the frequency tunability. There are two tuning electrodes applied for the 2G devices, one for loop roundtrip phase tuning and one for the coupler splitting ratio tuning.

The pictures of the 1G and 2G devices are shown in Fig. 3-1 and Fig. 3-2, respectively. The optical waveguide structures for these two generation devices are almost identical except the gap distance of the coupler between the bus waveguide and the loop waveguide, which is about 4.0 μm for the 1G devices and 6.0 μm for the 2G devices. The size of the wafer, limited by the cutting facility, is 14 mm x 1.8 mm for 1G device and 14 mm x 2.8 mm for the 2G device. At each end of the wafer, a small

piece of lithium niobate is glued on the top of the waveguide to support the mirror coating. The 2G device looks darker because of the color of the SiO_2 buffer layer on the lithium niobate surface.

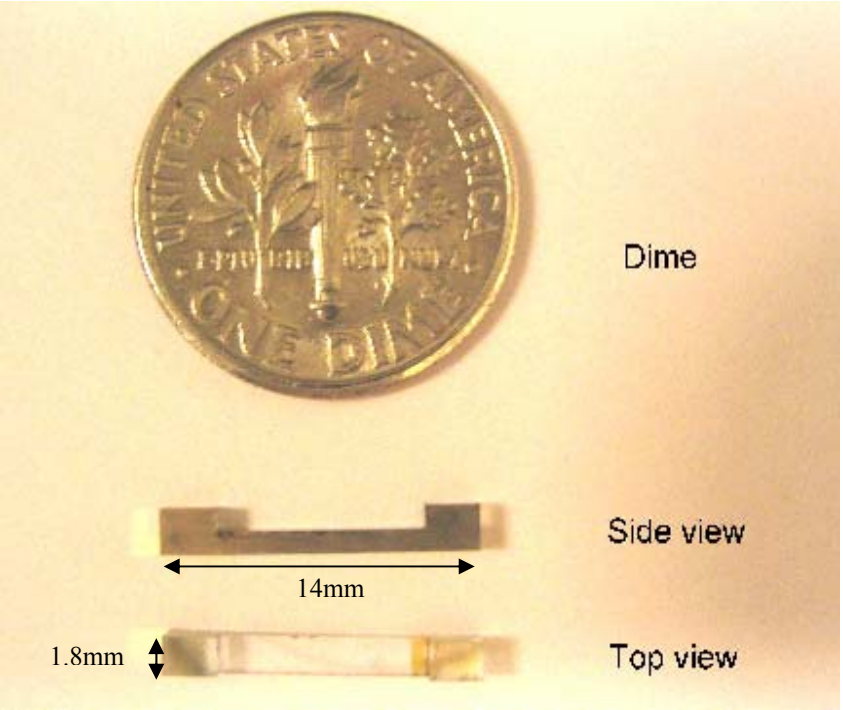

Fig. 3-1. The side and top view of the first generation device.

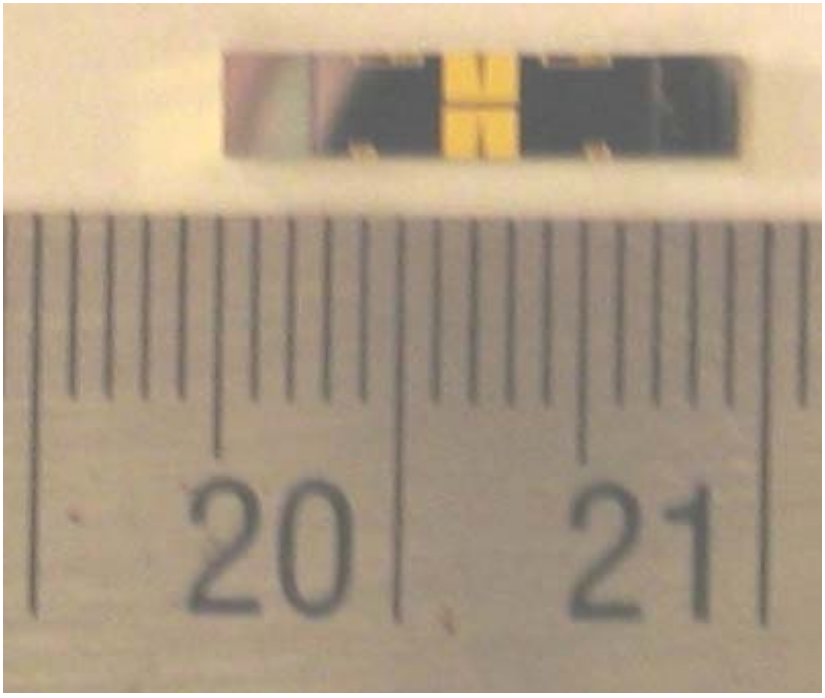

Fig. 3-2. The top view of the second generation device.

3.2 Transmission and DC Tunability Measurement

Measurements of the optical transmission function have been done both at UCSD and at Sumitomo. The results are consistent with each other. However, the data from Sumitomo are done with finer wavelength resolution because they have a better Lightwave Measurement System, Agilent 8164A, which has wavelength resolution of 0.1 pm. We only have a tunable laser with wavelength resolution of 8 pm in UCSD. In the discussion below, some of measured data from Sumitomo are used.

The measurement setup is shown in Fig. 3-3. The Lightwave Measurement System has an output wavelength ranged from 1500 nm to 1640 nm. The polarization

of the output light is controlled by the polarization controller (P.C.). The output of the loop resonator is coupled back to Agilent 8164A. As the polarization maintaining fiber is used for the setup, the polarization is expected stable during the measurement. The polarization state of the light incident on the waveguide is tuned to TM mode by the polarization controller. A DC voltage source is used to apply the tuning voltage to the phase tuning electrode or the coupling tuning electrode for the 2G device.

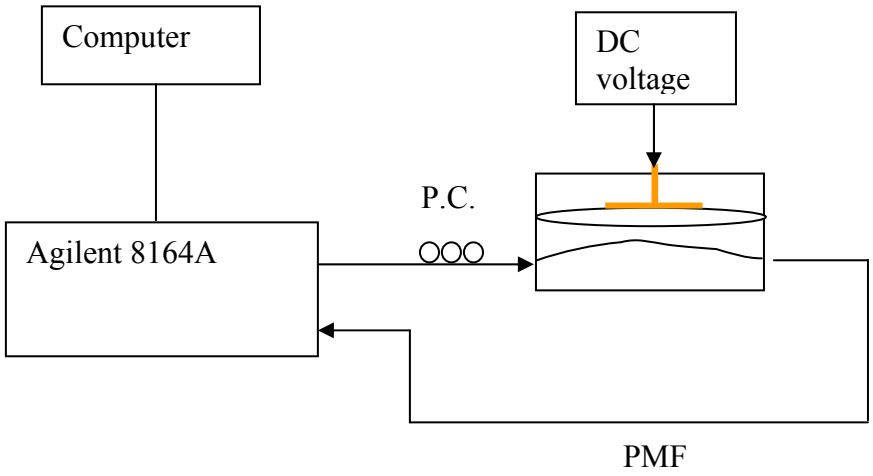

Fig. 3-3. Transmission measurement setup. PMF: polarization maintaining fiber. P.C.: polarization controller.

The transmission measurements at different wavelengths, ranging from 1.5545 μm to 1.5550 μm, are carried out in three devices with coupling gaps of 4.2 μm, 4.1 μm, and 4.0 μm. Fig. 3-4 (a), (b), and (c) show the normalized fiber-to-fiber transmissions and the theoretical results obtained by curve fitting the experimental results to the model mentioned in chapter 1. The fitting results have been summarized

in Table 3-1. It can be seen that the model can describe the experiment results very well.

One puzzle found from the measured results is that the sample 3-4, which is with narrower gap of 4.0 μm, shows the results inconsistent with the results of sample 3-2 and 3-3. It has smaller power coupling ratio instead of a larger value. And its insertion loss is also larger than the other two samples. We think that the inconsistency is caused by fabrication error.

Overall, the 1G devices have the power coupling ratio ranged from 91.5% to 93.5% and the roundtrip loop loss from 3.5 dB to 4.85 dB. If we assume the waveguide propagation loss is about 0.5 dB/cm, the loss of each Y-Reflector is between 1 dB to 1.7 dB. The coupling ratios are too large to obtain a good rejection level, which is defined as the ratio of the peak to minimum power of the transmission. Taking sample 3-2 as an example, if we could change the coupling ratio from 92.5% to 56.11%, the rejection level would be over 30 dB, as shown in Fig. 3-5.

According to the measured results of the 1G devices, we suggested a larger coupling gap to 6 μm to Sumitomo company when they fabricate the 2G devices. Currently fabricated 2G device has gap of about 6 μm and coupling ratio is reduced to 80% according to the curve fitting result.

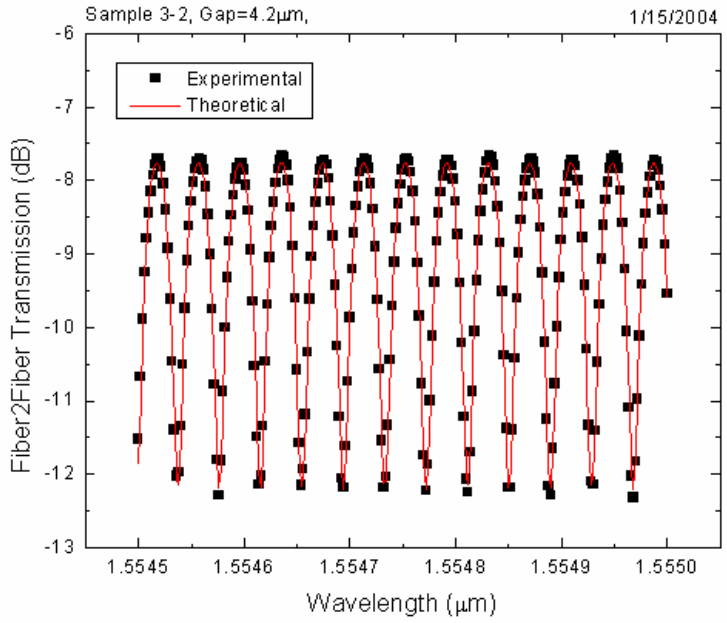

(a)

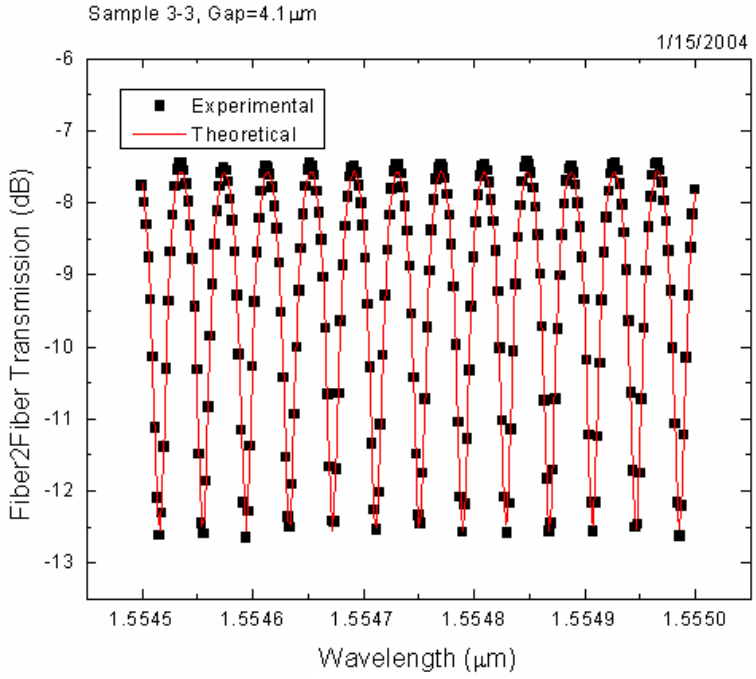

(b)

Fig. 3-4. Normalized fiber to fiber transmission measurements to the first generation devices with coupling gaps of (a) 4.2 μm, (b) 4.1 μm, and (c) 4.0 μm. (To be continued in the next page)

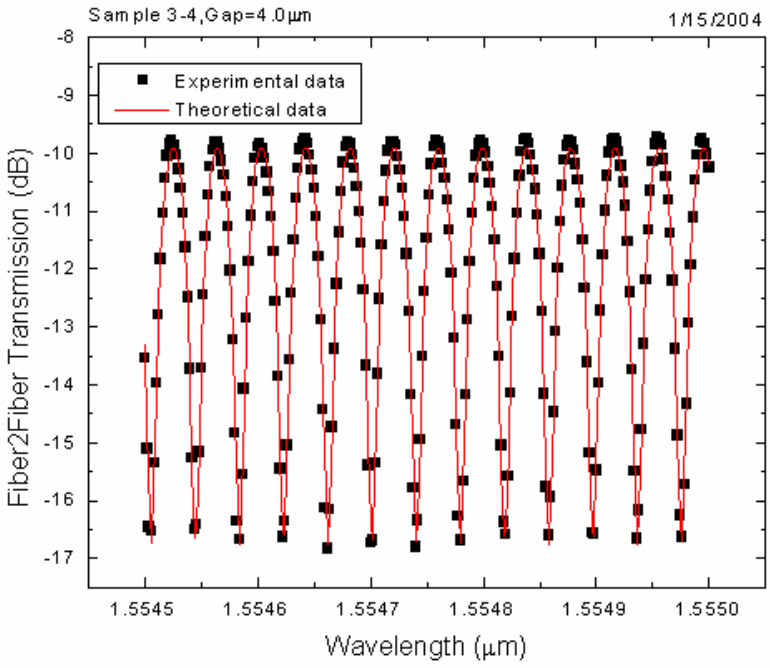

(c)

Fig. 3-4 (continue). Normalized fiber to fiber transmission measurements to the first generation devices with coupling gaps of (a) 4.2 μm, (b) 4.1 μm, and (c) 4.0 μm.

Table 3-1. The curve fitting results to the normalized fiber to fiber transmission results of the first generation devices with coupling gaps of 4.2 μm, 4.1 μm, and 4.0 μm, respectively.

Sample #	Gap (μm)	K (%)	α (dB)	Γ (dB)	Rejection (dB)
3-2	4.2	92.5	-3.5	-5.7	4.44
3-3	4.1	93.4	-4.24	-5.08	5.15
3-4	4.0	91.5	-4.85	-7.28	6.86

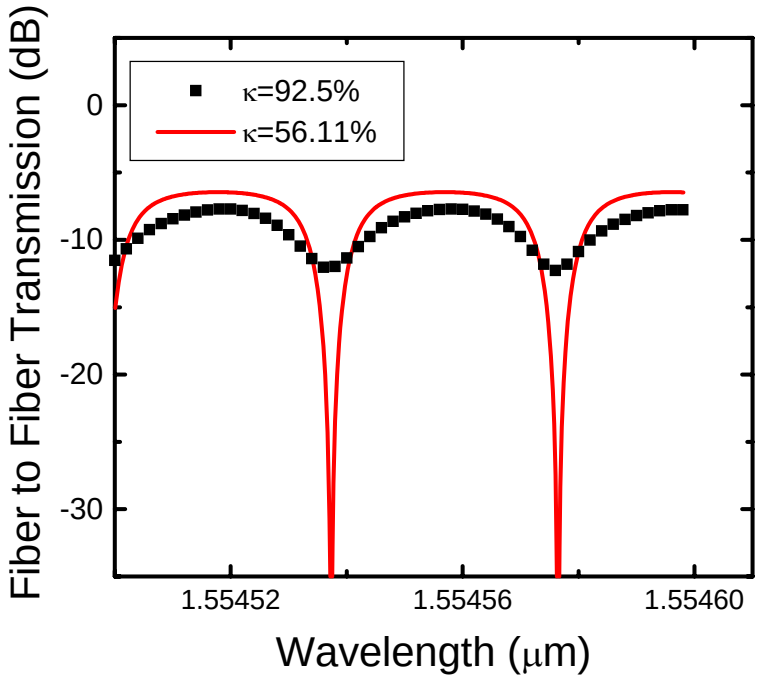

Fig. 3-5. Comparison of the rejection level for power coupling ratio of 92.5% and 56.11% respectively.

For the 2G device with electrodes, the transmission measurements have been done when different bias voltages are applied to either phase- or coupling-tuning electrodes. The transmission curves with phase tuning voltage of 0 and 15 V are shown in Fig. 3-6. The input optical power is -7 dBm. The resonant wavelength is blue-shifted 0.004 nm (0.50 GHz in frequency shift) with a 15 V bias. This means the tunibility is about 33.3 MHz/V for the 1.9mm long electrode or 33.3/0.19=175 MHz/(V·cm). The device works for the TM polarization. The tunability comes from the electro-optic effect of the extraordinary refractive index, n_e. The curve fitting result

shows the loop optical length n_eL is equal to 61740.3 μm, the power coupling ratio is 80%, roundtrip loss α is 4.43 dB, and extra loss Γ is 2.6 dB.

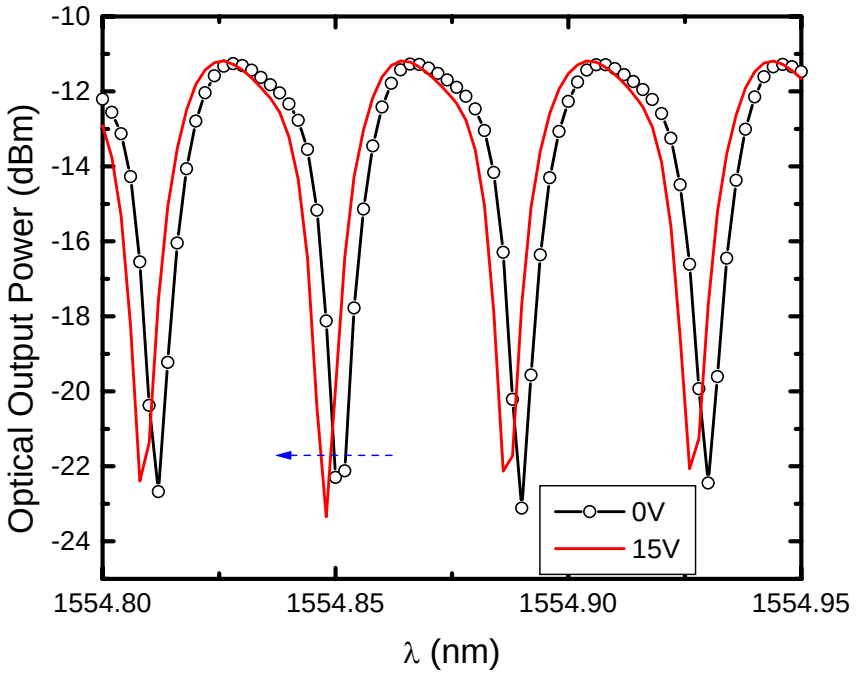

Fig. 3-6. DC phase tunability of the second generation device.

In order to estimate the variation of the refractive index, we note that the resonant phase condition

$$\phi = 2\pi \frac{n_e L}{\lambda} = 2\pi \frac{n_e L + \Delta n_e l_e}{\lambda + \Delta\lambda} \qquad (3.1)$$

where L is the roundtrip length of the loop, le is the effective length of the electrode, λ is the resonant wavelength, and Δλ is the wavelength shifting. The index variation is written as

$$\Delta n_e = \frac{\Delta\lambda}{\lambda}\frac{n_e L}{l_e} \qquad (3.2)$$

As mentioned in chapter 2, the index variation is related to the electric field by

$$\Delta n_e = -\frac{1}{2} n_e^3 r_{33} E_z \qquad (3.3)$$

The effective electric field is estimated by

$$E_z = -2\Delta n_e / (n_e^3 r_{33}) \qquad (3.4)$$

The parameters and the estimated E_z for the tunability shown in Fig.3-6 with 15 V DC tuning voltage are summarized in Table 3-2. The result looks reasonable. The total change in optical roundtrip phase is about 36.8°, which is estimated from

$$\Delta\phi = \frac{2\pi\Delta n_e l_e}{\lambda}. \qquad (3.5)$$

Table 3-2. The parameters and estimation results for the DC phase tuning.

n_e	L (μm)	l_e(μm)	λ(nm)	Δλ(nm)	Δn_e	E_z (V/μm)
2.1383	28873.4	1900	1554.85	-0.004	0.0000836	0.55

From the estimated Ez, we can estimate the overlap integral γ used in the equation (2.17). Since the gap between the hot electrode and the ground plane is 10 μm, the bias is 15 V, and Ez=0.55 V/μm, we have $\gamma = E_z / (V/d) = 0.55/(15/10) = 0.37$.

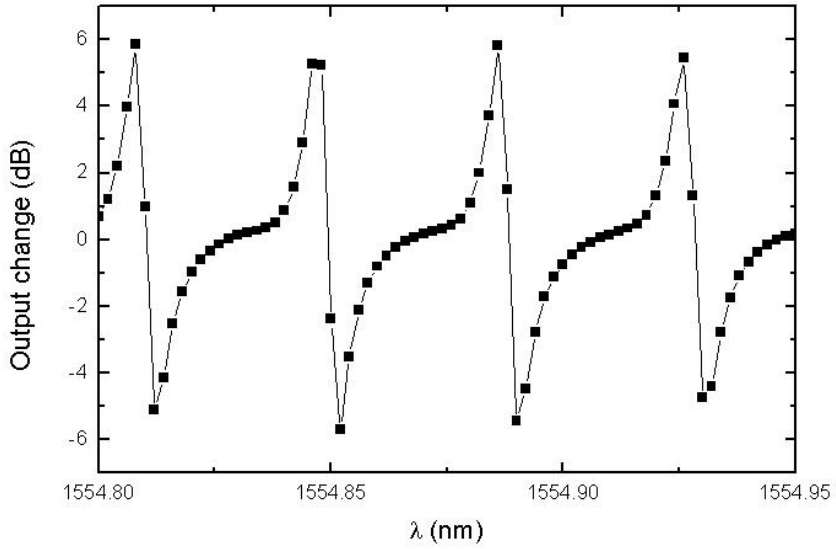

Fig. 3-7. Output power changes between 0 V and 15 V bias.

It is also interesting to examine the optical output power change at different wavelengths when the bias is changed from 0 V to 15 V. The output power change is easily obtained by subtracting the output power curve at 0 V from the output power curve at 15 V. The result in Fig.3-7 shows the maximum change is 6 dB. This helps us to choose the proper wavelength to do high efficiency modulation when we use the loop device as a modulator.

Similar DC tunability measurement has been done by applying the bias to the coupling tuning electrode, as shown in Fig. 3-8. It can be seen that it behaves similarly to the phase tuning electrode, but it has half the tunability, meaning it has 0.004 nm resonant wavelength blue shift at 30 V bias. This 50% reduction in phase tuning efficiency is because the coupling tuning electrode is on the top of the bus waveguide but not on the loop waveguide. The applied tuning electric field has a smaller overlap with the optical mode of the loop waveguide. As the consequence, the tuning

efficiency is lower than the phase tuning electrode which is directly on the top of loop waveguide.

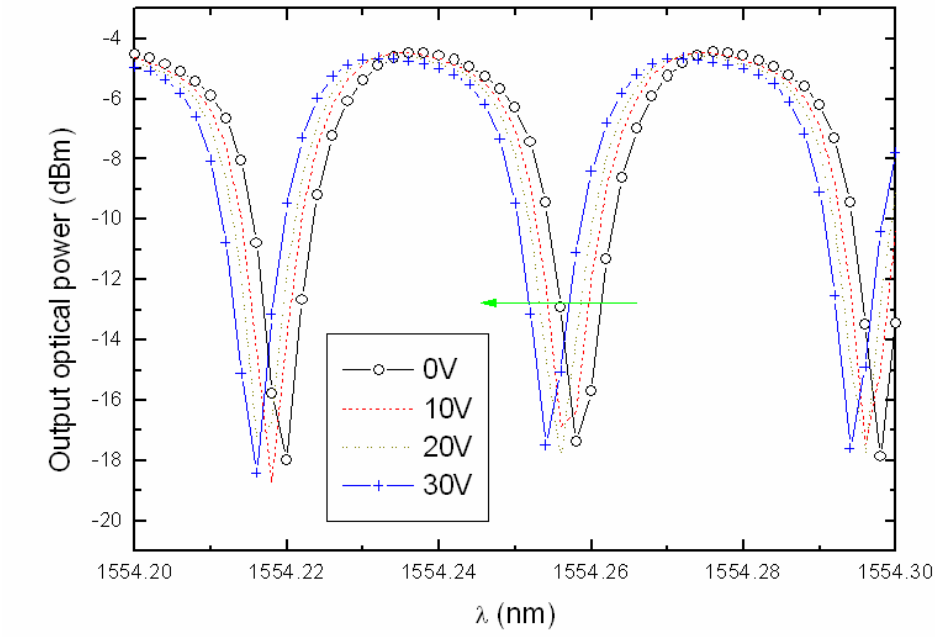

Fig. 3-8. DC tunability by applying voltage to coupling tuning electrode.

However, the coupling ratio does not change enough to affect significantly the rejection level because the index variation is too small. As it is described in chapter 2, the coupling ratio is affected by the propagation constant mismatch according to $\delta = (\beta_1 - \beta_2)/2 = \frac{\pi}{\lambda}(n_1 - n_2) = \frac{\pi}{\lambda}\Delta n$. If we estimate Δn_e is 8.36×10^{-5} for 30 V bias, then δ is about 1.69×10^{-4} μm^{-1}.

In order to evaluate how big this mismatch will affect the coupling coefficient, we've done a simple simulation estimation to a coupler that has two parallel Ti:LN

waveguides with a 6 μm separation. The power coupling ratio is about 60% for a 1000 μm long waveguide which implies that the coupling coefficient κ is $0.886\text{x}10^{-3}$ μm^{-1}. In the other words, it requires a waveguide length of 1772.25 μm to get 100% power coupling ratio, i.e., $B^2 = \sin^2(L\kappa) = \sin^2(1772.25 * 0.886 * 10^{-3}) = 1$. Suppose the propagation constant mismatch δ of $1.69\text{x}10^{-4}$ μm^{-1} is applied to this 100% coupler, the new power coupling ratio is $B^2 = \left|\kappa \sin(L\sqrt{\kappa^2 + \delta^2}) / \sqrt{\kappa^2 + \delta^2}\right|^2 = 0.964$. The change is only 3.6%. It is too small to change significantly the rejection level.

3.3 Demonstration of High Speed Tunability

To demonstrate the high speed tunability of the LN-loop, the optical RF link measurement setup shown in Fig. 3-9 is setup. It uses a packaged LN-loop device provided by Sumitomo company, which is shown in Fig. 3-10. The device was evaluated as a modulator by applying RF signal to the phase tuning electrode through a SMA connector. The input light is obtained from the tunable laser at the power level of 4.77 dBm (3 mW). The output light is detected by a high speed photo detector (New Focus, 20 GHz) and then collected by an RF spectrum analyzer, HP70000.

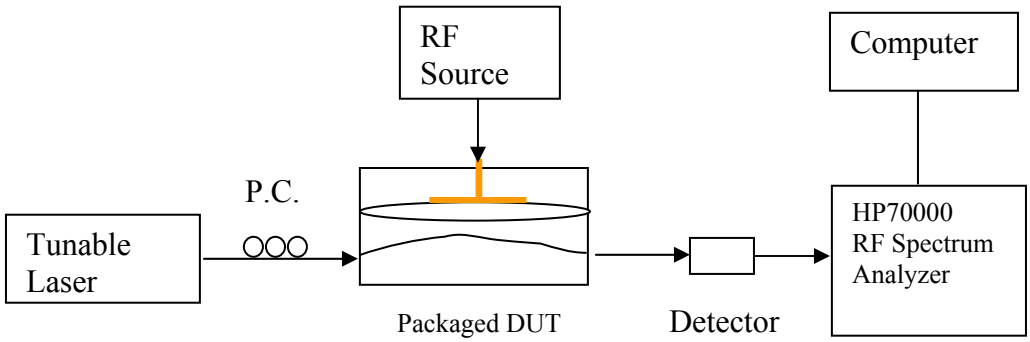

Fig. 3-9. High speed tunability measurement setup.

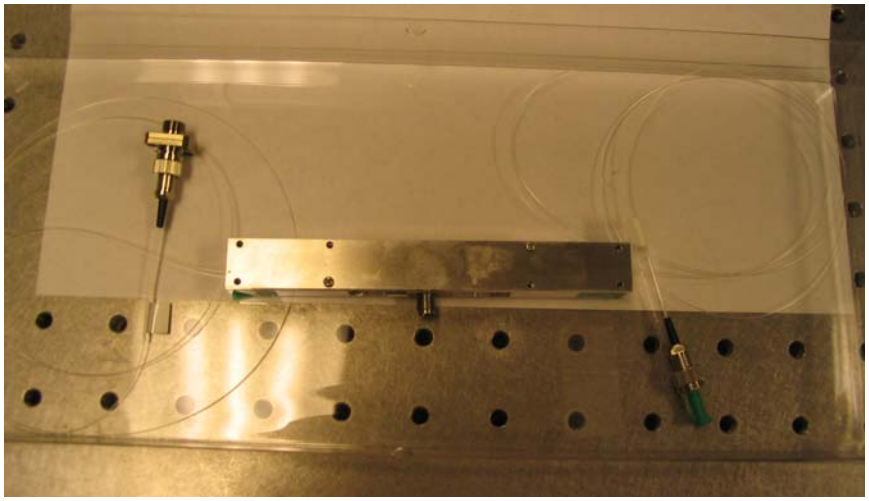

Fig. 3-10. The packaged LN-loop device. Only the phase tuning electrode has a SMA connector.

The first measurement is to search the maximum RF output the link can achieve by fine-tuning the input optical wavelength and the polarization controller. An example of the output on the RF spectrum analyzer is shown in Fig. 3-11 at the wavelength of 1550.45 nm, 1550.46 nm, and 1550.53 nm, respectively. A maximum output of -70 dBm is realized at an input RF power of 10 dBm, RF frequency of 0.5 GHz, optical power of 3 mW, and the wavelength of 1550.45 nm. The minimum RF output power is -95 dBm at the wavelength of 1550.53 nm.

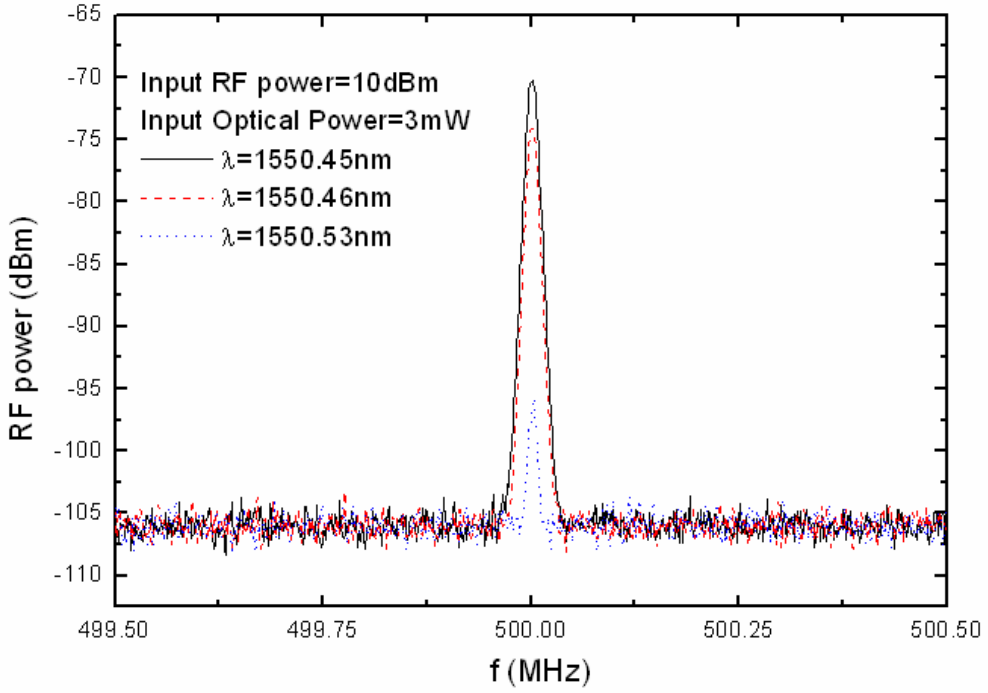

Fig. 3-11. Link RF output power measured with different wavelengths.

According to [1], the optical RF link gain is given by

$$G = 4P_{opt}^2 t_{ff}^2 \left(\frac{dT_N}{dV} \right) \eta^2 Z_{in} Z_{out} \qquad (3.6)$$

where P_{opt} (3 mW) is the input optical power; t_{ff} (~5 dB) is the fiber-to-fiber transmission loss; T_N is the normalized transfer curve; $\frac{dT_N}{dV}$ is the slope efficiency; η is the detector responsivity; Z_{in} (50 Ω) and Z_{out} (50 Ω) are the modulator input impedance and detector output impedance, the constant 4 is caused by RF reflection at the hot electrode which doubles the voltage on the optical waveguide if the reflection coefficient is assumed to be 1.

The normalized transfer curve is evaluated from the DC coupling tuning curves in Fig. 3-8. For example, for the wavelength of 1554.294nm, we have the normalized transfer curve shown in Fig. 3-12, where the transmission is normalized to the power at 0 V bias. In the first order approximation, we have $\frac{dT_N}{dV} = 0.0516$. Since the phase tuning electrode might have 2 times higher in efficiency than the coupling tuning electrode, the slope efficiency is taken to be 0.10 for the evaluation below.

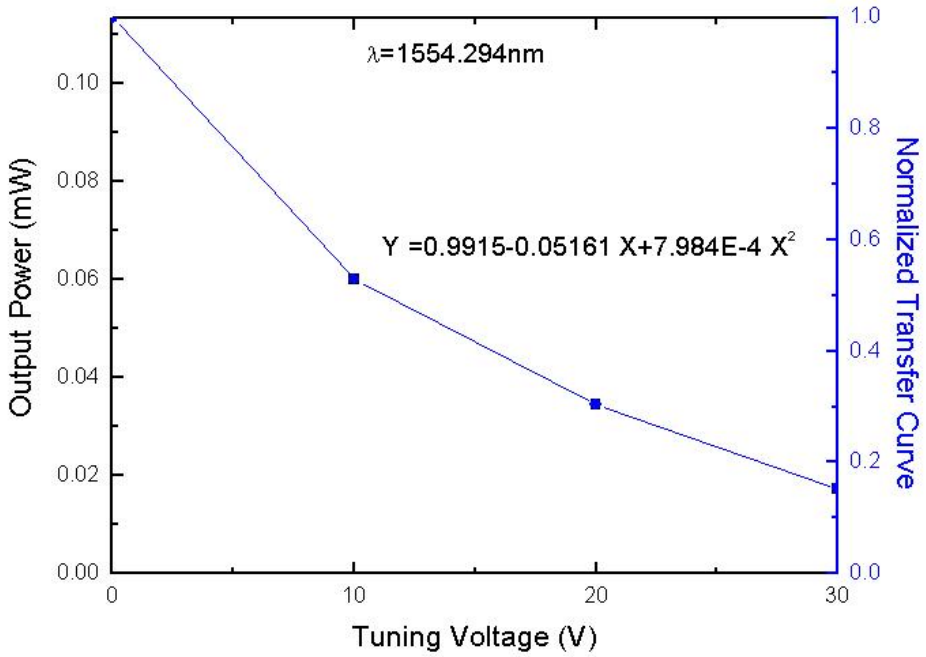

Fig. 3-12. Transmission and normalized transfer curve of wavelength of 1554.294 nm measured in DC coupling tuning.

Substituting all the terms in dB scale to the link gain equation, we have

$$\begin{aligned} G_{dB} &= 10\lg(4) + 20\lg(P_{opt}) + 20\lg(\frac{dT_N}{dV}) + 20\lg(t_{ff}) + 20\lg(\eta) + 10\lg(50*50) \\ &= 6.0 - 50.46 - 20 - 10 + 34 + 20\lg(\eta) \\ &= -40.44 + 20\lg(\eta) \end{aligned} \tag{3.7}$$

If the detector responsivity is close to 0.9 A/W which is the value most of the commercial detectors can achieve, we should have link gain in the order of -40 dB. However, the measured results are always below -80 dB which is 40 dB below the estimation. It turns out that the detector we used is the problem. Later on, we calibrated the detector and found that it has degraded because the built-in battery

dropped from 9 V to 4.6 V and the responsivity has dropped to 0.014 A/W, which reduced the gain by 39 dB.

The RF frequency response is also measured, as shown in Fig.3-13. To get rid of the effect of the detector responsivity, the results have been normalized to η=1 A/W. The curve shows that the link gain drops with increases in the frequency. The 3 dB bandwidth is about 5 GHz.

RF tuning measurements also have been done to the coupling tuning electrode and a similar phenomenon was observed at a lower efficiency. We only obtain a maximum output about -73 dBm, as shown in Fig. 3-14.

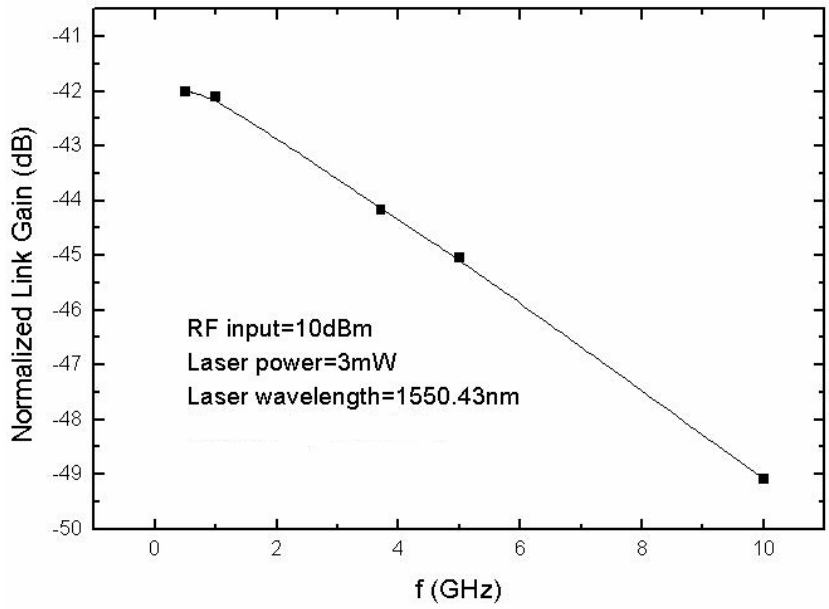

Fig. 3-13. Normalized link gain measured by applying RF signal to phase tuning electrode.

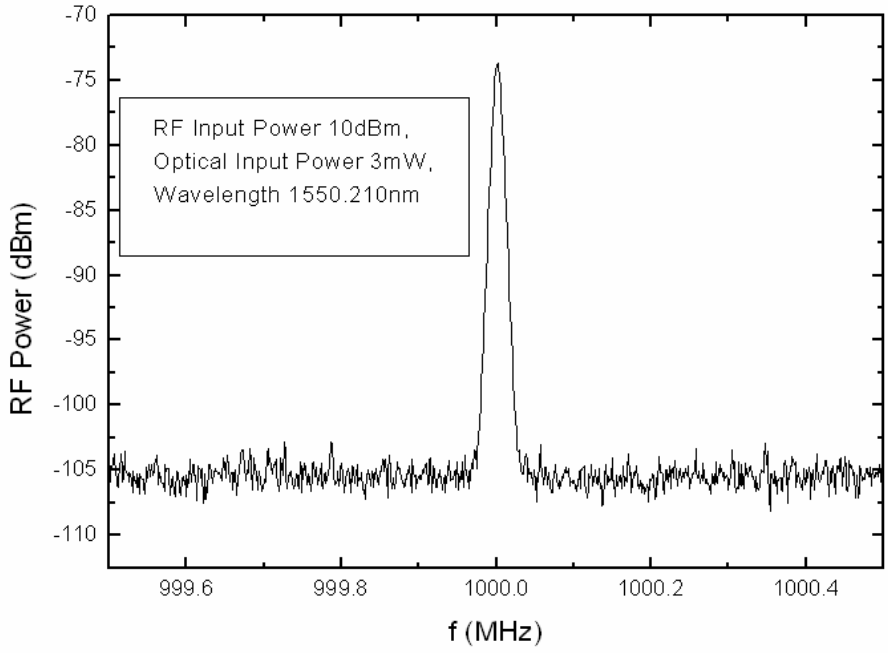

Fig. 3-14. RF response by applying RF signal to coupling tuning electrode.

3.4 Other Possible Device Applications of Y-Reflector

Although our current research focuses on the loop resonator, similar technique based on Y-reflector can be extended to other interesting new devices for optical RF signal processing. For example, the 1 to N splitter is a key device in many optical signal processing applications such as label recognition of photonic packet switching networks, [2] data rate conversion for large-capacity storage networks, [3] all-optical register, [4] and optical RF beam forming. [5] Different splitters have been created using surface-emitting planar lightwave circuits, acousto-optic modulator, [4] or a

fiber-based technique. [5] However, very few of them is easily re-programmed or fine-tuned to meet the dynamic variation of the networks.

We propose a novel, compact, multi-functional signal-processing device composed of a group of tunable couplers made on one single lithium niobate (LN) chip, as shown in Fig. 3-15. The couplers are arranged in parallel, similar to the steps in a ladder, so that we refer the device as a *coupler ladder*. The couplers transmit part of the light guided in a meandering waveguide, which acts as the built-in delay line. By applying voltage to electrodes at the coupler and along the meandering waveguide, the output amplitude and phase is tuned for each output channel. Thus the programmable property of the coupler ladder is achieved through an electric control circuit. Furthermore, the outputs channels are coherent with each other when a narrow band continuous wave (CW) laser is used as the source.

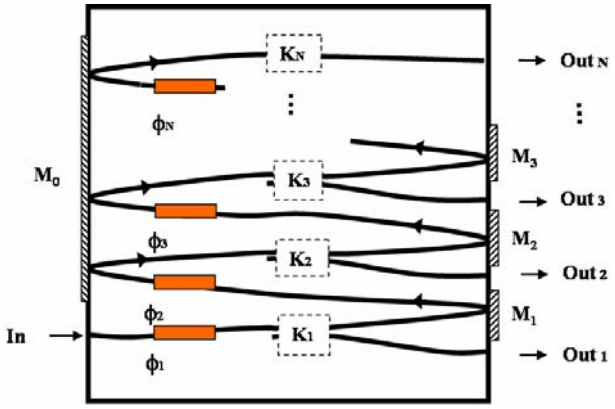

Fig. 3-15. A schematic diagram of the programmable coupler ladder.

In Fig. 3-15, Z-cut lithium niobate is chosen as the substrate material, due to its well-established fabrication technology. A meandering Titanium (Ti) diffused waveguide goes back and forth between the left and right facets of the lithium niobate substrate. Each turning point of the meandering waveguide at the facet forms a Y-reflector, which can completely guide the incident light from one branch to the other, analogous to a mirror reflecting a light beam from one direction to another in the free space.

For each left-to-right section of the meandering waveguide, a coupling waveguide is branched out from a certain point, so that a series of directional couplers is made in parallel to each other from the bottom to the top. In Fig. 3-15, K_1, K_2, K_3 … K_N represent the couplers. The facet at the termination of each coupling waveguide is optically transmittive so as to couple light to the outside. The number of outputs, N, is optimized subject to the limitation of the propagation loss.

The outputs, from 1 to N-1, are equal to each other. The final one, the N^{th} in Fig. 3-15, is a special one as it is the output of the meandering waveguide itself. There is actually no coupler for this channel. K_N is namely taken to be unity, representing an always-on state. This output can also be located at the opposite facet, depending on the applications.

Within the coupler ladder, the electrodes are used for two purposes: phase modulation and coupling coefficient modulation. Due to the excellent electro-optic property of lithium niobate, it is now routine to deposit the phase shifting electrodes along the meandering waveguide. In Fig.3-15, we use ϕ_1, ϕ_2, …, ϕ_N to represent the

phase shifting electrodes. Similarly, an electrically-controlled coupler or switch is also a well-established technology for Ti-diffused lithium niobate waveguide device, i.e., the coupling coefficients of K_1, K_2,…, K_{N-1} is tuned from 0 to 1 with proper voltage applied to the control electrodes. [7]

By tuning both the phase and the coupling coefficients, the output of every coupler can have arbitrary amplitude and phase modulations. The electro-optic response speed of lithium niobate is up to several tens of GHz, especially with traveling-wave type electrode. [6] Thus, high-speed tunability is achievable. A smart control circuit is employed to generate suitable control signals for the electrodes. In this context, the device can function as a programmable coupler ladder.

The most straightforward function of the coupler ladder is to split the input signal into N channels, achieving serial-to-parallel conversion similar to the traditional 1xN power splitter. However, this new device has a unique advantage over the traditional splitter; every output inherently has a relative delay to the other outputs. The relative delay time is determined by the length of the waveguide between adjacent couplers along the meandering waveguide.

Fig. 3-16 depicts the simplified diagram for the pulse propagation and alignment. N is set to 4 for convenience. It is interesting to note that if the built-in delay time correlates to the transmission bit rate then the output pulses will line up in the time axis. This is useful for signal processing applications such as label recognition in the packet switching networks.

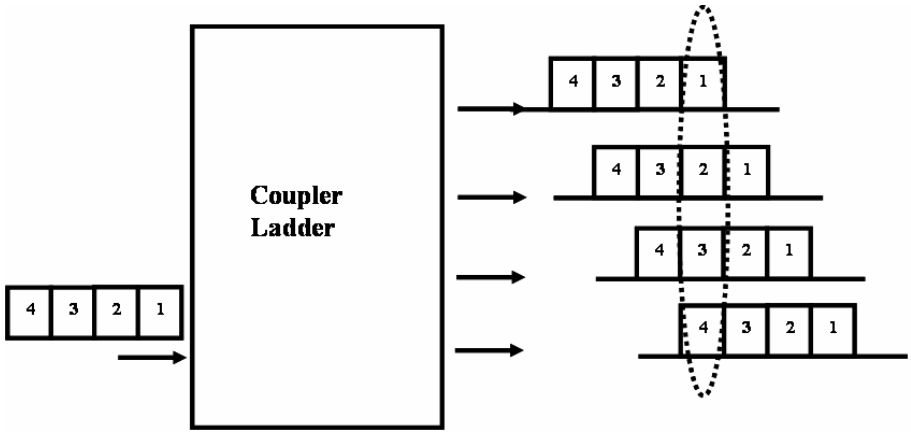

Fig. 3-16. Coupler ladder for pulse alignment after splitting.

More splitting functions is obtained with the help of an electrical control signal. As shown in Fig.3-17, the input pulse is sorted using the built-in delay. Assuming the control of the coupling coefficient K_i (i=1,2,3,4) is written under a synchronized clock, a different bit pattern is acquired by applying different control words for K_i. For example, for K1=K2=K3=K4=1, all the bits would be fanned out. For K1=K3=0 and K2=K4=1, only pulse 1 and pulse 3 would be swept out. This enables the device to perform signal processing at the bit level. If only one channel is allowed to be coupled out, the device becomes a programmable router.

By reversing the input and output ports, the device is also able to operate as a parallel-to-serial convertor with the help of a synchronization clock. Due to the transmission characteristic of the directional coupler, an advantage of this device is that when one channel (say, the 2^{nd} coupler) is open for the pulse to be coupled in, the undesired pulse flow coming from the upper channels (say, the 3^{rd} and 4^{th}) will be

transmitted to the dummy end of the coupler of channel 2, so that the interference between the pulses will be avoided. With proper waveguide design, the light reaching the dummy end will radiate out to the substrate, without causing interference to the transmission waveguide.

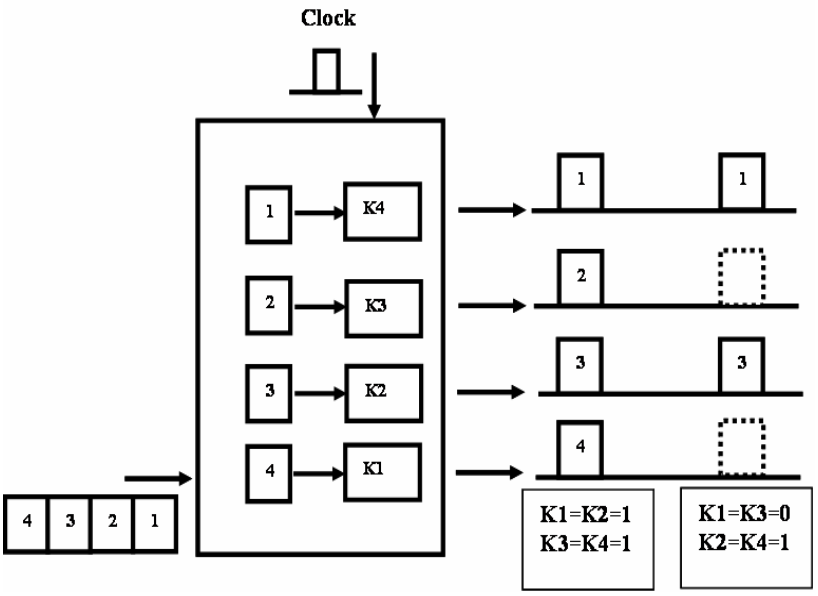

Fig. 3-17. Bit selection by different control words.

3.5 Summary

In this chapter, two generations of demo devices have been completed and evaluated for optical transmission response and electrical tunability. According to the curve fitting data to the experimental transmission results, each Y-reflector has an insertion loss between 1 to 1.7 dB if assuming the propagation loss of Ti:LN waveguide is 0.5 dB/cm. The DC frequency tunability of the loop is around 33.3 MHz/V or 175 MHz/(V·cm) by normalizing to the electrode length. AC modulation measurement shows normalized link gain of -42 dB for input optical power of 3 mW

which implies some interesting application of the loop for high efficient modulation or switching. The possibility to extend the Y-junction reflector technique to the 1xN power splitter is also discussed.

Reference

[1] C. Cox, III, E. Ackerman, R. Helkey, and G. E. Betts, "Techniques and performance of intensity-modulation direct-detection analog optical links," IEEE Trans. Microwave Theory Tech., Vol. 45, pp. 1375–1383, Aug. 1997.

[2] R. Takahashi, T. Nakahara, H. Takenouchi, and H. Suzuki, "40-Gbit/s Label Recognition and 1 x 4 Self-Routing Using Self-Serial-to-Parallel Conversion", IEEE Photon. Technol. Lett., Vol. 16, pp 692-694, Feb. 2004.

[3] H. Suzuki, R. Takahashi, T. Nakahara, H. Takenouchi, K. Takahata, T. Yasui, N. Kondo, and J. Yumoto, "Ultrafast photonic interfaces for storage networking using serial-to-parallel and parallel-to-serial conversion", Proc. of SPIE, Vol. 5069, pp 35-44, 2003.

[4] E. Lugagne Delpon, J. L. Oudar, and H. Lootvoet, "Operation of 4 x 1 optical register as a fast access optical buffer memory", Electron. Lett. , Vol. 33, pp1161-1162, Jun. 1997.

[5] R. D. Esman, M. Y. Frankel, J. L. Dexter, L. Goldberg, M. G. Parent, D. Stilwell, and D. G. Cooper, "Fiber-optic prism true time-delay antenna feed", IEEE Photon. Technol. Lett., Vol. 5, pp 1347-1349, 1993.

[6] H. S. Hinton, "Photonic Switching Using Directional Couplers", IEEE Comm. Magazine, Vol. 25, pp 16-26, 1987.

[7] S. K. Korotky, R. C. Alferness, C. H. Joyner, and L. L. Buhl, "14Gbit/sec optical signal encoding for λ=1.32 μm with double pulse driven of a Ti: LiNbO3 waveguide modulator", Electron. Lett., Vol. 20, pp132-133, 1984.

Chapter 4. Incoherent Optical RF Filter Using Differential Group Delay Module

4.1 Introduction to Transversal Filter

The incoherent optical RF filter has been developed for about three decades ever since the first proposal in 1976. [1] After some pioneer works in 1980s with optical fiber delay line [2-5], many experiment schemes have been introduced with new photonic devices developed in 1990s, e.g., the optical fiber Bragg gratings (FBG), the arrayed waveguide gratings (AWG), and the semiconductor optical amplifiers (SOA). [6] The most important transversal filters are summarized in Table 4-1 together with their pros and cons.

Although the key devices are different from scheme to scheme, the incoherent optical RF filter follows one basic working principle called transversal filtering, as depicted in Fig. 4-1. In the perspective of the impulse response, the incoming impulse is treated with serial-to-parallel conversion and divided into N paths, or so called N taps. Each path is applied with its delay time and signal weight. Then with parallel-to-serial conversion, the output N taps signal will be detected by the photodetector and converted into RF signal. Tapping and weighing are two most important issues for incoherent optical RF filter. Different tapping and weighing will generate different filtering functions. This could be understood from the time domain impulse response of the filter.

Table 4-1. The schemes of the transversal filters.

Tap Method	Pros	Cons	Reference
Fiber delay lines	1. Simple.	1. Not tunable. 2. Low Q. 3. Coherent noise limitation.	[30]
Active grating pairs	1. Very large number of taps (>>100), so that very high Q ~325 could be achieved. Q~900 is achieved with hybrid approach 2. Tunable if using chirped gratings. But no demonstration yet. 3. Square response is achieved by dual cavity parallel topology.	1. Precise gain control is required to avoid the onset lasing. 2. The working RF frequency couldn't be very high (~1GHz) as limited by the necessary length of EDFA. 3. Coherent noise limitation.	[9-13]
Chirped grating/array	1.Continuously Tunable. 2. Independently weight.	1. Small tap number, i.e., low Q. 2. Multiple wavelength source needed.	[14-20]
Spectrum slicing/AWG	1. No coherent noise. 2. Tunable.	1. Low Q. 2. Need broadband source.	[21-26]
Hi-Birefringence material	1. Overcome coherent noise limitation. 2. Theoretically infinite rejection level could be achieved for notch filter.	1. Hard to maintain polarization stability. 2. hard to realize tunability.	[27-30]

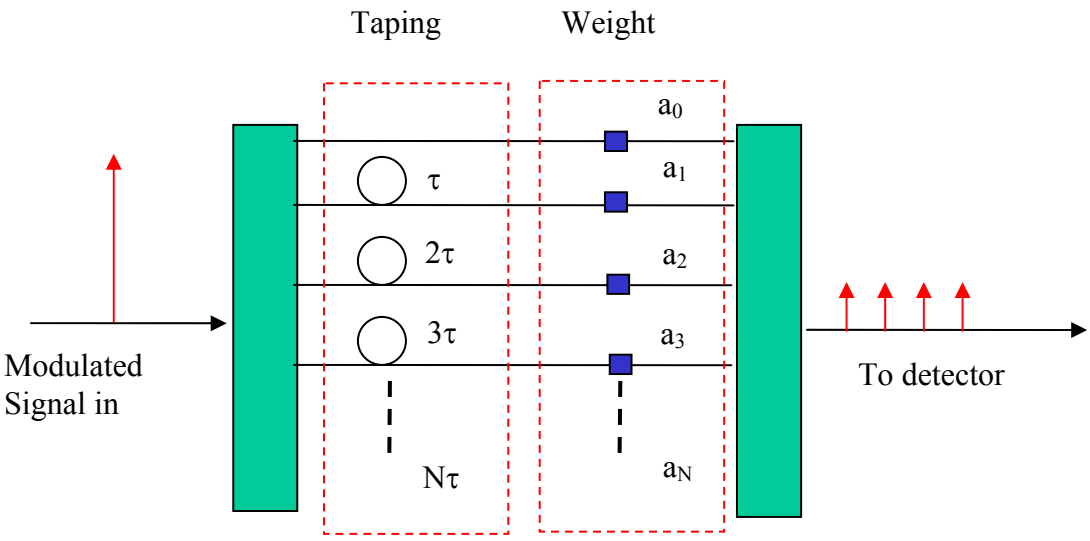

Fig. 4-1. The principle diagram of the transversal filter.

The time domain response of the transversal filter can be given by the convolution between the input signal $S_{in}(t)$ and the impulse response function h(t).

$$S_{out}(t) = h(t) * S_{in}(t) \qquad (4.1)$$

$$h(t) = \sum_{n=0}^{N} a_n \delta(t - n\tau) \qquad (4.2)$$

where a_n is the weights, n is the integer number, τ is the basic delay time, and δ is Dirac function.

For simplicity, we only consider equal weight case because the tapping technique is generally more distinctive to realize different transversal filters. Let's first derive the impulse response function for a 2-tap case with equal weights.

Assume the output of the laser has a line shape function g:

$$P_0 = \int_0^\infty g(\omega) g^*(\omega) d\omega = \int_0^\infty g^2 d\omega \,. \qquad (4.3)$$

where we take g as a real function.

When one of them transmits through the modulator modulated at frequency Ω and with modulation depth m, the output is given by

$$S(t) = g(\omega)(1 + m\cos(\Omega t))\cos(\omega t) \qquad (4.4)$$

After the transversal sampling of the first stage, say, two tapings with relative delay time τ, we get

$$S(t-\tau) = g(\omega)(1 + m\cos[\Omega(t-\tau)]\cos[\omega(t-\tau) + \theta(t)]. \quad (4.5)$$

The random phase θ(t) is to describe the relative phase stability caused by environmental factors, such as vibrations, or temperature variation.

The total signal after the parallel-to-serial conversion is written as

$$S_{sum}(t) = S(t) + S(t-\tau). \qquad (4.6)$$

The total power is

$$\begin{aligned} P_{sum}(t) &= S_{sum} \cdot S^*_{sum} = [S(t) + S(t-\tau)] \cdot [S^*(t) + S^*(t-\tau)] \\ &= S(t)S^*(t) + S(t-\tau)S^*(t-\tau) + S(t)S^*(t-\tau) + S^*(t)S(t-\tau) \qquad (4.7) \\ &= g^2 \left\{ \begin{array}{l} [1 + m\cos(\Omega t)]^2 \cos^2(\omega t) + [1 + m\cos[\Omega(t-\tau)]]^2 \cos^2[\omega(t-\tau) + \theta] \\ + 2(1 + m\cos(\Omega t))[1 + m\cos[\Omega(t-\tau)]]\cos(\omega t)\cos[\omega(t-\tau) + \theta] \end{array} \right\} \end{aligned}$$

The photocurrent of the square-law detector is given by

$$i(t) = \eta \overline{P}_{sum} = \eta g^2 \left\{ \begin{array}{l} \frac{1}{2}[1 + m\cos(\Omega t)]^2 + \frac{1}{2}[1 + m\cos[\Omega(t-\tau)]]^2 \\ + [1 + m\cos(\Omega t)][1 + m\cos[\Omega(t-\tau)]]\cos[\omega\tau - \theta] \end{array} \right\} \qquad (3.8)$$

where $\overline{P}_{sum}$ means the optical carrier has been averaged over the relatively long time.

What we are interested in are AC terms. So we neglect DC terms and rewrite the photocurrent as

$$i(t)=\eta g^2\left\{\begin{array}{l} m\cos(\Omega t)+\frac{m^2}{4}\cos(2\Omega t)+m\cos[\Omega(t-\tau)]+\frac{m^2}{4}\cos[2\Omega(t-\tau)] \\ +\left\{m\cos(\Omega t)+m\cos[\Omega(t-\tau)]+\frac{m^2}{2}[\cos[2\Omega t-\Omega\tau]+\cos[\Omega\tau]]\right\}\cos[\omega\tau-\theta] \end{array}\right\} \tag{4.9}$$

Further more, let's neglect the harmonics since they are proportional to small value m^2. Now we have

$$\begin{aligned} i(t) &= m\eta g^2\{\cos(\Omega t)+\cos[\Omega(t-\tau)]\}[1+\cos(\omega\tau-\theta)] \\ &= 2m\eta g^2\cos\left(\frac{\Omega\tau}{2}\right)\cos[\Omega t-\frac{\Omega\tau}{2}][1+\cos(\omega\tau-\theta)] \end{aligned} \tag{4.10}$$

The total current could be obtained by doing integration over the source spectrum.

$$\begin{aligned} I(t) &= \int_0^\infty i(t)d\omega = 2m\eta\cos\left(\frac{\Omega\tau}{2}\right)\cos\left[\Omega t-\frac{\Omega\tau}{2}\right]\int_0^\infty g^2(\omega)[1+\cos(\omega\tau-\theta)]d\omega \\ &= 2m\eta\cos\left(\frac{\Omega\tau}{2}\right)\left[P_0+\int_0^\infty g^2(\omega)\cos(\omega\tau-\theta)d\omega\right]\cos\left[\Omega t-\frac{\Omega\tau}{2}\right] \end{aligned} \tag{4.11}$$

Looking into the normalized amplitude of the photocurrent, we get

$$A=\frac{I(t)}{2m\eta P_0}=\cos\left(\frac{\Omega\tau}{2}\right)\left[1+\frac{1}{P_0}\int_0^\infty g^2\cos(\omega\tau-\theta)d\omega\right] \tag{4.12}$$

We have to consider the detail of the line shape function. For simplicity, we take a square shape function as the approximation.

$$\int_{\omega_0-\frac{1}{2}\Delta\omega}^{\omega_0+\frac{1}{2}\Delta\omega} g^2 d\omega = P_0 \tag{4.13}$$

where ω_0 is the central frequency and $\Delta\omega$ is the band width.

Thus the line shape function is a constant.

$$g^2 = P_0 / \Delta\omega \tag{4.14}$$

And also assuming that θ is identical for all the frequencies.

$$\begin{aligned} A &= \cos\left(\frac{\Omega\tau}{2}\right)\left[1+\frac{1}{\Delta\omega}\int_{\omega_0-\frac{1}{2}\Delta\omega}^{\omega_0+\frac{1}{2}\Delta\omega}\cos(\omega\tau-\theta)d\omega\right] \\ &= \cos\left(\frac{\Omega\tau}{2}\right)\left[1+\frac{\sin\left[\left(\omega_0+\frac{1}{2}\Delta\omega\right)\tau-\theta\right]-\sin\left[\left(\omega_0-\frac{1}{2}\Delta\omega\right)\tau-\theta\right]}{\Delta\omega\tau}\right] \\ &= \cos\left(\frac{\Omega\tau}{2}\right)\left[1+\frac{\sin\left(\frac{\Delta\omega\tau}{2}\right)}{\frac{\Delta\omega\tau}{2}}\cos(\omega_0\tau-\theta)\right] \end{aligned} \tag{4.15}$$

The response is mainly determined by the intrinsic delay time τ, the RF frequency Ω, line width of the source Δω, and the random phase θ. The second term is to describe the residual coherent noise. If the light source is with very long coherent time (small linewidth Δω), the residual coherent noise could be very large.

The similar derivation could be extended to N-taps with equal weights. We have

$$\begin{aligned} S_{sum}(t) &= \sum_{n=0}^{N-1} S(t-n\tau) \\ &= \sum_{n=0}^{N-1} g\left[1+m\cos\Omega(t-n\tau)\right]\cos\left[\omega(t-n\tau)+\theta_n\right] \end{aligned} \tag{4.16}$$

$$P_{sum} = S_{sum}^2 = \sum_{k,n=0}^{N-1} g^2 \left[1 + m\cos\Omega(t - k\tau)\right]\left[1 + m\cos\Omega(t - n\tau)\right] \cdot \cos\left[\omega(t - n\tau) - \theta_n\right]\cos\left[\omega(t - k\tau) - \theta_k\right] \quad (4.17)$$

Neglecting DC terms and the small terms proportional to m^2, we get

$$\overline{P_{sum}} = \sum_{k,n=0}^{N-1} \frac{1}{2} g^2 m\left[\cos\Omega(t - k\tau) + \cos\Omega(t - n\tau)\right]\cos\left[\omega\tau(n - k) + \theta_{nk}\right] \quad (4.18)$$

This is a complex expression. We can only get analytical solution with assumptions: (1) only concern the coherent interference between adjacent delay times, i.e., between n and n-1 or n+1, since it is the strongest effect; (2) $\theta_{n,n-1} = \theta$, i.e., the phase has the same relative change between adjacent delay paths.

Then we still can get a simple expression as below:

$$\overline{P_{sum}} = \sum_{n=0}^{N-1} g^2 m\cos\Omega(t - n\tau)\left[1 + \cos(\omega\tau + \theta)\right] \quad (4.19)$$

Do the same derivations as 2-tap model above, we get

$$A = \frac{\sin\left(\frac{N\Omega\tau}{2}\right)}{\sin\left(\frac{\Omega\tau}{2}\right)}\left[1 + \frac{\sin\left(\frac{\Delta\omega\tau}{2}\right)}{\frac{\Delta\omega\tau}{2}}\cos(\omega_0\tau + \theta)\right] \quad (4.20)$$

For the case of incoherent source with very large linewidth $\Delta\omega$, the coherent noise could be neglected. The output RF power response is proportional to

$$P_{RF} \propto A^2 = \left|\frac{\sin\left(\frac{N\Omega\tau}{2}\right)}{\sin\left(\frac{\Omega\tau}{2}\right)}\right|^2 \quad (4.21)$$

An example of the frequency response, neglecting the noise, with intrinsic delay time τ=45.2 ps is shown in Fig. 4-2, where the RF frequency scans from DC to 50 GHz and the output P_{RF} is in dB unit. One trend is clearly observed: the larger is N, the narrower is the main passband and the smaller is the sideband. For N=2, the filter is generally called notch-filter, used to block out certain frequency which is located at the notch position of the response curve. The notch happens at the frequency points that meet the conditions of

$$\begin{aligned} &\sin(N\Omega\tau/2)=0; \\ &\sin(\Omega\tau/2)\neq 0; \end{aligned} \tag{4.22}$$

And the peaks of the main passband are located at the frequency points that meet

$$\begin{aligned} &\sin(N\Omega\tau/2)=1; \\ &\sin(\Omega\tau/2)=1; \end{aligned} \tag{4.23}$$

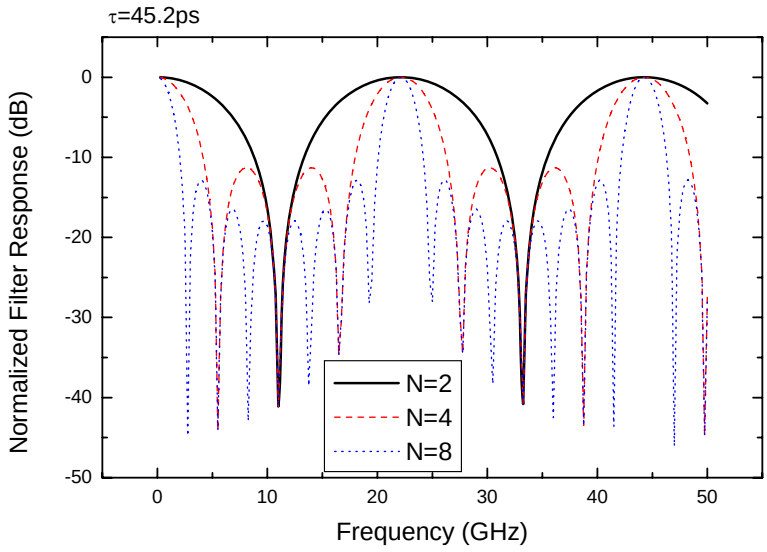

Fig. 4-2. Normalized frequency response of the transversal filter with equal weights.

Nowadays people generally use laser as the light source to realize the incoherent optical RF filter because laser has large output power and easy to couple to fiber. However, laser is generally with very long coherent time. From equation (4.20), we can see that this optical coherence of the source may cause the residual coherent noise. [12-14] This limitation can be removed by using the two orthogonal polarizations in Hi-Birefringence (Hi-Bi) fiber. [12] It was noted that the time delay in Hi-Bi fiber is tuned through temperature variation and its performance is affected by the ambient temperature variation.

In this work, we demonstrate a novel tunable notch filter through an off-the-shelf fiber-optic programmable differential group delay (DGD) module, DGD-6B1, made by General Photonics Corp. [15]. This filter serves two functions: it removes the limitation due to the coherence of the light source, and it allows digitally tunable notch-filtering operation.

4.2 DGD Module

As described in [15], the DGD module, with dimensions of 134 x 70 x 20 mm^3, has 6 phase delay sections each of which consists of a birefringent crystal and a magneto-optic polarization switch. A schematic view of the sections is shown in Fig. 4-3. The lengths of the birefringent crystals are arranged in a binary power series, incremented by a factor of 2 for each section. The relative delay between two orthogonal linear polarization states is digitally switched either from –45.2 to +45.2 ps or from 0.28 ps to 89.6 ps, with a resolution of 1.36 ps, i.e., 6-bit resolution. A total 64

DGD states is uniquely represented by a 6-bit digital highs and lows, as shown in the logic table Table. 4-2. The average DGD switching time is 150 μs. The optical insertion loss is 2.4 dB.

The operation of the module is computer-controlled using the software provided by the manufacturer. Due to the small size and the programmability of DGD, the filter is quite compact and robust in operation. As described previously, the logic high and low of each bit is directly verified by inspecting the corresponding LED on the module board. LED "on" represents "1" for the logic table; LED "off" represents "0" for the logic table. The appearance of the module is shown in Fig. 4-4.

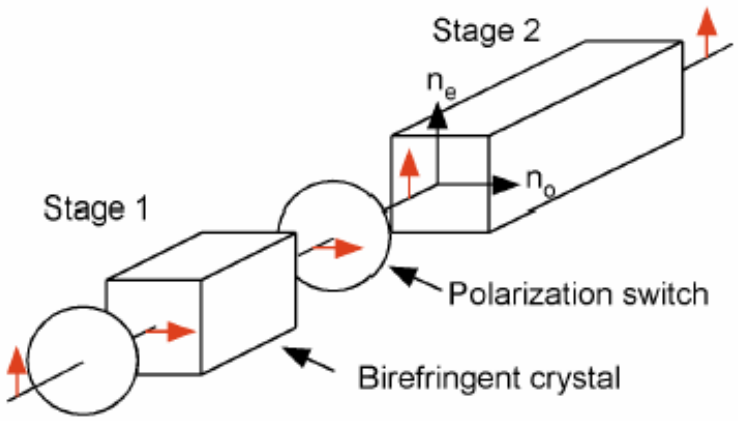

Fig. 4-3. The stage arrangement of DGD module.

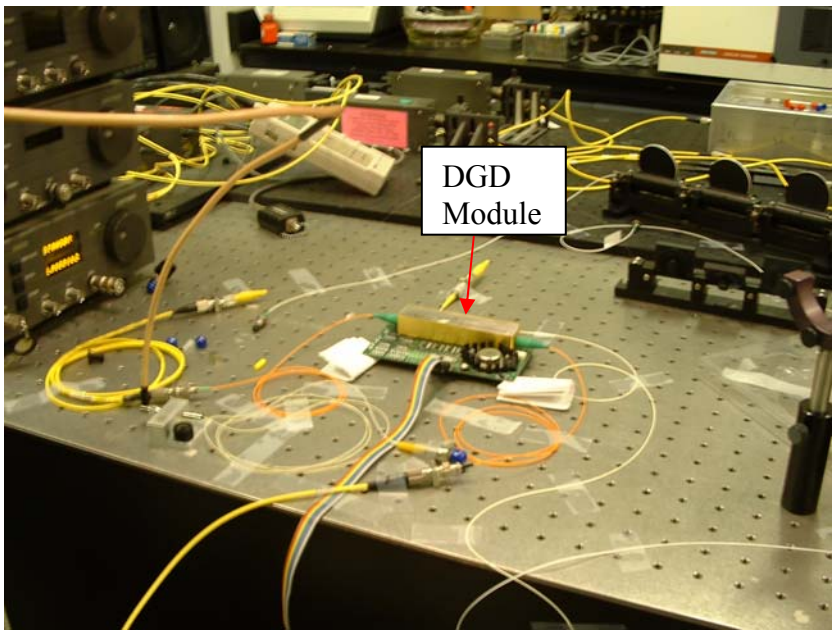

Fig. 4-4. The appearance of the DGD module.

Table 4-2. State table of the DGD units.

Logic Table	DGD1 (ps)	DGD2 (ps)	Logic Table	DGD1 (ps)	DGD2 (ps)
(1,1,1,1,1,0)	-45.17	0.28	(1,1,1,1,0,0)	0.68	45.6
(0,1,1,1,1,1)	-43.68	1.76	(0,1,1,1,0,1)	2.1	47.08
(0,0,1,1,1,0)	-42.26	3.12	(0,0,1,1,0,0)	3.42	48.48
(1,0,1,1,1,1)	-40.79	4.6	(1,0,1,1,0,1)	4.99	49.86
(1,0,0,1,1,0)	-39.42	6	(1,0,0,1,0,0)	6.35	51.28
(0,0,0,1,1,1)	-37.83	7.4	(0,0,0,1,0,1)	7.91	52.7
(0,1,0,1,1,0)	-36.6	8.8	(0,1,0,1,0,0)	9.23	54.14
(1,1,0,1,1,1)	-35	10.16	(1,1,0,1,0,1)	10.79	55.58
(1,1,0,0,1,0)	-33.63	11.64	(1,1,0,0,0,0)	12.07	57
(0,1,0,0,1,1)	-32.11	13.12	(0,1,0,0,0,1)	13.63	58.4
(0,0,0,0,1,0)	-30.8	14.56	(0,0,0,0,0,0)	14.96	59.84
(1,0,0,0,1,1)	-29.2	16	(1,0,0,0,0,1)	16.5	61.16
(1,0,1,0,1,0)	-27.84	17.36	(1,0,1,0,0,0)	17.84	62.56
(0,0,1,0,1,1)	-26.3	18.8	(0,0,1,0,0,1)	19.39	64.12
(0,1,1,0,1,0)	-24.96	20.08	(0,1,1,0,0,0)	20.83	65.6
(1,1,1,0,1,1)	-23.5	21.6	(1,1,1,0,0,1)	22.3	67.1
(1,1,1,0,0,0)	-22.29	22.98	(1,1,1,0,1,0)	23.36	68.56
(0,1,1,0,0,1)	-20.75	24.4	(0,1,1,0,1,1)	24.95	69.96
(0,0,1,0,0,0)	-19.41	25.78	(0,0,1,0,1,0)	26.33	71.34
(1,0,1,0,0,1)	-17.84	27.2	(1,0,1,0,1,1)	27.87	72.72
(1,0,0,0,0,0)	-16.51	28.68	(1,0,0,0,1,0)	29.2	74.12
(0,0,0,0,0,1)	-14.97	30.12	(0,0,0,0,1,1)	30.78	75.52
(0,1,0,0,0,0)	-13.61	31.52	(0,1,0,0,1,0)	32.11	76.9
(1,1,0,0,0,1)	-12.05	32.88	(1,1,0,0,1,1)	33.7	78.4
(1,1,0,1,0,0)	-10.8	34.28	(1,1,0,1,1,0)	34.91	79.8
(0,1,0,1,0,1)	-9.23	35.8	(0,1,0,1,1,1)	36.44	81.28
(0,0,0,1,0,0)	-7.9	37.2	(0,0,0,1,1,0)	37.83	82.68
(1,0,0,1,0,1)	-6.35	38.66	(1,0,0,1,1,1)	39.34	84.06
(1,0,1,1,0,0)	-4.99	40	(1,0,1,1,1,0)	40.65	85.42
(0,0,1,1,0,1)	-3.47	41.46	(0,0,1,1,1,1)	42.27	86.84
(0,1,1,1,0,0)	-2.1	42.8	(0,1,1,1,1,0)	43.68	88.22
(1,1,1,1,0,1)	-0.68	44.16	(1,1,1,1,1,1)	45.18	89.6

4.3 Tunable Notch Filter Based on DGD Module

Fig.4-5 depicts the experiment setup. The source is a single-mode Alcatel DFB laser with a linewidth of 2 to 5 MHz. It has a relatively long coherence time. In the test set up, the CW output of laser is modulated by a Mach-Zehnder $LiNbO_3$ modulator with a 3-dB bandwidth of 10 GHz. The polarization controller adjusts the input polarization to the DGD module, i.e., at an azimuth of 45° to the polarization axis of DGD, so that the two orthogonal polarization states is equally excited, as shown in Fig. 4-6.

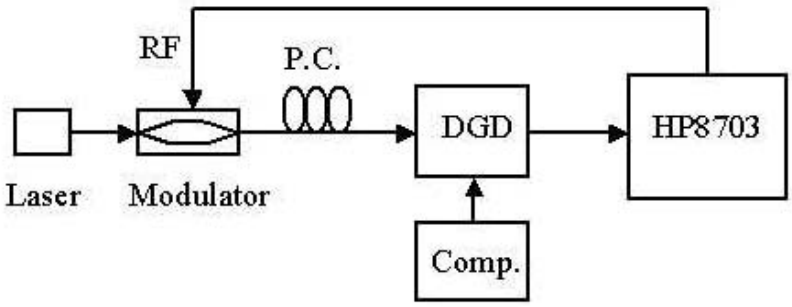

Fig. 4-5. Measurement setup of the notch filter based on DGD module.

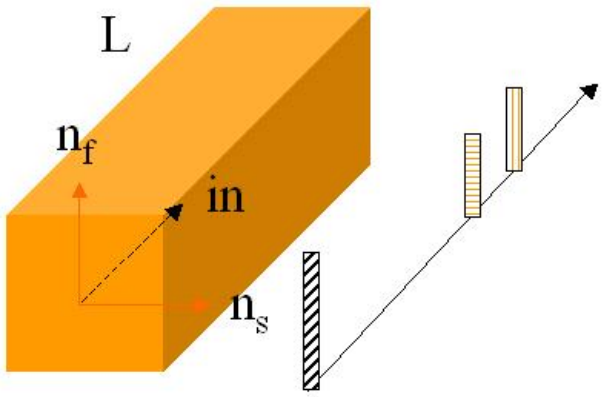

Fig. 4-6. Polarization direction of the incident beam. With 45° azimuth, one input pulse will generate two orthogonal output taps.

The minimum and maximum relative delays of the present DGD module are 0.68 ps and 45.2 ps respectively, corresponding to the first notch frequency (n=0) at 735 GHz and 11.06 GHz respectively. In the vicinity of 11 GHz, where the filter was tested, the tuning step is about 0.33 GHz which is limited by the bit resolution of the DGD module.

The operation of this notch filter is described as follows. The six sections of the DGD module are separately biased to give a relative delay time τ between the two orthogonal polarizations. When the modulated optical input is properly polarized with respect to the module, the optical output consists of two orthogonal polarizations with a relative delay time τ between them. The normalized output power spectrum, $P_N(\Omega)$ at the detector takes the form of:

$$P_N(\Omega) = \cos^2 \pi\Omega\tau, \qquad (4.24)$$

where Ω is the modulating microwave frequency. Thus the notches occur when

$$\Omega\tau = n + \frac{1}{2}, \qquad (4.25)$$

where n is an integer number.

Fig. 4-7 depicts the simulated normalized power spectrum of the notch filter after the detector, when the delay time is set at 45.2 ps. In principle, the rejection level of this filter could reach infinity when the two orthogonal states are equally excited. In practice, due to the unequal optical loss, unbalanced excitation of the two states, and the noise floor of the system, the observed rejection level remains finite in value.

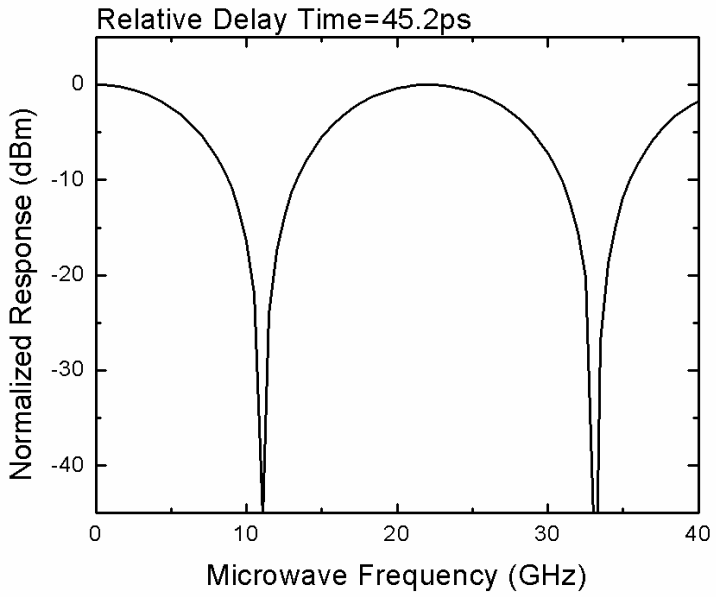

Fig. 4-7. Simulated frequency response of the notch filter at delay time 45.2 ps.

Fig. 4-8 shows the measurement results when the delay time is set at 45.2 ps. When linearly polarized light is launched along one of the polarization axes of the DGD module, i.e., θ=0°, no filter function is expected. This is similar to the observation in [12] using the Hi-Bi fiber delay line. However, using an input linearly polarized at an azimuth of 45° to the two polarization axis, two orthogonal modes are excited with a relative delay of 45.2 ps, and the notch frequency at 11.06 GHz is observed, with a maximum rejection level greater than 50 dB.

Fig. 4-9 shows that when the delay time is tuned from 45.2 ps to 40.6 and 34.9 ps, the notch is moved to 12.3 and 14.3 GHz respectively. We notice that the rejection level can even reach 60 dB, limited by the noise floor finally. But this high rejection level can not be maintained for long time and come back to 50 dB after several seconds.

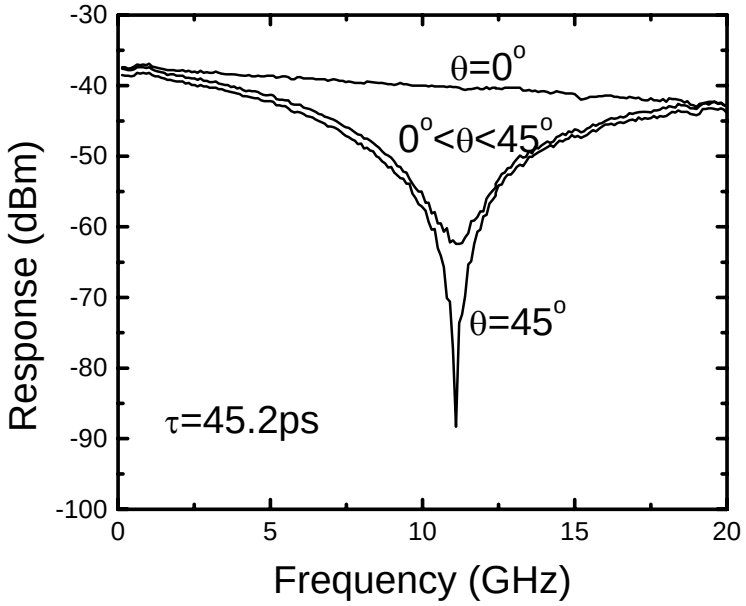

Fig. 4-8. Detected output as a function of frequency when input polarization azimuth adjusted.

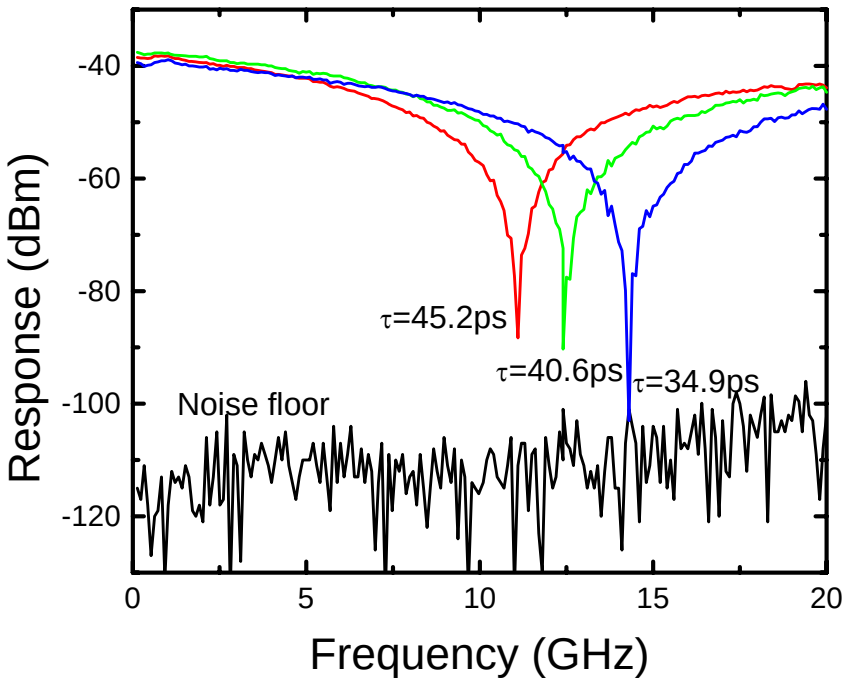

Fig. 4-9. Notch frequency is tuned by adjusting delay time of the DGD.

Next, we examine the filter function at a fixed modulation frequency at the input as the delay time is scanned. The input modulation frequency is set at 13.2 GHz and then the delay time of the DGD module is swift from 0.68 to 45.2 ps. In the measurement set up, the fixed modulation frequency is generated by an RF synthesizer, HP83620A, while the output is detected by an external high speed detector followed by a microwave spectrum analyzer, HP70000. The spectrum analyzer, at a resolution bandwidth of 100 kHz and span of 5 MHz, has a noise floor of around –77.0 dBm. The first notch for this input occurs when τ is around 37.8 ps, as shown in Fig.4-10.

The two insets in Fig. 4-10 show the spectra at delay time of 0.68 ps (left) and 37.8 ps (right), respectively.

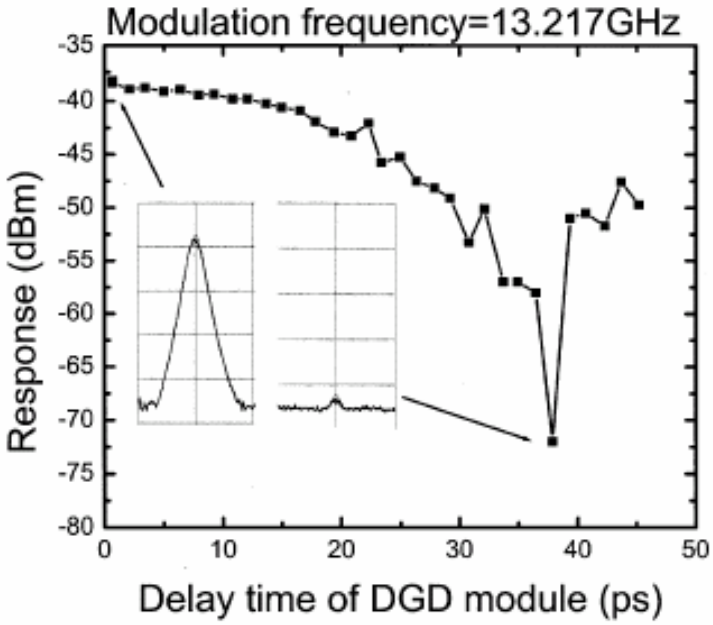

Fig. 4-10. Output response at the spectrum analyzer as a function of the delay time, the modulation frequency is fixed at 13.2 GHz. The spectrum analyzer is set at a resolution bandwidth of 100 kHz and span of 5 MHz, and has a noise floor of around -77.0 dBm.

The polarization switchers inside the DGD module will consume electric power and heat up the module. To investigate the thermal stability of the DGD module, we stick a thermometer to the package surface of the crystal and measured the temperature variation after turning the module on. It shows that the temperature keeps going up from 22.6 °C to 37.4 °C within 50 minutes before it is stable. About 200 MHz frequency deviation for the notch was observed, as shown in Fig.4-11. We did

not observe obvious effect from vibration even though our experiment was done on a common table.

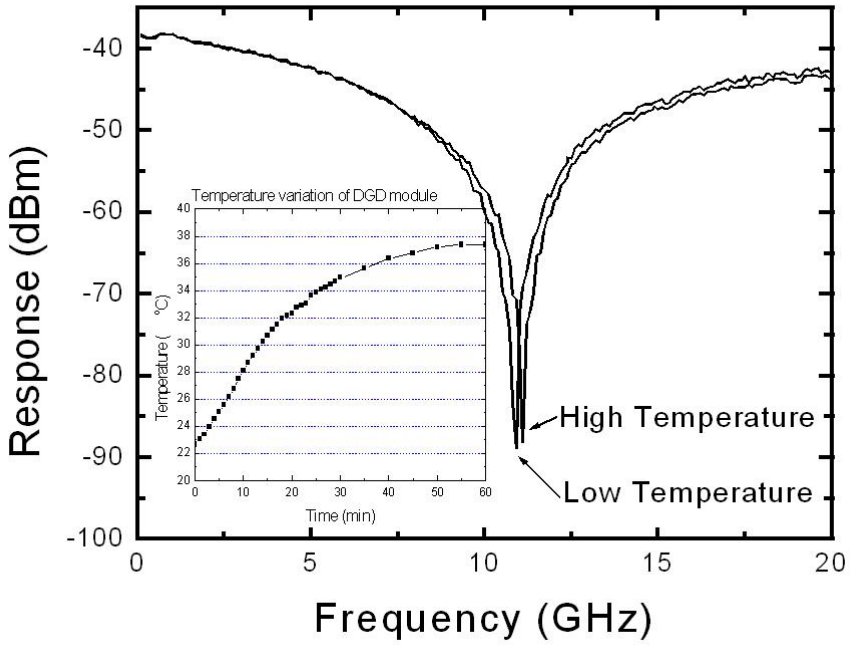

Fig. 4-11. Temperature sensitivity of the DGD module.

4.4 Four-tap Transversal Filter Using Two DGD Modules

More complicated filter response, such as bandpass filter, could be achieved by setting multiple DGD modules with different delay in parallel and detected by detector array, similar to the method used in [16]. But, of course, more considerations, such as absolute delay time compensation should be taken. Here we take four-tap transversal filter using two DGD modules as example. The arrangement of the DGDs is shown in Fig. 4-12.

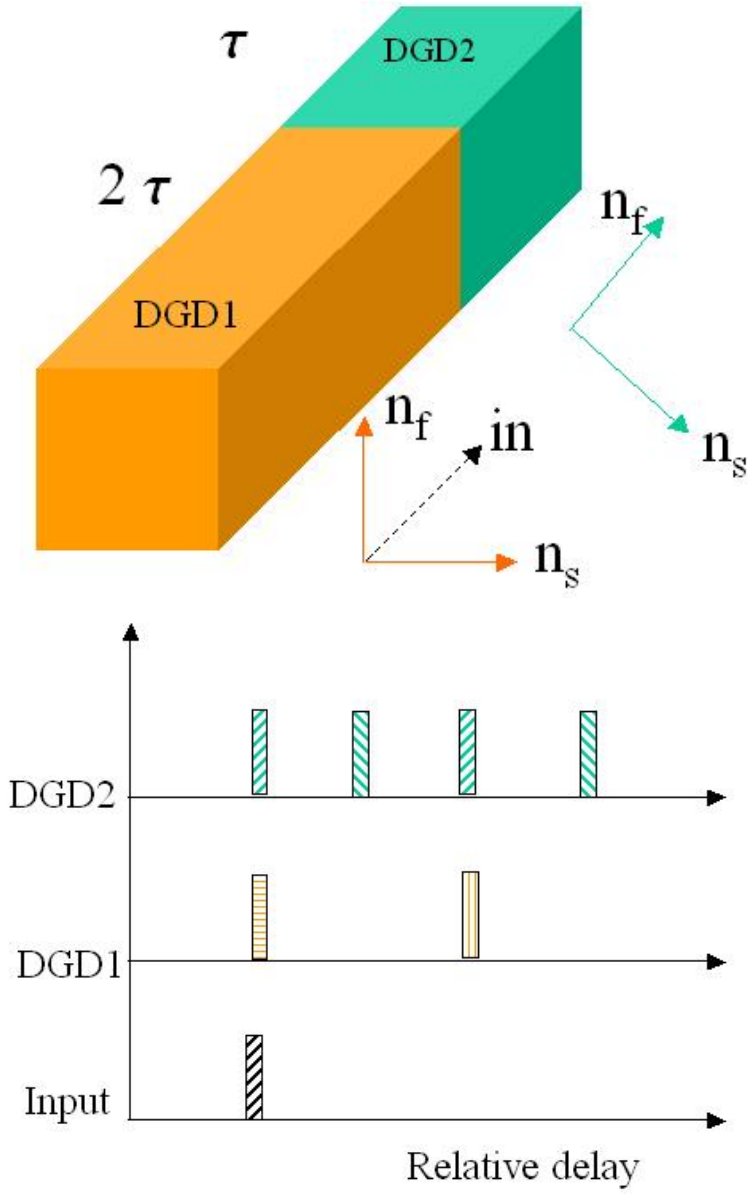

Fig. 4-12. The arrangement of two DGDs (upper) for four tapping generation after the signal propagating through two DGDs (bottom).

The input signal is RF intensity modulated optical beam, described by $S(t) = I_0(1 + m\cos(2\pi\Omega t))$. When it goes through two DGDs, four taps of signal are generated as

$$\begin{aligned} S_1(t) &= \frac{I_0}{4}[1 + m\cos(2\pi\Omega t)] \\ S_2(t) &= \frac{I_0}{4}[1 + m\cos(2\pi\Omega(t - \tau_2))] \\ S_3(t) &= \frac{I_0}{4}[1 + m\cos(2\pi\Omega(t - \tau_1))] \\ S_4(t) &= \frac{I_0}{4}[1 + m\cos(2\pi\Omega(t - \tau_1 - \tau_2))] \end{aligned} \tag{4.26}$$

Neglecting the DC terms, the AC terms will beat with each other in the detector, i.e.,

$$\begin{aligned} & S_1 + S_2 + S_3 + S_4 \\ &= \frac{mI_0}{4}\{\cos[2\pi\Omega t] + \cos[2\pi\Omega(t - \tau_2)] + \cos[2\pi\Omega(t - \tau_1)] + \cos[2\pi\Omega(t - \tau_1 - \tau_2)]\} \\ &= mI_0\cos[\frac{2\pi\Omega\tau_1}{2}]\cos[\frac{2\pi\Omega\tau_2}{2}]\cos[2\pi\Omega\left(t - \frac{\tau_1 + \tau_2}{2}\right)] \end{aligned} \tag{4.27}$$

The amplitude of AC frequency response at the output of the detector, which shows in the screen of HP8703, is proportional to $A(\Omega) = mI_0\cos[\frac{2\pi\Omega\tau_1}{2}]\cos[\frac{2\pi\Omega\tau_2}{2}]$.

In our measurement, we first set $\tau_1 = 89.6\,ps$ and $\tau_2 = 45.2\,ps$, the frequency response is $A(\Omega) = mI_0\cos[\frac{2\pi\Omega \times 89.6\,ps}{2}]\cos[\frac{2\pi\Omega \times 45.2\,ps}{2}]$.

We plot out the normalized frequency response $\frac{A(\Omega)}{mI_0} = \cos[\frac{2\pi\Omega \times 89.6ps}{2}]\cos[\frac{2\pi\Omega \times 45.2ps}{2}]$ in Fig. 4-13.

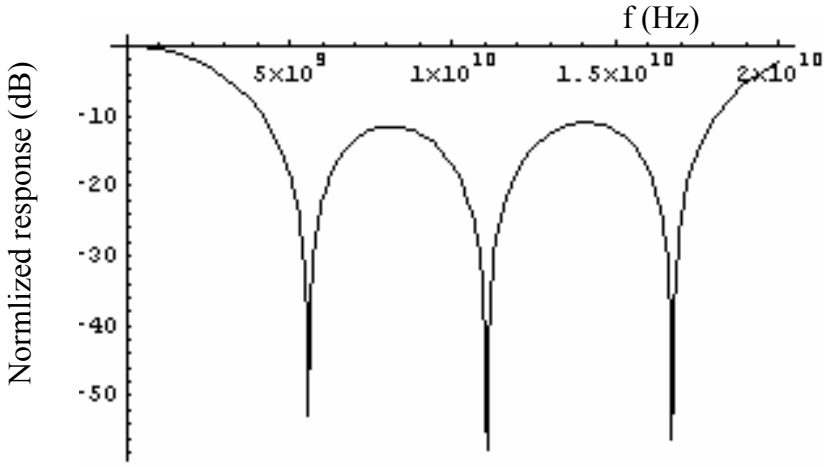

Fig. 4-13. Normalized response of 4-tap transversal filter.

It has notches at the conditions of $\frac{2\pi\Omega \times 89.6ps}{2} = \frac{\pi}{2} + n\pi$ and $\frac{2\pi\Omega \times 45.2ps}{2} = \frac{\pi}{2} + n\pi$. In the range of 130 MHz to 20 GHz, there are totally 3 notches

$$\frac{2\pi\Omega \times 89.6ps}{2} = \frac{\pi}{2} \Rightarrow \Omega_1 = 5.58GHz \tag{4.28}$$

$$\frac{2\pi\Omega \times 89.6ps}{2} = \frac{3\pi}{2} \Rightarrow \Omega_2 = 16.74GHz \tag{4.29}$$

$$\frac{2\pi\Omega \times 45.2ps}{2} = \frac{\pi}{2} \Rightarrow \Omega_3 = 11.06GHz \tag{4.30}$$

To verify the predicted frequency response, the measurement with two DGD modules has been set up as Fig. 4-14.

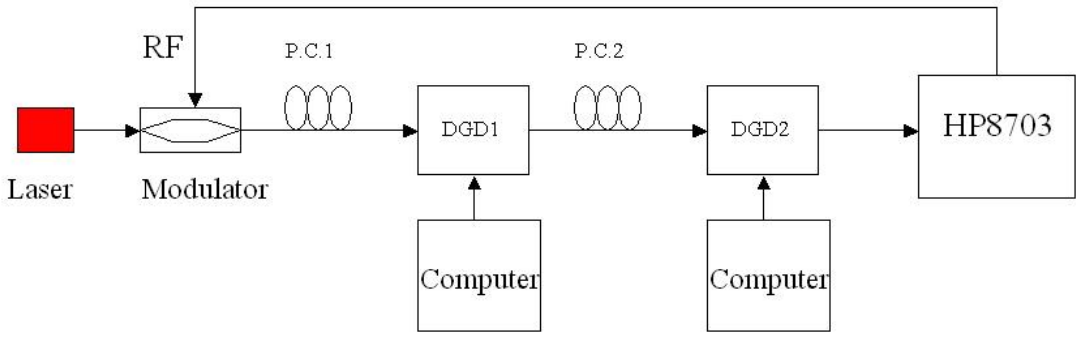

Fig. 4-14. Setup to measure 4-tap transversal filter response.

From the measurement result in Fig. 4-15, we see three marks shows the notch frequencies of 5.52GH, 11.1GHz, and 16.8GHz, respectively, pretty close to the theoretical prediction. Later on, we tuned $\tau_1 = 85.4\,ps$ and $\tau_2 = 42.3\,ps$, the notches are expected at the frequency of $\Omega_1 = 5.85GHz$, $\Omega_2 = 11.8GHz$, and $\Omega_3 = 17.6GHz$, as shown in Fig. 4-16. The measurement results show the notch frequencies are very close to what we predicted.

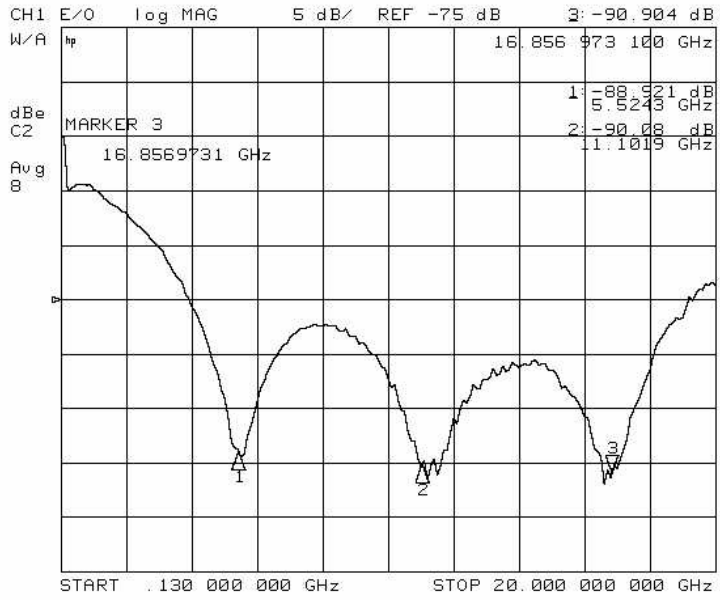

Fig. 4-15. 4-tap transversal filter frequency response by setting DGD1 at 89.6 ps delay and DGD2 45.2 ps.

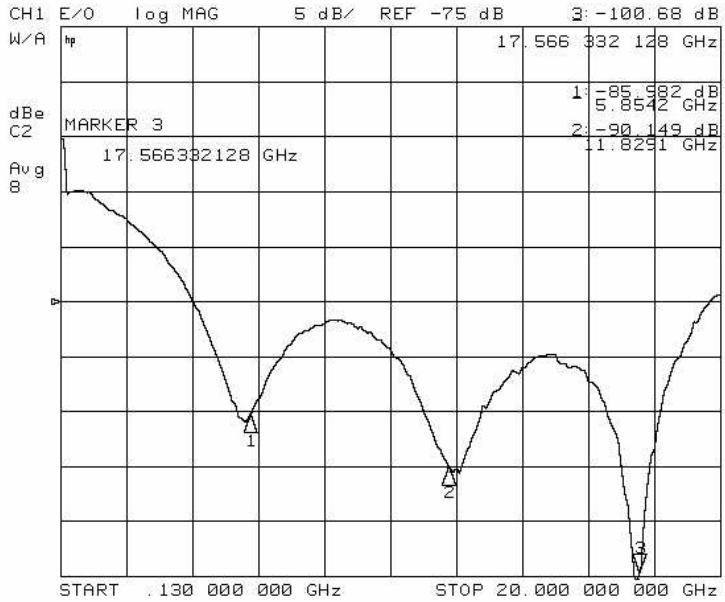

Fig. 4-16. 4-tap transversal filter frequency response by setting DGD1 at 85.4 ps delay and DGD2 42.3 ps.

However, we have to mention that this measurement is not so stable for two reasons. One is that we did not use any polarization-maintaining fiber to link two DGD units. The other is the remaining coherent noise of optical carriers since our laser source has very narrow linewidth (~5 MHz), i.e., very long coherent length in time domain. Although the orthogonal polarization between the adjacent taps helps compress the coherent noise, it can not thoroughly get rid of the coherent noise between the taps with same polarization direction.

4.5 Summary

In this chapter, the DGD unit is used to construct a digitally tunable incoherent optical RF notch filter which can achieve 60 dB out-of-band rejection level. The thermal stability is discussed. The bandpass filter based on double DGD link has been measured.

Reference

[1] Kalman Wilner, and Anthony P. Van Den Heuvel, "Fiber-Optic Delay Lines for Microwave Signal Processing", Proc. IEEE, Vol. 64, No. 5, pp 805-807, May 1976.

[2] K. Jackson, S. Newton, B. Moslehi, M. Tur, C. Cutler, J. Goodman and H. J. Shaw, Optical fiber delay-line signal processing, IEEE Trans. Microwave Theory Tech, Vol. 33, pp. 193-204, 1985.

[3] M. Tur, J. W. Goodman, B. Moslehi, J. E. Bowers, and H. J. Shaw, "Fiber-optic signal processor with applications to matrix-vector multiplication and lattice filtering," Optic. Lett., Vol. 7, No. 9, pp.463-465, 1982.

[4] S. A. Newton, R. S. Howland, K. P. Jackson, and H. J. Shaw, "High-speed pulse train generation using single-mode fiber recirculating delay lines," Electron. Lett., Vol. 19, pp.756-758, 1983.

[5] B. Moslehi, J. Goodman, M. Tur and H. J. Shaw, "Fiber-optic lattice signal processing", Proc. IEEE, Vol. 72, pp. 909-930, 1984.

[6] J. Capmany, B. Ortega, D. Pastor, and S. Sales, "Discrete-time optical processing of microwave signals", J. Lightwave Technol., Vol. 23, No. 2, pp. 702-723, 2005.

[7] Vahldieck, R., "Design and development of High-Q Microwave filters-past, present and future", In Proceedings of Africon 99, pp1099-1104, 1999.

[8] J. Capmany, D. Pastor, B. Ortega, and S. Sale, "Optical Processing of Microwave Signals", 0-7803-6455-4/00/ IEEE, 2000, pp241-4.

[9] David B. Hunter and Rober A. Minasian, "Photonic signal processing of microwave signals using an active-fiber Bragg-grating-pair structure", IEEE Trans. Microwave Theory Tech., Vol 45, pp1463-1466, Aug., 1997.

[10] Ningsi You and Robert A. Minasian, "A Novel high-Q optical microwave processor using hybrid delay-line filters", IEEE Trans. On Microwave theory and Tech., Vol. 47, No.7, July 1999.

[11] N. You and R. A. Minasian, "High-Q optical microwave filter", Electron. Lett. Vol. 35, No. 24, pp2125, Nov. 1999.

[12] Robert A. Minasian, Kamal E. Alameh, and Erwin H. W. Chan, "Photonics-based interference mitigation filters", IEEE Trans. Microwave Theory and Tech., Vol. 49, No.10, pp1894, Oct. 2001.

[13] D. Hunter and R. Minasian, “Reflectively tapped fiber optic transversal filter using in-fiber Bragg gratings”, Electron. Lett., Vol. 31, pp. 1010-1012, 1995.

[14] Jose Capmany, Daniel Pastor, and Beatriz Ortega, “New and flexible fiber-optic delay-line filters using chirped Bragg gratings and Laser arrays”, IEEE Trans. On Microwave theory and tech., vol. 47, No. 7, pp1321, July 1999.

[15] Ningsi You and Robert A. Minasian, “Synthesis of WDM grating-based optical microwave filter with arbitrary impulse response”, MWP’99 Digest, pp 223-6, 1999.

[16] D. B. Hunter, R. Minasian and P. A. Krug, “Tunable optical transversal filter based on chirped gratings”, Electron. Lett., Vol. 31, No. 25, pp 2205, 1995.

[17] W. Zhang and J. A. R. Williams, “Fibre optic bandpass transversal filter employing fibre grating arrays”, Electron. Lett., Vol. 35, No.12, pp1010, Jun.1999.

[18] Daniel Pastor, Jose Capmany, Beatriz Ortega, “Broad-band tunable microwave transversal notch filter based on tunable uniform fiber Bragg gratings as slicing filters”, IEEE Photon. Technol. Lett., Vol.13, No. 7, pp726, Jul. 2001.

[19] W. Zhang, J. A. R. Williams, L. A. Everall and I. Bennion, “Fibre optic radio frequency notch filter with linear and continuous tuning by using a chirped fibre grating”, Electron. Lett., Vol. 34, No. 18, pp1770, Sept. 1998.

[20] D. Hunter and R. Minasian, “Microwave optical filters using in-fiber Bragg grating arrays”, IEEE Microwave Guided Wave Lett., Vol. 6, pp 103-105, Feb. 1996.

[21] D. Norton, S. Johns, C. Keefer, and R. Soref, “Tunable microwave filtering using high dispersion fiber time delays”, IEEE Photon. Technol. Lett., vol. 6, pp. 831-832, July, 1994.

[22] A. P. Foord, P. Davis and A. Greenhalgh, “Synthesis of microwave and millimeter wave filters using optical spectrum slicing”, Electron. Lett., pp. 390-391, 1996.

[23] J. Capmany, D. Pastor and B. Ortega, “Fibre optic microwave and millimetre-wave filter with high density sampling and very high sidelobe suppression usingsubnanometre optical spectrum slicing”, Electron. Lett. Vol.35, No. 6, pp 494, Mar. 1999.

[24] Michael Y. Frankel and Ronald D. Esman, “Fiber-Optic tunable microwave transversal filter”, IEEE Photon. Technol. Lett., Vol. 7, No. 2, pp191-3, 1995.

[25] Daniel Pastor, Beatriz Ortega, Jose Capmany, Salvador Sales, Alfonso Martinez, Pascual Munoz, "Flexible and tunable microwave filters based on arrayed waveguide gratings", in Proc. IEEE Int. Topical Meeting on Microwave Photon., 2002, pp. 189-192, 2002.

[26] F. Coppinger, S. Yegnanarayanan, P. D. Trinh, B. Jalali, and I. L. Newberg, "Nonrecursive tunable photonic filter using wavelength-selective true time delay", IEEE Photon. Technol. Lett.., Vol. 8, pp1214-1216, Sept. 1996.

[27] W. Zhang, J. A. R. Williams, and I. Bennion, "Optical fibre delay line filter free of limitation imposed by optical coherence", Electron. Letts., Vol. 35, No. 24, pp2133, 1999.

[28] W. Zhang, J. A. R. Williams, and I. Bennion, "Polarization synthesized optical transversal filter employing high birefringence fiber gratings", IEEE Photonics Technology letters, Vol. 13, No.5, pp523, May 2001.

[29] Yicheng Lai, W. Zhang, and J. A. R. Williams, "A novel all-fiber bipolar transversal filter with complementary outputs", in Proc. IEEE Int. Topical Meeting on Microwave Photon.,(MWP'02), pp173, 2002.

[30] B. Moslehi and J. Goodman, "Novel amplified fiber optic recirculating delay line processor", J. Lightwave Technology, Vol. 10, pp. 1142-1147, Aug. 1992.

Chapter 5. Summary and Future Work

5.1 Summary of Dissertation

This dissertation contributes to the optical RF signal processing technique through the invention of a novel tunable lithium niobate loop (LN-loop) resonator for the coherent signal processing and by introducing a novel optical RF notch filter using the differential group delay (DGD) module for the incoherent signal processing.

Tunability is a very important property for the optical loop resonator as it compensates fabrication error and fine-tune the optical or RF response function. The resonators based on the silica waveguide or polymer waveguide generally only can be tuned by thermo-optic method which is slow and with low accuracy. Ti diffused lithium niobate waveguide is a very good candidate to construct an electrically tunable loop or disk resonator due to its advantages of low loss, large electro-optic effect, and mature fabrication technique. However, the bending loss caused by the weakly guided waveguide limits the waveguide from a sharp bending and makes it hard to form a circular loop. To overcome this difficulty, we adopt a pair of Y-junction reflectors to help guiding the light in one direction and squeeze the loop to two slightly curved lines very close to each other, so that the bending loss is negligible and wafer size needed is very compact.

The important design issues about the Ti diffused lithium niobate waveguide, the coupling section, the Y-junction reflector, and the tuning electrodes have been discussed in detail in Chapter 2.

The FIMMWave simulation to the Ti diffused waveguide of our demo device shows that the TM mode is more strongly guided than the TE mode because the maximum refractive index change for the extraordinary index n_e is about two times larger than the ordinary index n_o. In order to utilize the large electro-optic coefficient r_{33}, we design the demo device working for the TM mode.

The simulated power coupling ratio of TM mode varies from 93.5% to 52% when the coupling gap distance changes from 4 μm to 6 μm. The simulation fits the measured results very well for the demo device with the gap of 4 μm. For the larger gap of 6 μm, the measured power coupling ratio is 80%. The discrepancy may be caused by the SiO_2 layer on the surface and the gold electrode on the bus waveguide for the real device but lack in the simulation structure.

For the Y-reflector, the most important issue is to reduce its insertion loss. The testing devices built in Sumitomo company are estimated with 3.5 dB insertion loss when the Y-reflector is measured as a stand-alone component. However, this value is very possibly overestimated. FIMMWave simulation shows the low loss around 1.0 dB per Y-reflector is possible for 1.55 μm wavelength range. The simulation also predicts that the insertion loss of the Y-reflector is not sensitive to the wavelength changing from 1.52 to 1.57 μm.

The design of the CPW waveguide on the lithium niobate substrate is simulated with Ansoft HFSS. It is interesting to see that the rule of thumb—the characteristic impedance of CPW depends only to geometric ratio parameter k—still holds for the anisotropic crystal substrate. This simplifies the effort to design tapered feeder with characteristic impedance of 50 Ω. The pattern of electrode applied to the testing sample is slightly offset from the intent optimal design. But we manage to use it to demonstrate the high speed tunability. The comparison of the simulated and experimental S_{11} data shows the two data sets fit with each other for frequency below 7 GHz. While for frequency 7-10 GHz, the measured S_{11} roll off faster than the simulation results.

With the designed loop structure, the normalized frequency tunability of 175 MHz/(V·cm) is expected for the overlap integral of 0.37. It is possible to obtain normalized frequency tunability of 260 MHz/(V·cm) if the overlap integral can be optimized to 0.55.

The measurements to the first (1G) and second generation (2G) testing devices are discussed in chapter 3. For 1G device without tuning electrodes, the optical transmission curves fit very well with the all-pass filter model. The fitting result shows the power coupling ratio is about 92.5% and the loop roundtrip loss is about 3.5 dB for the device with coupling gap of 4.2 μm. The rejection level is about 5 dB. For 2G device, the DC tunability is measured of 500 MHz with applying 15 V to the phase tuning electrode, which has successfully demonstrated the normalized frequency tunability of 175 MHz/(V·cm). Similar result can be obtained by applying 30 V to the

coupling tuning electrode. By enlarging the coupling gap, the power coupling ratio reduces to 80% for 2G device and the rejection level is improved to 12 dB. The roundtrip loss is about -4 dB. The high speed tunability has been indirectly demonstrated by modulating the 2G device with high frequency RF signal. 3 dB link gain bandwidth of 5 GHz has been found. -42 dB normalized link gain, assuming the detector has responsivity of 1 A/W, is obtained. A serial 1xN optical power splitter is also theoretically discussed in chapter 3 as an interesting extension of the Y-reflector technique.

In chapter 4, an optical RF notch filter scheme is proposed and demonstrated with a 6-bit differential group delay (DGD) module. A 60 dB rejection level is achieved. The filter is controlled and digitally tuned with computer controlling. The bandpass filter based on two DGD modules also has been briefly discussed and experimentally demonstrated.

5.2 Future Works

Although we have experimentally demonstrated the tunable LN-loop, much works still need to do in the future to improve its performance.

For the coupling section, we would like to do further investigation to the power coupling ratio, to see how to reduce it to 56%, which matches to the roundtrip loss and consequently improve the rejection level.

For the Y-junction, further reducing the insertion loss is still possible by trying different geometric structures. The metal mirror limits the layout of the Y-reflector so that it ends at the facet. If we can use Bragg grating inside the waveguide to replace

the metal mirror, it will increase the flexibility to integrate the loop with other optical waveguide structure.

For the electrode, more efficient pattern is desired. The overlap integral can be optimized by fine-tune the hot electrode structure. Also we can consider special design of the electrode such as a resonant electrode or traveling wave electrode, to enhance the tuning efficiency or enlarge the bandwidth.

The device we proposed in the dissertation is just a building block. More complicated structure such as multiple-loop resonator can be built in similar fashion, to obtain more functions for the optical RF signal processing. The application in high speed modulator or switch is also interesting for future investigation.

Nonlinear optics may be another interesting application for the loop resonator as lithium niobate is a nonlinear optical crystal and the resonant cavity can support long interference time.